

1 Trace element composition of igneous and hydrothermal magnetite from  
2 porphyry deposits: Relationship to deposit subtypes and magmatic  
3 affinity

4 Xiao-Wen Huang,<sup>1,2,3,†</sup> Anne-Aurélie Sappin,<sup>2,3,4</sup> Émilie Boutroy,<sup>2,5</sup> Georges  
5 Beaudoin,<sup>2,3</sup> Sheida Makvandi<sup>2,3</sup>

7 <sup>1</sup>State Key Laboratory of Ore Deposit Geochemistry, Institute of Geochemistry,  
8 Chinese Academy of Sciences, Guiyang 550081, China

9 <sup>2</sup>Département de géologie et de génie géologique, Université Laval, Québec, QC G1V  
10 0A6, Canada

11 <sup>3</sup>Research Center on the Geology and Engineering of Mineral Resources (E4m),  
12 Université Laval, Québec, QC G1V 0A6, Canada

13 <sup>4</sup>Geological Survey of Canada, Natural Resources Canada, 490 rue de la Couronne,  
14 Québec, QC G1K9A9, Canada

15 <sup>5</sup>Agnico Eagle Mines Limited, 1655 3e Av, Val d'Or, QC J9P 1W1, Canada

18 <sup>†</sup>Corresponding author: e-mail, [huangxiaowen2008@live.cn](mailto:huangxiaowen2008@live.cn)

## Abstract

Trace element compositions of igneous and hydrothermal magnetite from nineteen well-studied porphyry Cu ± Au ± Mo, Mo, and W-Mo deposits, combined with partial least squares-discriminant analysis (PLS-DA), were used to investigate the factors controlling magnetite chemistry during igneous and hydrothermal processes, as divided by magmatic affinity and porphyry deposit subtypes. Igneous magnetite can be discriminated by relatively high P, Ti, V, Mn, Zr, Nb, Hf, and Ta contents but low Mg, Si, Co, Ni, Ge, Sb, W, and Pb contents, in contrast to hydrothermal magnetite. Compositional differences between igneous and hydrothermal magnetite are mainly controlled by the temperature, oxygen fugacity, co-crystallized sulfides, and element solubility/mobility that significantly affect the partition coefficients between magnetite and melt/fluids. Binary diagrams based on Ti, V, and Cr contents are not enough to discriminate igneous and hydrothermal magnetite in porphyry deposits.

Relatively high Si and Al contents discriminate porphyry W-Mo hydrothermal magnetite, probably reflecting the control by high Si, highly differentiated, granitic intrusions for this deposit type. Relatively high Mg, Mn, Zr, Nb, Sn, and Hf, but low Ti and V contents, discriminate porphyry Au-Cu hydrothermal magnetite, most likely resulting from a combination of mafic to intermediate intrusion composition, high chlorine in fluids, relatively high oxygen fugacity, and low temperature conditions. Igneous or hydrothermal magnetite from Cu-Mo, Cu-Au, and Cu-Mo-Au deposits cannot be discriminated from each other probably due to similar intermediate to felsic intrusion composition, melt/fluid composition, and conditions such as temperature

1 45 and oxygen fugacity for the formation of these deposits.

2  
3 46 The magmatic affinity of porphyritic intrusions exerts some control on the chemical  
4  
5  
6 47 composition of igneous and hydrothermal magnetite in porphyry system. Igneous and  
7  
8  
9 48 hydrothermal magnetite related to alkaline magma is relatively rich in Mg, Mn, Co,  
10  
11  
12 49 Mo, Sn, and high field strength elements (HFSE), perhaps due to high concentrations  
13  
14  
15 50 of chlorine and fluorine in magma and exsolved fluids, whereas those related to  
16  
17  
18 51 calc-alkaline magma are relatively rich in Ca but depleted in HFSE, consistent with  
19  
20  
21 52 the high Ca but low HFSE magma composition. Igneous and hydrothermal magnetite  
22  
23  
24 53 related to high-K calc-alkaline magma is relatively rich in Al, Ti, Sc, and Ta, due to a  
25  
26  
27 54 higher temperature of formation or enrichment of these elements in melt/fluids.

28  
29 55 PLS-DA on hydrothermal magnetite compositions from worldwide porphyry Cu,  
30  
31 56 iron oxide-copper-gold (IOCG), Kiruna-type iron oxide-apatite (IOA), and skarn  
32  
33  
34 57 deposits identify important discriminant elements for these deposit types. Magnetite  
35  
36  
37 58 from porphyry Cu deposits is characterized by relatively high Ti, V, Zn, and Al  
38  
39  
40 59 contents, whereas that from IOCG deposits can be discriminated from other types of  
41  
42  
43 60 magnetite by its relatively high V, Ni, Ti, and Al contents. IOA magnetite is  
44  
45  
46 61 discriminated by higher V, Ti, and Mg but lower Al contents, whereas skarn magnetite  
47  
48  
49 62 can be separated from magnetite from other deposit types by higher Mn, Mg, Ca, and  
50  
51  
52 63 Zn contents. Decreased Ti and V contents in hydrothermal magnetite from porphyry  
53  
54  
55 64 Cu and IOA, to IOCG, and to skarn deposits may be related to decreasing temperature  
56  
57  
58 65 and increasing oxygen fugacity. The relative depletion of Al in IOA magnetite is due  
59  
60  
61 66 to its low magnetite-silicate melt partition coefficient, immobility of Al in fluids, and

1 67 earlier, higher-temperature magmatic or magmatic-hydrothermal formation of IOA  
2  
3 68 deposits. The relative enrichment of Ni in IOCG magnetite reflects more mafic  
4  
5  
6 69 magmatic composition and less competition with sulfide, whereas elevated Mn, Mg,  
7  
8  
9 70 Ca, and Zn in skarn magnetite results from enrichment of these elements in fluids via  
10  
11  
12 71 more intensive fluid-carbonate rock interaction.

13  
14 72 **Keywords:** Trace elements, magnetite, porphyry, deposit subtypes, magmatic affinity,  
15  
16  
17 73 discrimination diagrams  
18  
19  
20  
21  
22  
23  
24  
25  
26  
27  
28  
29  
30  
31  
32  
33  
34  
35  
36  
37  
38  
39  
40  
41  
42  
43  
44  
45  
46  
47  
48  
49  
50  
51  
52  
53  
54  
55  
56  
57  
58  
59  
60  
61  
62  
63  
64  
65

## Introduction

Magnetite is a widespread accessory mineral in various types of rocks and mineral deposits. Hydrothermal magnetite occurs in porphyry Cu ± Au ± Mo deposits as disseminated grains, massive aggregates, veins, intergrowths and replacements of other minerals such as hematite (Nadoll et al., 2014, 2015; Canil et al., 2016). The amount of magnetite associated with mineralization in typical porphyry deposits can locally exceed 10% by volume (Sillitoe, 1997; Sinclair, 2007). In shallow porphyry systems, Fe<sup>2+</sup>-chloride complexes can react with H<sub>2</sub>O or aqueous SO<sub>2</sub> to precipitate magnetite, during which oxidized S species in fluids exsolved from magma are reduced, leading to sulfide mineralization (Simon et al., 2004; Sun et al., 2004). Hydrothermal magnetite is commonly crystallized with chalcopyrite, bornite, and chalcocite in porphyry systems at high temperature and *f*O<sub>2</sub>, and low *f*S<sub>2</sub> (Beane, 1981). In addition to hydrothermal magnetite, igneous magnetite is also common in the host or country rocks of porphyry deposits (Ishihara, 1977; Nadoll et al., 2015; Pisiak et al., 2017).

Chemical composition of igneous and hydrothermal magnetite, in combination with petrographic description and statistical analysis, can be used to discriminate magnetite from various geological environments (Carew, 2004; Singoyi et al., 2006; Rusk et al., 2009; Dupuis and Beaudoin, 2011; Dare et al., 2012, 2014; Boutroy et al., 2014; Nadoll et al., 2012, 2014; Huang et al., 2013, 2014, 2015a, b, 2016, 2018b) and can be employed to fingerprint different types of ore deposits (Dupuis and Beaudoin, 2011; Boutroy et al., 2014; Makvandi et al., 2016a, b, 2017; Pisiak et al., 2017; Huang et al.,

1 96 2018a). A number of in situ iron oxide trace element studies of porphyry deposits  
2  
3  
4 97 (Dupuis and Beaudoin, 2011; Mountjoy, 2011; Nadoll et al., 2014, 2015; Canil et al.,  
5  
6 98 2016; Pisiak et al., 2017) discussed the factors controlling compositional variations in  
7  
8  
9 99 iron oxides and the formation of mineralization. For example, Canil et al. (2016) used  
10  
11  
12 100 Principal Component Analysis (PCA) of hydrothermal magnetite from porphyry Cu ±  
13  
14 101 Au ± Mo and skarn deposits to identify positive correlations of Al, Ti, and V related to  
15  
16  
17 102 temperature, and negative correlations of Sn and Mo, with Mn and Co, governed by  
18  
19  
20 103 fluid chemistry. Dupuis and Beaudoin (2011) proposed the Ca+Al+Mn vs. Ti+V and  
21  
22  
23 104 Ni/(Cr+Mn) vs. Ti+V diagrams to discriminate iron oxide-copper-gold (IOCG),  
24  
25  
26 105 Kiruna-type iron oxide-apatite (IOA), banded iron formation, porphyry Cu, skarn,  
27  
28 106 Fe-Ti-V, Ni-Cu-PGE, and volcanogenic massive sulfide (VMS) deposits. These  
29  
30  
31 107 discrimination diagrams are useful in identifying the iron oxides with unknown origin.  
32  
33  
34 108 However, individual analyses of samples from a specific deposit type (e.g., porphyry  
35  
36  
37 109 Cu, skarn, IOA) can show a large compositional variability. Nadoll et al. (2014, 2015)  
38  
39  
40 110 investigated the trace element composition of magnetite from porphyry Cu and skarn  
41  
42  
43 111 deposits from the southwestern USA, and argued that the boundary in the Al+Mn vs.  
44  
45  
46 112 Ti+V diagram to separate these two deposit types is transitional. Pisiak et al. (2017)  
47  
48  
49 113 calculated discriminant functions using Linear Discriminant Analysis (LDA) of trace  
50  
51  
52 114 element data of barren igneous, ore-related igneous, and porphyry hydrothermal  
53  
54  
55 115 magnetite, and applied the results to exploration for porphyry deposits near the Mount  
56  
57  
58 116 Polley Cu-Au deposit (Canada). Their study demonstrated that LDA models for  
59  
60  
61 117 magnetite composition are effective tools in exploration for buried porphyry systems  
62  
63  
64  
65

1 118 (Pisiak et al., 2017).

2  
3 119 Porphyry deposits can be classified into subtypes according to their metal  
4  
5  
6 120 endowment such as porphyry Cu, Cu-Mo, Cu-Au, Cu-Mo-Au, Au, Mo, W-Mo, Sn,  
7  
8  
9 121 Sn-Ag, and Ag deposits (Kirkham and Sinclair, 1995; Singer, 1995; Cooke et al., 2005;  
10  
11 122 Sinclair, 2007; Sillitoe, 2010). Different types of porphyry deposits reflect various  
13  
14 123 magma and fluid compositions and physical conditions such as temperature, pressure,  
15  
16  
17 124 and oxygen fugacity. For example, high-sulfidation Au-rich deposits commonly occur  
18  
19  
20 125 at shallower level above porphyry Cu system (Sillitoe, 2010). The composition of host  
21  
22 126 rocks may strongly influence the size, grade, and type of mineralization generated in  
23  
24  
25 127 porphyry Cu systems (Sillitoe, 2010). The porphyritic intrusions in porphyry Cu  
26  
27  
28 128 deposits are exclusively I-type, magnetite-series (Ishihara, 1981), and typically  
29  
30  
31 129 metaluminous and medium K calc-alkaline, but may also fall into the high-K  
32  
33  
34 130 calc-alkaline (shoshonitic) or alkaline fields (Seedorf, 2005). There is an affinity  
35  
36  
37 131 between high-K calc-alkaline rocks and gold-rich porphyry systems (Müller and  
38  
39 132 Groves, 1993; Sillitoe, 1997; Sillitoe, 2000). Felsic intrusive rocks genetically related  
40  
41  
42 133 to porphyry W deposits are commonly characterized by F-rich fluorite and/or topaz  
43  
44  
45 134 (Sinclair, 1995). However, the relationship between the chemical composition of  
46  
47  
48 135 igneous and hydrothermal magnetite with the porphyry deposit subtypes and the  
49  
50  
51 136 magmatic affinity of the porphyritic intrusions remains poorly studied.

52  
53 137 In this study, we investigate the chemical composition of igneous and hydrothermal  
54  
55  
56 138 magnetite from a wide range of porphyry deposit subtypes (Table 1). These deposits  
57  
58  
59 139 formed in a range of geological environments, with different ages and country rock

1 140 types, and are related to porphyry intrusions with various compositions and magmatic  
2  
3 141 affinities (Table 1). Trace element compositions of magnetite were determined using  
4  
5  
6 142 electron probe microanalyzer (EPMA) and laser ablation-inductively coupled  
7  
8  
9 143 plasma-mass spectrometry (LA-ICP-MS). The geochemical data were investigated by  
10  
11 144 PLS-DA to identify factors controlling the formation of igneous and hydrothermal  
12  
13 145 magnetite in porphyry systems and to establish the link of igneous and hydrothermal  
14  
15 146 magnetite chemistry with porphyry deposit subtypes and the magmatic affinity of  
16  
17 147 porphyry intrusions. The trace element composition of hydrothermal magnetite from  
18  
19  
20 148 porphyry Cu deposits is also compared with that of IOCG, IOA, and skarn magnetite  
21  
22  
23 149 to identify possible relationship between them and to provide a better understanding  
24  
25  
26 150 of trace element fingerprints in magnetite from porphyry deposits.  
27  
28  
29  
30

## 31 32 33 34 152 **Sampling and Analytical Methods**

### 35 36 153 *Sampling*

37  
38  
39 154 Seventy-nine samples representing different types of host rocks, veins, and  
40  
41  
42 155 hydrothermal alteration were collected from porphyry Cu ± Au ± Mo (17), porphyry  
43  
44 156 Mo (1), and porphyry W-Mo (1) deposits (Table 1). These deposits are distributed in  
45  
46  
47 157 western and eastern North America, western South America, Eastern Europe, Central  
48  
49  
50 158 Asia, and the southwestern Pacific regions (Table 1). According to the main metals,  
51  
52 159 these deposits can be divided into porphyry Au-Cu, Cu-Au, Cu-Mo, Cu-Mo-Au, Mo,  
53  
54 160 and W-Mo deposits of Late Ordovician to Miocene age (Table 1). They are mainly  
55  
56  
57  
58 161 hosted by intrusions, dikes, and stocks of intermediate to felsic composition, e.g.,  
59  
60  
61  
62  
63  
64  
65



1 162 diorite, monzonite, monzodiorite, syenite, granite, and granodiorite. Some deposits  
2  
3 163 are also hosted by subvolcanic porphyries such as andesite to rhyolite, trachyandesite,  
4  
5  
6 164 trachyte, and alkaline basalt (Table 1). The porphyry intrusions were emplaced into a  
7  
8  
9 165 range of country rocks, including andesitic to basaltic volcanic rocks, volcanoclastic  
10  
11  
12 166 rocks, clastic sedimentary rocks, carbonate rocks, granite to diorite, schist, and gneiss  
13  
14  
15 167 (Table 1). The volcanic and intrusive rocks have alkaline, calc-alkaline, and high-K  
16  
17  
18 168 calc-alkaline affinities (Table 1). A total of 630 magnetite grains from the 79 samples  
19  
20  
21 169 were analyzed by EPMA and 68 magnetite grains from 19 samples were analyzed by  
22  
23  
24 170 LA-ICP-MS (Table 2). The EPMA dataset includes 242 analyses from Dupuis and  
25  
26  
27 171 Beaudoin (2011) (Table 2).

28 172

### 30 173 *Petrography*

32  
33  
34 174 Optical petrography was used to characterize the mineral assemblage, magnetite  
35  
36  
37 175 texture, and to assist in discrimination of hydrothermal from igneous magnetite.  
38  
39  
40 176 Magnetite textures were examined using a JEOL JSM-840A scanning electron  
41  
42  
43 177 microscope at Université Laval (Québec, Canada) under backscattered and secondary  
44  
45  
46 178 electron modes. Semi-quantitative energy dispersive X-ray spectrometry (EDS) was  
47  
48  
49 179 used to identify exsolution products, mineral inclusions, and associated minerals.  
50  
51  
52 180 Operating conditions used an accelerating voltage of 15 kV and a beam current of 60  
53  
54  
55 181  $\mu\text{A}$  at a working distance of 20 mm.

56 182

### 58 183 *EPMA analyses*

1 184 Magnetite was analyzed at Université Laval using a CAMECA SX-100 EPMA,  
2  
3 185 equipped with five wavelength-dispersive spectrometers, using a 10- $\mu$ m diameter  
4  
5 186 beam with a voltage of 15 kV and a current of 100 nA. Analytical conditions are same  
6  
7 187 to those described by Boutroy et al. (2014). Analyzed crystals are LIF for V and Cr,  
8  
9 188 LLIF for Zn, Cu, Ni, and Mn, LPET for K, Sn, Ca, and Ti, and TAP for Al, Si, and Mg.  
10  
11 189  $K\alpha$  signal was acquired for all elements. Calibration was achieved using a range of  
12  
13 190 natural and synthetic standards, comprising simple oxides (GEO Standard Block of P  
14  
15 191 and H Developments) and natural minerals (Mineral Standard Mount MINM 25–53,  
16  
17 192 Astimex Scientific) (Jurek and Hulínský, 1980). The background was measured for  
18  
19 193 15-20 s and the concentration was counted over the peak for 20 to 40 s depending on  
20  
21 194 the element. The average detection limits are 17 ppm for K, 23 ppm for Ca, 29 ppm  
22  
23 195 for Sn, 34 ppm for Cr, 67 ppm for Ni, 83 ppm for Mg, 93 ppm for Cu, 105 ppm for  
24  
25 196 Mn, 110 ppm for V, 149 ppm for Zn, 151 ppm for Si, 154 ppm for Ti, and 301 ppm  
26  
27 197 for Al.  
28  
29  
30  
31  
32  
33  
34  
35  
36  
37  
38  
39  
40  
41

#### 42 199 *LA-ICP-MS analyses*

43  
44 200 Magnetite was analyzed using a RESolution M-50 193 nm Excimer Laser Ablation  
45  
46 201 system coupled with an Agilent 7700x ICP-MS at Université du Québec à Chicoutimi  
47  
48 202 (UQAC), using a beam size of 25 to 80  $\mu$ m with a speed stage of 3 to 15  $\mu$ m/s and a  
49  
50 203 laser frequency of 10 Hz and a power of 5 mJ per pulse. Lines were ablated across the  
51  
52 204 width of a magnetite grain for a period ranging from 20 to 60 seconds depending on  
53  
54 205 the grain size, after monitoring a gas blank for 20–30 seconds. LA-ICP-MS was used  
55  
56  
57  
58  
59  
60  
61  
62  
63  
64  
65

1 206 to analyze  $^{24}\text{Mg}$ ,  $^{27}\text{Al}$ ,  $^{45}\text{Sc}$ ,  $^{47}\text{Ti}$ ,  $^{51}\text{V}$ ,  $^{52}\text{Cr}$ ,  $^{55}\text{Mn}$ ,  $^{60}\text{Ni}$ ,  $^{66}\text{Zn}$ ,  $^{75}\text{As}$ ,  $^{59}\text{Co}$ ,  $^{69}\text{Ga}$ ,  $^{74}\text{Ge}$ ,  
2  
3 207  $^{89}\text{Y}$ ,  $^{90}\text{Zr}$ ,  $^{95}\text{Mo}$ ,  $^{101}\text{Ru}$ ,  $^{105}\text{Pd}$ ,  $^{111}\text{Cd}$ ,  $^{118}\text{Sn}$ ,  $^{121}\text{Sb}$ ,  $^{93}\text{Nb}$ ,  $^{107}\text{Ag}$ ,  $^{115}\text{In}$ ,  $^{178}\text{Hf}$ ,  $^{181}\text{Ta}$ ,  $^{182}\text{W}$ ,  
4  
5  
6 208  $^{187}\text{Re}$ ,  $^{193}\text{Ir}$ ,  $^{195}\text{Pt}$ ,  $^{197}\text{Au}$ ,  $^{208}\text{Pb}$  and  $^{209}\text{Bi}$  isotopes in magnetite. Sulfur, Si, Ca and Cu  
7  
8  
9 209 were monitored to detect mineral inclusions. Multiple isotopes of Zr ( $^{90,92}\text{Zr}$ ) and Ga  
10  
11 210 ( $^{69,71}\text{Ga}$ ) were measured to resolve the isobaric interferences. Analytical conditions  
12  
13  
14 211 are same to those described by Boutroy et al. (2014). A single Fe-rich reference  
15  
16  
17 212 material, GSE-1G, containing all the required elements, was used for calibration  
18  
19  
20 213 (Savard et al., 2012). To monitor the quality of the analyses, reference materials  
21  
22  
23 214 GSD-1G and BC28 (natural magmatic magnetite) were analyzed for each run. Data  
24  
25  
26 215 reduction was carried out using the software Iolite. Iron was used as the internal  
27  
28  
29 216 standard to compute concentration assuming stoichiometric magnetite (Dare et al.,  
30  
31 217 2012).

## 218 219 **Statistical Methods**

### 220 *Estimation of average composition*

221 Electron microprobe and LA-ICP-MS datasets are typically censored because they  
222 contain non-detect data that are below the minimum detection limits (Helsel, 2005).

223 The average composition of iron oxides was estimated using the nonparametric  
224 Kaplan-Meier (K-M) method (NADA package in R; Lee and Helsel, 2007).

### 225 226 *Data preprocessing and partial least squares-discriminant analysis*

227 Censored compositional data were imputed using the k-nearest neighbors function

1 228 with the Aitchison distance (robCompositions package in R; Hron et al., 2010;  
2  
3 229 Makvandi et al., 2016b). Geochemical data, summed to 100%, can lead to spurious  
4  
5  
6 230 correlations (Aitchison, 1986; Whitten, 1995). This is referred as the ‘closure  
7  
8  
9 231 problem’, inherent to all compositional datasets (Aitchison, 1986). In this study, data  
10  
11  
12 232 were transformed using centered-log ratio (clr) that is suitable for multivariate  
13  
14  
15 233 statistical techniques such as PLS-DA (Aitchison, 1986; Egozcue et al., 2003;  
16  
17 234 Makvandi et al., 2016b).

20 235 Multivariate statistical analysis of EPMA and LA-ICP-MS data was performed in  
21  
22  
23 236 order to 1) recognize factors responsible for compositional variations of magnetite, 2)  
24  
25 237 identify the relationship between igneous and hydrothermal magnetite, and 3) unravel  
26  
27  
28 238 the relationships between magnetite chemistry and deposit subtype, magmatic affinity,  
29  
30  
31 239 and host porphyry composition. The PLS-DA method has been described in Makvandi  
32  
33  
34 240 et al. (2016b) and Huang et al. (2018a). PLS-DA is a supervised classification  
35  
36  
37 241 technique using labeled data, which sharpens the separation between groups of  
38  
39  
40 242 observations by rotating principal components. This technique produces maximum  
41  
42  
43 243 separation among classes and identifies the variables responsible for the separation of  
44  
45  
46 244 different classes (De Iorio et al., 2008). In the PLS-DA method, a series of orthogonal  
47  
48  
49 245 components (latent variables) are extracted to relate the X ( $N \times K$ ) and Y ( $N \times M$ )  
50  
51  
52 246 matrices by maximizing the covariance between the two matrices using the following  
53  
54  
55 247 equations (Wold et al., 2001; Eriksson et al., 2013; Brereton and Lloyd, 2014):

56 248  $X = TP^T + E$  (1)

58 249  $Y = TQ^T + F$  (2)

1 250  $T = XW^*$  (3)

2  
3 251 where  $T$  ( $N \times r$ ) is the score matrix containing  $r$  orthogonal PLS components (scores).

4  
5  
6 252 The  $T$  matrix represents the common latent variable space of both  $X$  and  $Y$  matrices.

7  
8 253 For Eqs. (1)–(3),  $P$  ( $N \times r$ ) and  $Q$  ( $M \times r$ ) are the loadings matrices for  $X$  and  $Y$ ,

9  
10  
11 254 respectively. The weight matrix ( $W^*$ ) consists of the coefficients of the linear

12  
13  
14 255 combinations of the  $X$  variables that are the most predictive of  $Y$ .  $E$  and  $F$  are the

15  
16  
17 256 model residuals.

18  
19  
20 257 Loadings biplots ( $qw^*_1$ - $qw^*_2$ ), score scatter plots ( $t_1$ - $t_2$ ), score contribution plots,

21  
22 258 and variable importance on projection (VIP) plots were generated for different

23  
24  
25 259 datasets investigated by PLS-DA, following Makvandi et al. (2016b). Loadings

26  
27 260 biplots indicate the correlation among different variables (elements), and the

28  
29  
30 261 relationship between the variables and different sample classes (e.g., magnetite

31  
32  
33 262 types/deposit subtypes/magmatic affinity/porphyry composition). The loading values

34  
35  
36 263 show the impact of elements on the model, and the sign of the values indicates

37  
38  
39 264 positive or negative correlation between the elements. Elements that plot in the

40  
41  
42 265 vicinity of each other in PLS-DA loadings space show strong positive correlations,

43  
44  
45 266 and they are negatively correlated to those in the opposite quadrant. The correlation

46  
47  
48 267 among variables and sample classes controls the distribution of samples in the scores

49  
50  
51 268 scatter plots. Score contribution plots depict the compositional difference between the

52  
53  
54 269 mean composition of a cluster (sample group) and the mean composition of the whole

55  
56  
57 270 dataset. Given that data is mean-centered prior to PLS-DA, the origin of score scatter

58  
59  
60 271 plots represents the mean composition of whole dataset (Makvandi et al., 2016b). The

1 272 VIP plots are also used to indicate the impact of different variables on the sample  
2  
3 273 classification, where VIP values equal and/or larger than 1 are most important for  
4  
5  
6 274 classification (Eriksson et al., 2013).  
7  
8

9 275

## 10 11 276 **Petrography**

12  
13  
14 277 One important aspect of petrographic observations is to discriminate igneous  
15  
16  
17 278 magnetite from hydrothermal magnetite. McQueen and Cross (1998) illustrated that  
18  
19  
20 279 texture or crystal habit may reflect the origin of magnetite grains. Nadoll et al. (2015)  
21  
22  
23 280 suggested that magnetite of igneous and hydrothermal origin can be determined based  
24  
25  
26 281 on occurrence (vein vs. disseminated in host rock), crystal habit (euhedral vs.  
27  
28  
29 282 massive), associated minerals (mafic minerals vs. hydrothermal minerals), and the  
30  
31 283 occurrence and type of exsolution and mineral inclusions.  
32

33  
34 284

### 35 36 285 *Igneous magnetite in porphyry systems*

37  
38  
39 286 In the studied porphyry deposits, igneous magnetite is disseminated in barren to  
40  
41  
42 287 slightly mineralized, weakly altered, volcanic and intrusive host rocks, such as  
43  
44  
45 288 andesite (Fig. 1A), dacite (Fig. 1B), diorite and monzonite porphyries. Igneous  
46  
47  
48 289 magnetite is an accessory phase (<~10 modal%) associated with felsic and mafic  
49  
50  
51 290 magmatic minerals including plagioclase, K-feldspar, hornblende, and biotite (Figs.  
52  
53 291 1A-B). Igneous magnetite occurs as subhedral to anhedral grains (Figs. 1A-B) and  
54  
55  
56 292 rarely as bands in ilmenite grains in the Rosia Poeni porphyry Cu-Au deposit (Fig.  
57  
58  
59 293 1C). It commonly contains ilmenite and spinel exsolution lamellae (Fig. 1D). Titanite

1 294 may occur as inclusions in magnetite (Fig. 1E), or as replacement of ilmenite lamellae  
2  
3  
4 295 in magnetite (Fig. 1F). Locally, hematite partially replaced magnetite (martitization)  
5  
6 296 along spinel planes, rims, and fissures (Fig. 1D). In the Mount Milligan deposit,  
7  
8  
9 297 igneous magnetite is also replaced by chalcopyrite along fractures (Fig. 1F).

10  
11 298

### 12 13 14 299 *Hydrothermal magnetite in porphyry systems*

15  
16  
17 300 As mentioned by Nadoll et al. (2014), the term hydrothermal magnetite can be  
18  
19  
20 301 ambiguous especially when considering the complex geological and mineralogical  
21  
22  
23 302 relationships in magmatic-hydrothermal deposits. In a porphyry system, assigning a  
24  
25  
26 303 hydrothermal origin to magnetite can be complicated by multiple vein generations,  
27  
28  
29 304 overprints of multiple alteration stages, fluid/rock interaction, and secondary  
30  
31 305 weathering processes (Nadoll et al., 2014). For example, early magnetite veins can be  
32  
33  
34 306 crosscut by K-feldspar + quartz + magnetite + pyrite veins, and both veins can be cut  
35  
36  
37 307 by late quartz + sericite + pyrite ± magnetite veins (Einaudi, 1982; Titley, 1990;  
38  
39 308 Nadoll et al., 2014). Here, vein crosscutting relationship and magnetite generations  
40  
41  
42 309 are not emphasized because the compositional variations of hydrothermal magnetite  
43  
44  
45 310 are discussed at deposit or deposit type scale rather than at the vein scale. All  
46  
47  
48 311 generations of magnetite with possible hydrothermal origin are grouped together.  
49  
50  
51 312 Hydrothermal magnetite is abundant (~15-30 modal%) within weakly to strongly  
52  
53  
54 313 altered host rocks and within fissures, associated with sericite, chlorite, and epidote  
55  
56 314 (Fig. 2A). Anhedral to subhedral hydrothermal magnetite is disseminated in  
57  
58  
59 315 sericitized feldspath-rich rock and was crosscut by chlorite + magnetite + chalcopyrite

1 316 veins (Fig. 2A). In addition, hydrothermal magnetite mainly occurs within and along  
2  
3 317 quartz-dominated (Figs. 2B-C) and magnetite-dominated (Figs. 2D-F) veins. It forms  
4  
5 318 disseminated grains (Fig. 2B) or massive aggregates (Figs. 2C-D), and is locally  
6  
7  
8 319 surrounded by chalcopyrite (Fig. 2C) and pyrite (Fig. 2E). Hydrothermal magnetite is  
9  
10  
11 320 partially or totally martitized (Fig. 2F). In the Kharmagtai and Skouries deposits,  
12  
13  
14 321 replacement of magnetite by chalcopyrite is common (Figs. 2G-H).  
15  
16

17 322 Weak oscillatory zoning is locally found in hydrothermal magnetite using  
18  
19  
20 323 back-scattered electron (BSE) imaging. Zonation is characterized by light gray zones,  
21  
22  
23 324 which alternate with fine dark gray zones rich in small inclusions (<1  $\mu\text{m}$  to 10  $\mu\text{m}$ ,  
24  
25 325 Figs. 3A-E). Quartz is the main inclusion in magnetite. Some magnetite grains from  
26  
27  
28 326 the Mount Pleasant W-Mo deposit show dissolution-reprecipitation texture composed  
29  
30  
31 327 of Si-rich, dark gray and Si-poor, light gray domains (Fig. 3F). This texture in  
32  
33  
34 328 porphyry deposits is not as common as in IOCG, IOA, and skarn deposits (Hu et al.,  
35  
36 329 2015; Heidarian et al., 2016; Huang and Beaudoin, 2018; Huang et al., 2018b).  
37  
38  
39 330 Because of elemental heterogeneity in magnetite with oscillatory zoning and  
40  
41  
42 331 compositional modification during dissolution-reprecipitation processes (Hu et al.,  
43  
44  
45 332 2015; Huang et al., 2018b), magnetite grains with oscillatory zoning and  
46  
47  
48 333 dissolution-precipitation textures were not analyzed by EPMA and LA-ICP-MS.  
49

50 334

### 51 52 53 335 **Chemical Composition of Magnetite**

54  
55 336 Igneous and hydrothermal magnetite from the porphyry deposits contains variable  
56  
57  
58 337 trace element contents. Titanium, Si, Al, Mn, Cu, Mg, V, Zn, Ca, K, Cr, Sn, P, Ni, Pb,  
59  
60  
61  
62  
63  
64  
65



1 338 W, Zr, Co, and Ga (in decreasing order of maximum abundance) are in concentrations  
2  
3 339 higher than 100 ppm. Magnetite also contains low concentrations (<100 ppm) of Nb,  
4  
5  
6 340 As, Sc, Y, Mo, La, Bi, Sm, Sb, Hf, Ta, Ge, Yb, In, and Ag. Cadmium, platinum-group  
7  
8  
9 341 elements (Ir, Pt, and Os), and Au are typically below or close to the lower detection  
10  
11 342 limit of LA-ICP-MS. The full EPMA and LA-ICP-MS dataset for all magnetite grains  
12  
13 343 is given in online Appendix [Table A1](#). Elements such as Mg, Al, Ti, V, and Mn occur  
14  
15 344 in significant concentrations in magnetite and are often detectable by both EPMA and  
16  
17 345 LA-ICP-MS. Other elements such as K, Sn, Cu, Zn, Si, Ca, Cr, and Ni often have  
18  
19 346 lower concentration near or below detection for the EPMA. There is a good  
20  
21 347 correlation between EPMA and LA-ICP-MS analyses for elements V, Al, and Mn ( $R^2$   
22  
23 348 = 0.98, 0.83, 0.75; [Fig. A1](#) in online Appendix). However, significant differences are  
24  
25 349 observed between EPMA and LA-ICP-MS analyses for elements Ti, Mg, Cr, Ca, and  
26  
27 350 Si ( $R^2 = 0.36, 0.32, 0.28, 0.04, 0.006$ ; [Fig. A1](#)). Significant scatter observed for certain  
28  
29 351 elements may be due to the difference in beam size between the EPMA and  
30  
31 352 LA-ICP-MS. For example, extensive exsolution is observed in the igneous magnetite  
32  
33 353 grains ([Figs. 1D-F](#)). The smaller beam size of EPMA (10  $\mu\text{m}$ ) is less able to  
34  
35 354 homogenize entire bulk composition of magnetite with significant exsolution lamellae,  
36  
37 355 whereas the area rasterized by the larger laser spot size (80  $\mu\text{m}$ ) is more efficient for  
38  
39 356 homogenizing material during analysis (Dare et al., 2012). Therefore, this difference  
40  
41 357 in sampling would contribute significantly to differences in concentrations for any  
42  
43 358 element that is heterogeneously distributed in magnetite, such as Ti, which occurs as  
44  
45 359 ilmenite exsolution lamellae ([Figs. 1D-F](#)). The significant differences in Si, Ca, Mg,  
46  
47  
48  
49  
50  
51  
52  
53  
54  
55  
56  
57  
58  
59  
60  
61  
62  
63  
64  
65

1 360 and Cr concentrations between EPMA and LA-ICP-MS analyses may be due to  
2  
3 361 different detection limits of these elements for two different analytical techniques and  
4  
5  
6 362 unresolved mineral inclusions during LA-ICP-MS analyses. For example, the higher  
7  
8  
9 363 Si and Ca contents analyzed by LA-ICP-MS than by EPMA (Fig. A1) are partly due  
10  
11 364 to unavoidable mineral inclusions that occur in submicron or nanometer scale.

12  
13  
14 365

15  
16  
17 366 *Average trace element composition of magnetite*

18  
19  
20 367 The chemical composition of individual analyses and the average composition of each  
21  
22 368 sample, normalized to bulk continental crust (Rudnick and Gao, 2003), are shown in  
23  
24  
25 369 online Appendix Figs. A2-A5. EPMA data show that igneous and hydrothermal  
26  
27  
28 370 magnetite from the same deposit has similar normalized trace element patterns,  
29  
30  
31 371 respectively, and that normalized ratios of a specific element vary within one order of  
32  
33  
34 372 magnitude (Figs. A2-A4). Igneous and hydrothermal magnetite from the same deposit  
35  
36  
37 373 has different trace element patterns. For example, igneous magnetite (sample 3133)  
38  
39 374 from the Bajo de la Alumbrera Cu-Au deposit has higher Al, Mn, Mg, Ti, and Zn  
40  
41  
42 375 contents than hydrothermal magnetite (Fig. A2). Similarly, igneous magnetite (sample  
43  
44  
45 376 Spegar1) from the Reko Diq Cu-Au deposit and sample 10880-B from the Butte  
46  
47  
48 377 Cu-Mo deposit, have higher Al, Mn, Mg, and Ti contents than hydrothermal magnetite  
49  
50  
51 378 in the same deposit (Figs. A3-A4). However, some igneous magnetite grains (e.g.,  
52  
53 379 Loc18b in Reko Diq or Bur-98-5 and Bur-98-8 in Butte) also show similar trace  
54  
55  
56 380 element patterns to hydrothermal magnetite in the same deposit (Figs. A3-A4).  
57  
58  
59 381 LA-ICP-MS data show igneous magnetite from the same deposit have more variable

1 382 trace element compositions with normalized Zr, Ta, Nb, W, and Cu contents variation  
2  
3 383 exceeding one order of magnitude (Fig. A5). This is the same for hydrothermal  
4  
5  
6 384 magnetite (Fig. A5).

7  
8  
9 385 Figure 4 provides the average composition of individual deposits, normalized to  
10  
11 386 bulk continental crust (Rudnick and Gao, 2003). EPMA data show that most igneous  
12  
13 387 magnetite from different porphyry deposits has similar normalized trace element  
14  
15  
16  
17 388 patterns (Fig. 4A), with the exception of the Mount Milligan deposit, which has Mn  
18  
19 389 contents one order of magnitude lower than other samples. Hydrothermal magnetite  
20  
21  
22 390 from most porphyry deposits shows similar normalized EPMA trace element patterns  
23  
24  
25 391 (Fig. 4B). However, hydrothermal magnetite from the Mount Pleasant W-Mo deposit  
26  
27 392 has higher Si, Al, and Sn but lower Mg, Ti, and V contents than that from other  
28  
29  
30 393 deposits (Fig. 4B). LA-ICP-MS data show that igneous magnetite from the Bajo de la  
31  
32  
33 394 Alumbraera and Butte deposits has slightly different trace element patterns with  
34  
35  
36 395 normalized ratios of P, Pb, Ta, and Nb varying by close to one order of magnitude (Fig.  
37  
38  
39 396 4C). In addition, hydrothermal magnetite from the Reko Diq Cu-Au deposit has the  
40  
41  
42 397 highest Y, P, Pb, Ge, W, and Mo contents, whereas that from the Porgera Au-Cu  
43  
44  
45 398 deposit has the lowest W, Cu, Ga, Ti, and V contents (Fig. 4D).

46  
47 399 Box and whisker plot of trace element contents in igneous and hydrothermal  
48  
49  
50 400 magnetite shows that EPMA mean values for hydrothermal magnetite are higher for  
51  
52  
53 401 Si, K, Sn, Cu, and Ni, but lower for Ca, Al, Mn, Mg, Ti, Zn, and V contents (Fig. 5A).  
54  
55  
56 402 LA-ICP-MS analyses show that hydrothermal magnetite has higher Pb, Ge, W, Sc, Cu,  
57  
58  
59 403 Mo, Ga, Co, and Ni but lower Ca, Y, P, Zr, Hf, Al, Ta, Nb, Sn, Mn, Mg, Ti, Zn, V, and  
60  
61  
62  
63  
64  
65

1 404 Cr contents compared to igneous magnetite (Fig. 5B).

2  
3 405

4  
5  
6 406 *Compositional comparison for magnetite from different deposit subtypes*

7  
8  
9 407 There is some overlapping of igneous/hydrothermal magnetite composition between

10  
11 408 different deposit subtypes in terms of the large compositional variations. However,

12  
13 409 significant differences can be identified in terms of the average composition for

14  
15 410 different deposit subtypes. EPMA analyses show that igneous magnetite from

16  
17 411 porphyry Cu-Au deposits has higher Mn, Mg, Ti, and Zn average contents than that

18  
19 412 from porphyry Cu-Mo and Cu-Mo-Au deposits (Fig. 6A). Igneous magnetite from

20  
21 413 porphyry Cu-Mo deposits shows higher V and Cr average contents than that from the

22  
23 414 other two deposit types, whereas that from porphyry Cu-Mo-Au deposits is

24  
25 415 characterized by relatively high K contents (Fig. 6A). Limited LA-ICP-MS data (four

26  
27 416 and seven analyses for porphyry Cu-Au and Cu-Mo, respectively) suggest that

28  
29 417 igneous magnetite from porphyry Cu-Au deposits has higher Si, Ca, Y, Pb, Al, W, Ta,

30  
31 418 Nb, Mo, Sn, Mn, Mg, Ti, Zn and Co average contents than that from porphyry Cu-Mo

32  
33 419 deposits (Fig. 6B).

34  
35 420 EPMA analyses show that hydrothermal magnetite from porphyry Au-Cu deposits

36  
37 421 has higher Mg and Ti average contents than that from other deposit types, whereas

38  
39 422 that from porphyry Cu-Mo deposits has relatively high Cu and Cr contents (Fig. 6C).

40  
41 423 Hydrothermal magnetite from porphyry Cu-Mo-Au deposits has slightly higher K, Zn,

42  
43 424 and Ni average contents than that from other deposit types, whereas that from the

44  
45 425 porphyry W-Mo deposit has relatively high Si, Ca, Al, and Sn concentrations (Fig.

1 426 6C). Hydrothermal magnetite from the porphyry Cu-Au and Mo deposits has  
2  
3 427 intermediate trace element contents compared to other deposit types (Fig. 6C). The  
4  
5  
6 428 LA-ICP-MS data of hydrothermal magnetite is from four deposit subtypes, porphyry  
7  
8  
9 429 Au-Cu, Cu-Au, Cu-Mo, and Cu-Mo-Au. Hydrothermal magnetite from porphyry  
10  
11 430 Au-Cu deposits shows relatively high Zr, Nb, and Mn contents, whereas that from the  
12  
13  
14 431 porphyry Cu-Au deposits has higher Y, P, Pb, Hf, W, Sc, Ta, Mo, Ti, and Cr contents  
15  
16  
17 432 (Fig. 6D). Hydrothermal magnetite from porphyry Cu-Mo deposits has higher Ca and  
18  
19  
20 433 Cu contents, whereas that from Cu-Mo-Au deposits shows relatively high Ni and Cr  
21  
22  
23 434 contents (Fig. 6D).  
24  
25  
26 435

## 28 436 **Multivariate Statistical Analysis of Magnetite Composition**

### 30 437 *Igneous and hydrothermal magnetite*

31  
32  
33 438 Figure 7 shows the PLS-DA results of EPMA and LA-ICP-MS data classified by  
34  
35  
36 439 magmatic and hydrothermal magnetite. PLS-DA of EPMA data shows that in contrast  
37  
38  
39 440 to hydrothermal magnetite that is dispersed in the  $t_1$ - $t_2$  space, igneous magnetite is  
40  
41  
42 441 mainly isolated in the high  $t_1$  region because of a positive correlation between V and  
43  
44  
45 442 Ti that are negatively correlated to Si and Ca (Figs. 7A-B, E-H). However, there is  
46  
47  
48 443 significant compositional overlap between igneous and hydrothermal magnetite (Fig.  
49  
50  
51 444 7B) in terms of score contributions of Mg, Mn, Al, and Zn (Figs. 7E-F). Figures 7C-D  
52  
53 445 show PLS-DA results of LA-ICP-MS data that uses a higher number of elemental  
54  
55  
56 446 variables to differentiate between igneous and hydrothermal magnetite. Igneous  
57  
58  
59 447 magnetite mainly plots in the high  $t_1$ ,  $t_2$  region due to positive correlation among V, Zr,

1 448 P, Ti, Nb, and Mn, which are negatively correlated to Mg, Si, Co, Ni, Ge, Sb, W and  
2  
3 449 Pb (Figs. 7C-D, G-H). It is worth noting that V is more efficient than Ti in  
4  
5  
6 450 discriminating between igneous and hydrothermal magnetite, as shown by the higher  
7  
8  
9 451 score contribution for V (Figs. 7G-H). Score contribution plots show that contrasting  
10  
11  
12 452 element contributions discriminate igneous from hydrothermal magnetite (Figs.  
13  
14 453 7E-H).

15  
16  
17 454

18  
19  
20 455 *Deposit subtypes-igneous magnetite*

21  
22 456 Figure 8 shows the PLS-DA results of EPMA data of igneous magnetite classified  
23  
24  
25 457 by three deposit types, Cu-Au, Cu-Mo, and Cu-Mo-Au. Igneous magnetite from  
26  
27  
28 458 Cu-Au deposits mainly plots at positive  $t_1$  due to correlated Mg and Al (Fig. 8A-C),  
29  
30  
31 459 whereas that from Cu-Mo deposits plots in the negative  $t_2$  side due to correlated Mn,  
32  
33  
34 460 V and Ca (Fig. 8B, D). Igneous magnetite from the Cu-Mo-Au deposits plots in the  
35  
36  
37 461 negative  $t_1$ , positive  $t_2$  region due to correlated V and Ca (Fig. 8B, E). In general,  
38  
39  
40 462 igneous magnetite from the three subtypes of deposits cannot be well discriminated  
41  
42  
43 463 from each other because of overlap in  $t_1$ - $t_2$  space. The VIP plot indicates that V and Al  
44  
45  
46 464 are the most important discriminant elements for these three deposit subtypes (Fig.  
47  
48  
49 465 8F). Titanium is important to discriminate Cu-Mo-Au deposits, whereas Si is useful to  
50  
51  
52 466 discriminate Cu-Mo deposits (Fig. 8F). Magnesium is the important variable for  
53  
54  
55 467 Cu-Au deposits (Fig. 8F). Due to the limited number ( $n = 11$ ) of LA-ICP-MS analyses  
56  
57  
58 468 for igneous magnetite and the larger number ( $n = 25$ ) of element variables than that of  
59  
60  
61 469 analyses, PLS-DA of LA-ICP-MS data was not attempted.

1 470

2  
3 471 *Deposit subtypes-hydrothermal magnetite*

4  
5  
6 472 **Figure 9** shows PLS-DA results of EPMA data for hydrothermal magnetite classified  
7  
8  
9 473 by deposit subtypes. Hydrothermal magnetite from porphyry W-Mo deposit plots in  
10  
11  
12 474 the negative  $t_2$  side and can be discriminated from other deposit subtypes due to  
13  
14 475 correlated Si and Al (**Figs. 9A-B**). Hydrothermal magnetite from the porphyry Mo  
15  
16  
17 476 deposit mainly plots at positive  $t_1$  due to correlated Ti and Mg in spite of overlap with  
18  
19  
20 477 that from porphyry Cu-Au deposits (**Figs. 9A-B**). Hydrothermal magnetite from  
21  
22  
23 478 porphyry Au-Cu, Cu-Au, Cu-Mo, and Cu-Mo-Au deposits is scattered in the  $t_1$ - $t_2$  plot  
24  
25  
26 479 and cannot be discriminated from each other (**Figs. 9A-B**). However, hydrothermal  
27  
28  
29 480 magnetite from porphyry Au-Cu deposits can be roughly discriminated from other  
30  
31  
32 481 deposit subtypes in the  $t_1$ - $t_3$  plot by high Mg score (**Figs. 9C-D**). Score contribution  
33  
34  
35 482 plots indicate that hydrothermal magnetite from different deposit subtypes has  
36  
37  
38 483 specific trace element characteristics relative to the whole dataset. For example,  
39  
40  
41 484 hydrothermal magnetite from porphyry Au-Cu deposits is discriminated by a positive  
42  
43  
44 485 contribution of Mg (**Fig. 9E**), whereas that from the Cu-Au and Mo deposits is mainly  
45  
46  
47 486 discriminated by positive contributions of Ti, Al and Mg (**Fig. 9F, I**). Positive  
48  
49  
50 487 contributions of V, Ca, and Si characterize hydrothermal magnetite from porphyry  
51  
52  
53 488 Cu-Mo deposits (**Fig. 9G**), whereas positive contributions of Zn, Al, Si, and Mg are  
54  
55  
56 489 typical of hydrothermal magnetite from porphyry Cu-Mo-Au deposits (**Fig. 9H**).  
57  
58  
59 490 Hydrothermal magnetite from porphyry W-Mo deposits is distinguished by positive  
60  
61  
62 491 contributions of Al and Si (**Fig. 9J**). The VIP plot indicates that Si is an important

1 492 discriminant element for all deposit subtypes with the exception of Au-Cu deposits,  
2  
3 493 whereas Mg is important for discriminating all deposit subtypes with the exception of  
4  
5  
6 494 W-Mo deposits (Fig. 9K). Zinc and Al are important in discriminating hydrothermal  
7  
8  
9 495 magnetite from the Cu-Mo-Au and W-Mo deposits, although Al is also important for  
10  
11  
12 496 Au-Cu deposits (Fig. 9K). Vanadium is an important discriminant element for Cu-Au  
13  
14  
15 497 and Mo deposits (Fig. 9K).

16  
17 498 Figure 10 shows the PLS-DA results of LA-ICP-MS data of hydrothermal  
18  
19  
20 499 magnetite classified by four deposit subtypes, Au-Cu, Cu-Au, Cu-Mo, and Cu-Mo-Au.  
21  
22  
23 500 Hydrothermal magnetite from the Au-Cu deposits plots in the negative  $t_1$  side due to  
24  
25  
26 501 correlated Mg, Mn, Co, Zr, Nb, Sn, and Hf, whereas that from Cu-Au deposits mainly  
27  
28  
29 502 plots in the positive  $t_1$ , negative  $t_2$  region due to correlated Al, Sc, Ti, W, Pb, and Y  
30  
31  
32 503 (Figs. 10A-B). Hydrothermal magnetite from Cu-Mo and Cu-Mo-Au deposits plots in  
33  
34  
35 504 the positive  $t_1$ , positive  $t_2$  region because of correlated Ga, V, Cu, Sb, and Ge (Figs.  
36  
37  
38 505 10A-B). Hydrothermal magnetite from Au-Cu, Cu-Au, and Cu-Mo-Au deposits can  
39  
40  
41 506 be discriminated from each other, whereas hydrothermal magnetite from Cu-Mo  
42  
43  
44 507 deposits partly overlaps those from Cu-Au and Cu-Mo-Au deposits. Score  
45  
46  
47 508 contribution plots show that positive contributions of Mg, Mn, Co, Zr, Nb, Sn, and Hf  
48  
49  
50 509 discriminate hydrothermal magnetite from the Au-Cu deposits, whereas positive  
51  
52  
53 510 contributions of Sc, Al, Ti, V, Ga, Ta, W, and Pb characterize hydrothermal magnetite  
54  
55  
56 511 from Cu-Au deposits (Figs. 10C-D). Hydrothermal magnetite from Cu-Mo deposits is  
57  
58  
59 512 discriminated by positive contributions of Ca, V, Mn, Cu, Zn, Ga, and W, whereas that  
60  
61  
62 513 from Cu-Mo-Au deposits is separated by positive contributions of V, Co, Ni, Zn, and



1 514 Ga (Figs. 10E-F). The VIP plot indicates that Sc, Mn, and Co are important  
2  
3 515 discriminant elements for all deposit subtypes (Fig. 10G). Aluminum and Sn are  
4  
5  
6 516 important in discriminating Au-Cu, Cu-Mo, and Cu-Mo-Au deposits, whereas V, Ga,  
7  
8  
9 517 Zr, and Nb are important discriminant elements for Au-Cu and Cu-Au deposits (Fig.  
10  
11 518 10G).

12  
13  
14 519

15  
16  
17 520 *Magmatic affinity-igneous magnetite*

18  
19  
20 521 Figure 11 shows the PLS-DA results of EPMA data of igneous magnetite classified  
21  
22 522 by magmatic affinity. In spite of overlapping in  $t_1$ - $t_2$  space, igneous magnetite  
23  
24  
25 523 associated with alkaline intrusions plots in the positive  $t_2$  side due to correlated Si and  
26  
27  
28 524 Al (Figs. 11A-C), whereas that associated with high-K calc-alkaline intrusions plots in  
29  
30  
31 525 the positive  $t_1$ , negative  $t_2$  region due to correlated Ti, Mg, and Al (Figs. 11A-B, E).  
32  
33  
34 526 Igneous magnetite associated with calc-alkaline intrusions is scattered in the  $t_1$ - $t_2$  plot,  
35  
36  
37 527 characterized by positive contributions of Zn, V, and Ca (Figs. 11A-B, D). The VIP  
38  
39 528 plot shows that Al is important to discriminate all types of igneous magnetite (Fig.  
40  
41  
42 529 11F). Zinc and Ca are useful discriminant elements for igneous magnetite associated  
43  
44  
45 530 with calc-alkaline and high-K calc-alkaline intrusions (Fig. 11F). Vanadium is only  
46  
47  
48 531 useful in discriminating igneous magnetite associated with calc-alkaline intrusions,  
49  
50  
51 532 whereas Si is useful in discriminating igneous magnetite associated with alkaline and  
52  
53 533 high-K calc-alkaline intrusions (Fig. 11F). PLS-DA of LA-ICP-MS was not  
54  
55  
56 534 performed due to limited data for igneous magnetite grouped by magmatic affinity.

57  
58  
59 535

1 536 *Magmatic affinity-hydrothermal magnetite*  
2  
3 537 PLS-DA of EPMA data shows that hydrothermal magnetite associated with high-K  
4  
5  
6 538 calc-alkaline intrusions mainly plots at negative  $t_2$  due to correlated Al and Mn (Figs.  
7  
8  
9 539 12A-B). Hydrothermal magnetite associated with alkaline and calc-alkaline intrusions  
10  
11 540 is scattered in  $t_1$ - $t_2$  space. In general, hydrothermal magnetite associated with  
12  
13 541 intrusions of different magmatic affinities cannot be discriminated from each other  
14  
15 542 from EPMA data (Fig. 12B). Score contribution plots show that positive contribution  
16  
17 543 of Mg discriminates hydrothermal magnetite associated with alkaline intrusions,  
18  
19 544 whereas positive contributions of Zn, V, Ca, and Si discriminate that associated with  
20  
21 545 calc-alkaline intrusions (Figs. 12C-D). Hydrothermal magnetite associated with  
22  
23 546 high-K calc-alkaline intrusions is discriminated by positive contributions of Mn, Ti,  
24  
25 547 and Al (Fig. 12E). The VIP plot shows that Al and Mg are important discriminating  
26  
27 548 elements for hydrothermal magnetite associated with intrusions of all magmatic  
28  
29 549 affinities (Fig. 12F). Zinc and Ti discriminate hydrothermal magnetite associated with  
30  
31 550 calc-alkaline and high-K calc-alkaline intrusions (Fig. 12F).  
32  
33  
34  
35  
36  
37  
38  
39  
40  
41

42 551 LA-ICP-MS data yield a better classification for hydrothermal magnetite associated  
43  
44 552 with intrusions of different magmatic affinities (Figs. 13A-B). Hydrothermal  
45  
46 553 magnetite associated with alkaline intrusions is discriminated by positive  
47  
48 554 contributions of Mg, Mn, Co, Zr, Nb, Mo, Sn, Hf, and Ta (Figs. 13A-C), whereas that  
49  
50 555 associated with calc-alkaline intrusions is discriminated by positive contributions of V,  
51  
52 556 Ni, Cu, Ga, Ge, Sb, and W (Figs. 13A, B, D). Hydrothermal magnetite associated with  
53  
54 557 high-K calc-alkaline intrusions plots at positive  $t_2$  due to correlated Sc, Ti, Al, Ta, and  
55  
56  
57  
58  
59  
60  
61  
62  
63  
64  
65

1 558 Hf (Figs. 13A-B, E). The VIP plot shows that V, Ni, Ga, and Ta are important  
2  
3 559 discriminant elements for all types of hydrothermal magnetite (Fig. 13F). Magnesium,  
4  
5  
6 560 Mn, Cu, Zr, Nb, Sn, Hf, and W are useful in discriminating hydrothermal magnetite  
7  
8  
9 561 associated with alkaline and calc-alkaline intrusions (Fig. 13F). Aluminum, Co, and  
10  
11  
12 562 Mo are only useful in discriminating hydrothermal magnetite associated with high-K  
13  
14 563 calc-alkaline intrusions (Fig. 13F). Scandium and Ti are useful in discriminating  
15  
16  
17 564 hydrothermal magnetite associated with alkaline and high-K calc-alkaline intrusions  
18  
19  
20 565 (Fig. 13F).

21  
22  
23 566

24  
25 567 *Porphyry composition-igneous magnetite*

26  
27  
28 568 PLS-DA of EPMA data of igneous magnetite shows that intermediate porphyry  
29  
30 569 cannot be separated from felsic porphyry in the  $t_1$ - $t_2$  space (Figs. 14A-B). Igneous  
31  
32  
33 570 magnetite from intermediate porphyry is scattered in the  $t_1$ - $t_2$  space with positive  
34  
35  
36 571 contributions of Al, Si, and Mg (Fig. 14C), whereas that from felsic porphyry plots in  
37  
38  
39 572 the negative  $t_1$  region (Figs. 14A-B) due to positive contributions of Mn and V (Fig.  
40  
41  
42 573 14D). Because there are only four and seven LA-ICP-MS analyses for igneous  
43  
44  
45 574 magnetite from intermediate and felsic porphyry, respectively, PLS-DA was not  
46  
47  
48 575 performed on igneous magnetite grouped by porphyry composition.

49  
50 576

51  
52  
53 577 *Porphyry composition-hydrothermal magnetite*

54  
55  
56 578 Figure 15 shows PLS-DA results of EPMA data of hydrothermal magnetite related to  
57  
58  
59 579 different porphyry composition. Hydrothermal magnetite related to mafic porphyry

1 580 can be discriminated from that related to intermediate and felsic porphyry due to  
2  
3 581 positive contribution of Mg and Mn (Figs. 15A-C). However, hydrothermal magnetite  
4  
5  
6 582 related to intermediate and felsic porphyry cannot be separated from each other in the  
7  
8  
9 583  $t_1$ - $t_2$  space (Figs. 15A-B). Score contribution plots show that hydrothermal magnetite  
10  
11  
12 584 related to intermediate porphyry is characterized by positive contributions of Mg and  
13  
14 585 Al (Fig. 15D), whereas that related to felsic porphyry is characterized by weakly  
15  
16  
17 586 positive contributions of Si, Ca, and V (Fig. 15E). Magnesium and Al are the most  
18  
19  
20 587 important discriminant elements for three types of porphyry, whereas Mn is only  
21  
22  
23 588 useful in discriminating mafic porphyry (Fig. 15F).

24  
25 589 PLS-DA of LA-ICP-MS data of hydrothermal magnetite shows that mafic,  
26  
27  
28 590 intermediate, and felsic porphyries are discriminated from each other. Hydrothermal  
29  
30  
31 591 magnetite related to mafic porphyry plots in the negative  $t_1$  region (Figs. 16A-B),  
32  
33  
34 592 because of positive contributions of Mg, Mn, Co, Zr, Nb, Mo, Sn, and Hf (Fig. 16C).  
35  
36  
37 593 Hydrothermal magnetite related to intermediate porphyry mainly plots in the positive  
38  
39 594  $t_1$ , positive  $t_2$  region due to positive contributions of Al, Sc, Ti, V, Ga, Sn, and Pb (Fig.  
40  
41  
42 595 16D), whereas that related to felsic porphyry plots in the positive  $t_1$ , negative  $t_2$  region  
43  
44  
45 596 due to positive contributions of Ca, Mn, Cu, Zn, and W (Fig. 16E). VIP plot shows  
46  
47  
48 597 that Mg, Al, Ti, and Mn are the most important discriminant elements for three  
49  
50  
51 598 different porphyries (Fig. 16F). Vanadium, Ga, Zr, and Nb are useful in discrimination  
52  
53  
54 599 between mafic and intermediate porphyries, whereas Cu, Zn, Sn, W, and Pb are  
55  
56 600 important to discriminate between intermediate and felsic porphyries (Fig. 16F).  
57  
58  
59 601 Calcium and Ta are only useful in discriminating hydrothermal magnetite related to

1 602 felsic porphyry (Fig. 16F).  
2  
3

4 603  
5

## 6 604 **Discussion**

### 7 8 9 605 *Igneous versus hydrothermal processes*

10  
11 606 The compositional variations of igneous magnetite are mainly attributed to the  
12  
13 607 conditions of temperature,  $fO_2$ , and  $fS_2$ , melt composition, cooling rate, sub-solidus  
14  
15 608 re-equilibration processes, and element partitioning with co-precipitated minerals  
16  
17 609 (Buddington and Lindsley, 1964; Ghiorso and Sack, 1991; Frost and Lindsley, 1992;  
18  
19 610 Dare et al., 2012, 2014; Nadoll et al., 2014). Experimental studies have demonstrated  
20  
21 611 that magnetite-melt or magnetite-mineral partition coefficients of elements in igneous  
22  
23 612 magnetite depend mostly on temperature, host rock/melt composition, and  
24  
25 613 oxygen/sulfur fugacity (Toplis and Corgne, 2002; Sievwright et al., 2017; Sossi et al.,  
26  
27 614 2018) and can vary across three to five orders of magnitude for a specific element  
28  
29 615 (Dare et al., 2012; Nadoll et al., 2014). Despite the limited experimental works  
30  
31 616 available on partitioning of trace elements between magnetite and hydrothermal fluids  
32  
33 617 (Chou and Eugster, 1977; Ilton and Eugster, 1989; Simon et al., 2004), the  
34  
35 618 composition of hydrothermal magnetite appears to be controlled by the fluid  
36  
37 619 composition (element availability), temperature,  $fO_2$  and  $fS_2$ , and host rock buffering  
38  
39 620 (Nadoll et al., 2014). Hydrothermal magnetite has higher Si, K, Pb, Ge, W, Sc, Cu,  
40  
41 621 Mo, Ga, Co, and Ni but lower Ca, Y, P, Zr, Hf, Al, Ta, Nb, Mn, Mg, Ti, Zn, and V  
42  
43 622 contents than igneous magnetite in terms of average values (Figs. 5A-B). PLS-DA  
44  
45 623 results show that relatively high Mg, Si, Ca, Co, Ni, Ge, Sb, W, and Pb discriminates  
46  
47  
48  
49  
50  
51  
52  
53  
54  
55  
56  
57  
58  
59  
60  
61  
62  
63  
64  
65

1 624 hydrothermal magnetite, whereas relatively high P, Ti, V, Mn, Zr, Nb, Hf, and Ta  
2  
3 625 discriminates igneous magnetite (Fig. 7). In this section, we discuss the main factors  
4  
5  
6 626 controlling the compositional differences between igneous and hydrothermal  
7  
8  
9 627 magnetite.

10  
11 628 The observation that Ti and V contents are higher in igneous magnetite compared  
12  
13 629 to hydrothermal magnetite in porphyry systems is consistent with the study of Nadoll  
14  
15  
16 630 et al. (2015) that focuses on both porphyry and skarn systems. The Ti vs. V diagram  
17  
18  
19 631 was proposed to discriminate igneous from hydrothermal magnetite based on this  
20  
21  
22 632 observation (Nadoll et al., 2015). This observation is also consistent with findings that  
23  
24  
25 633 magmatic magnetite from Fe-Ti-(V) deposits commonly have Ti+V contents higher  
26  
27  
28 634 than hydrothermal magnetite from magmatic-hydrothermal deposits such as IOCG  
29  
30  
31 635 and porphyry Cu (Dupuis and Beaudoin, 2011). Higher Ti and V contents in igneous  
32  
33  
34 636 magnetite are likely due to strong compatibility of Ti and V in magnetite crystallized  
35  
36  
37 637 from silicate melt ( $D_{Ti} = 7.0$ ,  $D_V = 26$ ; Dare et al., 2012) and relatively lower  
38  
39  
40 638 solubility of these elements in aqueous fluids (Mysen, 2012). Because the partition of  
41  
42  
43 639 Ti and V into magnetite is preferred with increasing temperature and decreasing  
44  
45  
46 640 oxygen fugacity, respectively (Nielsen et al., 1994; Toplis and Carroll, 1995; Toplis  
47  
48  
49 641 and Corgne, 2002; Sievwright et al., 2017), decreased Ti and V contents from igneous  
50  
51  
52 642 to hydrothermal magnetite reflect decreasing temperature and increasing oxygen  
53  
54  
55 643 fugacity from magmatic to hydrothermal process.

56 644 Phosphorus is incompatible in igneous magnetite ( $D_P = 0.0028$ ; Dare et al., 2012)  
57  
58  
59 645 and therefore tends to concentrate in late magma after progressive fractional  
60  
61  
62  
63  
64  
65

1 646 crystallization, for example, to form Fe-Ti-P mineralization. Phosphorus contents in  
2  
3 647 both igneous and hydrothermal magnetite are commonly below detection limit and  
4  
5  
6 648 rarely reported (Dare et al., 2014). The slightly higher P in igneous magnetite  
7  
8  
9 649 compared to hydrothermal magnetite may be related to highly differentiated granitic  
10  
11 650 magma rich in P. Igneous magnetite is generally rich in high field strength elements  
12  
13 651 (HFSE)-Zr, Hf, Nb, and Ta, relative to hydrothermal magnetite. This observation is  
14  
15  
16  
17 652 consistent with the result of Dare et al. (2014). Because HFSE are relatively  
18  
19  
20 653 incompatible in magnetite ( $D_{Zr} = 0.2$ ,  $D_{Hf} = 0.25$ ,  $D_{Nb} = 0.1$ ,  $D_{Ta} = 0.2$ ; Dare et al.,  
21  
22 654 2012), these metals are preferentially incorporated into late igneous magnetite  
23  
24  
25 655 crystallized from the most evolved magmas. Moreover, the HFSE are considered  
26  
27  
28 656 relatively immobile during alteration at low metamorphic grades and low water/rock  
29  
30  
31 657 ratios (Pearce and Cann, 1973; Floyd and Winchester, 1978; Middelburg et al., 1988)  
32  
33  
34 658 and thus have low solubility in hydrothermal fluids under the P-T conditions that  
35  
36 659 prevail during the formation of porphyry deposits. Thus, the low mobility of HFSE  
37  
38  
39 660 under hydrothermal conditions perhaps explains their low concentrations in most  
40  
41  
42 661 magmatic-hydrothermal fluids.

43  
44 662 Silicon and Ca are extremely incompatible in igneous magnetite crystallized from  
45  
46  
47 663 silicate melts ( $D_{Si} = 0.0017$ ,  $D_{Ca} = 0.035$ ; Dare et al., 2012). Although no partition  
48  
49  
50 664 coefficients of Si and Ca between magnetite and hydrothermal fluids are available, Si-  
51  
52  
53 665 and/or Ca- rich (e.g., ~1-6 wt%) hydrothermal magnetite is commonly found in skarn  
54  
55  
56 666 deposits (Westendorp et al., 1991; Shimazaki, 1998; Ciobanu and Cook, 2004; Dupuis  
57  
58  
59 667 and Beaudoin, 2011; Hu et al., 2015; Huang et al., 2018b). This suggests that Si and

1 668 Ca are highly mobile during hydrothermal alteration and tends to be enriched in  
2  
3 669 magnetite precipitated from hydrothermal fluids. However, some magnetite grains  
4  
5  
6 670 with high Si and Ca contents in fact contain nanometer-scale mineral inclusions  
7  
8  
9 671 (Deditius et al., 2018).

10  
11 672 Hydrothermal magnetite from porphyry deposits is rich in Ge, Sb, Pb, and W  
12  
13 673 relative to igneous magnetite. These elements are incompatible to weakly compatible  
14  
15 674 in magmatic magnetite ( $D_{\text{Ge}} = 0.11$ ,  $D_{\text{Sb}} = 0.35$ ,  $D_{\text{Pb}} = 1.4$ ,  $D_{\text{W}} = 2.3$ ). Meng et al.  
16  
17 675 (2017) interpreted the enrichment of Ge in hydrothermal magnetite from skarn, IOCG,  
18  
19  
20 676 and volcanic-hosted hydrothermal deposits, relative to igneous magnetite from  
21  
22  
23 677 magmatic Fe-Ti oxide and Ni-Cu sulfide deposits, as caused by higher oxygen  
24  
25  
26 678 fugacity. The elevated W, Pb, As, Mo, and Sn concentrations in altered magnetite  
27  
28  
29  
30 679 from BIF-hosted high grade iron deposits were attributed to hydrothermal  
31  
32  
33 680 metasomatism related to the granitic rocks (Nadoll et al., 2014). Germanium, Sb, and  
34  
35  
36 681 Pb are also chalcophile and more likely to partition into coexisting sulfides such as  
37  
38  
39 682 chalcopyrite and pyrite (Bernstein, 1985; Dare et al., 2012; Meng and Hu, 2018).  
40  
41  
42 683 Minor amounts of these elements in hydrothermal magnetite co-precipitating with  
43  
44  
45 684 Fe-Cu sulfides may reflect relative enrichment of these elements in fluids.  
46  
47  
48 685 Considering that these elements have high solubility in hydrothermal fluids, in  
49  
50  
51 686 particular at intermediate to high temperatures ( $>300^{\circ}\text{C}$ ) (Hemley and Hunt, 1992), it  
52  
53  
54 687 is likely that hydrothermal fluids exsolved from porphyry-associated intrusions may  
55  
56 688 have a major control on the contents of Ge, Sb, Pb, and W in hydrothermal magnetite  
57  
58  
59 689 from porphyry deposits.



1 690 Transition metals, Co and Ni, are strongly compatible in magnetite crystallized  
2  
3 691 from silicate melt ( $D_{\text{Co}} = 7.5$ ,  $D_{\text{Ni}} = 30$ ; Dare et al., 2012) and are expected to be in  
4  
5  
6 692 high concentration in igneous magnetite. In contrast to sulfide-deficient mineral  
7  
8  
9 693 assemblage of igneous magnetite, hydrothermal magnetite in porphyry deposits is  
10  
11  
12 694 commonly crystallized with chalcopyrite and pyrite that scavenge or preferentially  
13  
14  
15 695 incorporate chalcophile elements such as Co and Ni from fluids (Dare et al., 2012). It  
16  
17  
18 696 is thus expected that hydrothermal magnetite in sulfide-bearing veins should be  
19  
20  
21 697 depleted in Co and Ni relative to igneous magnetite. However, Co and Ni contents are  
22  
23  
24 698 relatively higher in hydrothermal magnetite compared to igneous magnetite (Figs. 5B  
25  
26  
27 699 and 7). Nadoll et al. (2015) showed that there are no obvious differences in Co  
28  
29  
30 700 contents (~40 ppm) between igneous and hydrothermal magnetite from porphyry  
31  
32  
33 701 deposits. Considering that porphyry systems are hosted by a variety of igneous,  
34  
35  
36 702 sedimentary, and metamorphic rocks (Table 1), the relative enrichment of Co and Ni  
37  
38  
39 703 in hydrothermal magnetite is most likely due to interaction of hydrothermal fluids  
40  
41  
42 704 with mafic volcanic rocks or magmatic sulfides. This is consistent with hydrothermal  
43  
44  
45 705 magnetite from mafic porphyry that has higher Co content than those from  
46  
47  
48 706 intermediate and felsic porphyries (Fig. 16C).

49  
50 707 Hydrothermal magnetite is relatively rich in Mg but depleted in Mn compared to  
51  
52  
53 708 igneous magnetite. The low score contributions for Mn (Figs. 7E-H) indicate subtle  
54  
55  
56 709 differences in Mn contents between igneous and hydrothermal magnetite, and that Mn  
57  
58  
59 710 is not as important as Mg in discriminating magmatic from hydrothermal magnetite.  
60  
61  
62 711 Elements such as Mg and Mn can be enriched in hydrothermal fluids by extensive

1 712 fluid/rock interactions (Einaudi et al., 1981; Meinert et al., 2005), as suggested by  
2  
3 713 relatively high Mg and Mn contents in skarn magnetite (Nadoll et al., 2015; Zhao and  
4  
5  
6 714 Zhou, 2015; Huang et al., 2016, 2018b). Considering that mafic porphyry is involved  
7  
8  
9 715 in the formation of hydrothermal magnetite, the higher Mg in hydrothermal magnetite  
10  
11  
12 716 is thus explained by host rock buffering because hydrothermal magnetite related to  
13  
14  
15 717 mafic porphyry is rich in Mg and Mn relative to those related to intermediate and  
16  
17 718 felsic porphyries (Figs. 15 and 16).

18  
19  
20 719

21  
22  
23 720 *Discrimination diagrams for igneous and hydrothermal magnetite*

24  
25 721 PLS-DA of EPMA data shows that igneous magnetite cannot be discriminated from  
26  
27  
28 722 hydrothermal magnetite in the  $t_1$ - $t_2$  space (Fig. 7B). In spite of overlapping, positive  
29  
30  
31 723 contributions of Si and Ca discriminate hydrothermal magnetite, whereas positive  
32  
33  
34 724 contributions of Ti and V characterize igneous magnetite (Figs. 7E-F). PLS-DA of  
35  
36  
37 725 LA-ICP-MS data, covering a larger number of elements, shows a clear separation  
38  
39  
40 726 between igneous and hydrothermal magnetite (Fig. 7D). The most important  
41  
42  
43 727 discrimination elements for igneous magnetite are V and Zr, whereas those for  
44  
45  
46 728 hydrothermal magnetite are Mg, Si, Ge, and Sb (Figs. 7G-H). The different  
47  
48  
49 729 discrimination ability of magnetite between EPMA and LA-ICP-MS data is related to  
50  
51  
52 730 the larger number of variables (i.e., elements), but perhaps also to the smaller number  
53  
54  
55 731 of samples analyzed by LA-ICP-MS. Therefore, the boundary between igneous and  
56  
57  
58 732 hydrothermal magnetite is preliminary (Fig. 7D) and should be confirmed by more  
59  
60  
61 733 data.

1 734 Dare et al. (2014) proposed a Ti versus Ni/Cr discriminant diagram to distinguish  
2  
3 735 magnetite from igneous to hydrothermal origin. This diagram is constructed based on  
4  
5  
6 736 the different behavior of Ni and Cr in magmatic and hydrothermal systems. Nickel  
7  
8  
9 737 and Cr are coupled in silicate magmas with Ni/Cr ratios lower than 1 because they  
10  
11  
12 738 behave compatibly during fractionation of intermediate and felsic melts, whereas they  
13  
14  
15 739 are decoupled in many hydrothermal systems with higher Ni/Cr ratios likely due to a  
16  
17 740 higher solubility of Ni compared to Cr in fluids (Dare et al., 2014). EPMA data show  
18  
19  
20 741 that most of hydrothermal magnetite grains plot in the hydrothermal field (Fig. 17A).  
21  
22  
23 742 However, some hydrothermal magnetite has lower Ni/Cr ratios than expected (Fig.  
24  
25 743 17A). Moreover, more than half of igneous magnetite plots in the hydrothermal field  
26  
27  
28 744 characterized by high Ni/Cr ratios. LA-ICP-MS data show that all igneous magnetite  
29  
30  
31 745 plot in the magmatic field but that some hydrothermal magnetite plot in both  
32  
33  
34 746 magmatic and hydrothermal fields (Fig. 17B). Our results are consistent with the  
35  
36  
37 747 observation of Knipping et al. (2015) that the Ti versus Ni/Cr diagram is not very  
38  
39  
40 748 useful for discrimination between igneous and hydrothermal magnetite. Experimental  
41  
42  
43 749 studies showed that both  $\text{Cr}^{6+}$  and  $\text{Cr}^{3+}$  are more soluble than Ni in aqueous fluid at  
44  
45  
46 750 high temperature (magmatic conditions) (James, 2003; Watenphul et al., 2012, 2013),  
47  
48  
49 751 which would result in low Ni/Cr ratios for magmatic-hydrothermal magnetite.  
50  
51  
52 752 Moreover, low Cr concentration (high Ni/Cr) in magnetite is not necessary an  
53  
54  
55 753 indicator of hydrothermal origin, especially when considering that higher Ni values  
56  
57  
58 754 are expected in magmatic magnetite than in hydrothermal magnetite (Knipping et al.,  
59  
60  
61 755 2015).

1 756 Nadoll et al. (2015) proposed a simple binary Ti-V diagram to discriminate  
2  
3 757 between igneous and hydrothermal magnetite from porphyry and skarn deposits. They  
4  
5  
6 758 considered that igneous magnetite commonly has Ti contents above ~5000 ppm,  
7  
8  
9 759 whereas hydrothermal magnetite is characterized by lower Ti-V concentrations, in  
10  
11 760 spite of an overlap between igneous and hydrothermal magnetite. In the Ti-V plot,  
12  
13  
14 761 most EPMA data of igneous and hydrothermal magnetite from porphyry deposits plot  
15  
16  
17 762 in the overlapping field (Fig. 17C), whereas most hydrothermal magnetite  
18  
19  
20 763 LA-ICP-MS data plot in the igneous field (Fig. 17D). This suggests that in porphyry  
21  
22  
23 764 systems, the limit between igneous and hydrothermal processes is transitional and that  
24  
25  
26 765 part of the magnetite grains have a hydrothermal-igneous origin. This overlapping  
27  
28  
29 766 composition between igneous and hydrothermal magnetite is also observed in  
30  
31  
32 767 PLS-DA results (Fig. 7B). Moreover, microtextures show that some igneous  
33  
34  
35 768 magnetite grains have been replaced along grain margins and that some ilmenite  
36  
37  
38 769 lamellae have been altered to titanite (Figs. 1E-F). Wen et al. (2017) have  
39  
40  
41 770 demonstrated that igneous magnetite in altered granitic plutons is susceptible to  
42  
43  
44 771 textural and compositional reequilibration. The reequilibrated magnetite has  
45  
46  
47 772 geochemical patterns that may be different from its precursor (Wen et al., 2017),  
48  
49  
50 773 complicating the application of existing discrimination diagrams. This partly explains  
51  
52  
53 774 why the binary plots of Ti versus Ni/Cr and Ti versus V cannot efficiently  
54  
55  
56 775 discriminate igneous and hydrothermal magnetite in porphyry deposits.

57  
58 777 *Relationship between deposit subtypes and magnetite chemistry*  
59  
60  
61  
62  
63  
64  
65

1 778 As shown in [Figs. 8 and 9](#), both igneous and hydrothermal magnetite from Cu-Au,  
2  
3 779 Cu-Mo, and Cu-Mo-Au deposits cannot be discriminated from each other by EPMA  
4  
5  
6 780 data. However, hydrothermal magnetite from these deposits can be discriminated by  
7  
8  
9 781 LA-ICP-MS data in spite of minor overlap ([Fig. 10B](#)). In addition, PLS-DA of EPMA  
10  
11 782 and LA-ICP-MS data of hydrothermal magnetite shows that porphyry W-Mo and  
12  
13 783 Au-Cu deposits can be discriminated from other deposit subtypes ([Figs. 9 and 10](#)).  
14  
15  
16  
17 784 The discrimination between different subtypes of porphyry deposits suggests that the  
18  
19 785 composition of hydrothermal magnetite can reflect physical or chemical conditions  
20  
21  
22 786 responsible for the formation of these deposit types.

23  
24  
25 787 The composition of intrusions associated with porphyry deposits varies widely  
26  
27  
28 788 ([Table 1](#)) and appears to exert a fundamental control on the metal content of the  
29  
30 789 deposits (Sinclair, 2007; Sillitoe, 2010). Mo-rich porphyry Cu deposits (e.g., Butte  
31  
32  
33 790 and Escondida Norte, [Table 1](#)) are associated with more felsic intrusions, whereas  
34  
35  
36 791 Au-rich porphyry deposits tend to be related to more mafic intrusions, although  
37  
38 792 intrusions as felsic as quartz monzonite may also host Au-rich porphyry deposits (e.g.,  
39  
40  
41 793 Ridgeway, [Table 1](#); Sillitoe, 2010). Cu-poor porphyry Au deposits appear to occur  
42  
43  
44 794 exclusively in association with calc-alkaline diorite and quartz diorite porphyries (Vila  
45  
46  
47 795 and Sillitoe, 1991). Porphyry Mo (Climax-type), W-Mo, W, and Sn deposits are  
48  
49  
50 796 considered to be typically associated with felsic, high silica (72-77 wt% SiO<sub>2</sub>) and, in  
51  
52  
53 797 many cases, strongly differentiated granitic plutons (Sinclair, 2007). The relatively  
54  
55  
56 798 high Si and Al contents in hydrothermal magnetite from the Mount Pleasant porphyry  
57  
58  
59 799 W-Mo deposit ([Figs. 9J](#)) are thus likely due to the granitic composition of the host  
60  
61  
62  
63  
64  
65

1 800 intrusions (Table 1). This is consistent with that hydrothermal magnetite related to  
2  
3 801 felsic porphyry has higher Si contents than those related to mafic and intermediate  
4  
5  
6 802 porphyries (Figs. 15E and 16E). Intrusions associated with Endako-type porphyry Mo  
7  
8  
9 803 deposits range more widely in composition, from granodiorite to granite (Table 1;  
10  
11  
12 804 Sinclair, 2007), whereas porphyry Cu-Au, Cu-Mo, and Cu-Mo-Au deposits are hosted  
13  
14  
15 805 by intermediate intrusions (Table 1). Therefore, the overlapping composition of  
16  
17 806 hydrothermal magnetite from porphyry Mo (Endako), Cu-Au, Cu-Mo, and Cu-Mo-Au  
18  
19  
20 807 deposits (Figs. 9B, D and 10B) could be explained by similar and overlapping  
21  
22  
23 808 composition of their host intrusions. This is consistent with the significant  
24  
25  
26 809 compositional overlapping of hydrothermal magnetite associated with intermediate  
27  
28  
29 810 and felsic porphyry intrusions (Fig. 15B).

30  
31 811 The Porgera porphyry Au-Cu deposit is hosted by mafic intrusions, whereas the  
32  
33  
34 812 Sari Gunay and Ridgeway porphyry Au-Cu deposits are hosted by intermediate  
35  
36  
37 813 intrusions (Table 1). The more mafic composition of the host rocks may explain the  
38  
39  
40 814 high Mg and Mn in hydrothermal magnetite from Au-Cu deposits because these  
41  
42  
43 815 elements are more enriched in fluids related to mafic magma than those related to  
44  
45  
46 816 felsic magma (Figs. 15C and 16C). However, the relative enrichment of HFSE such as  
47  
48  
49 817 Zr, Nb, and Hf in Au-Cu deposit hydrothermal magnetite cannot be explained by a  
50  
51  
52 818 more mafic host rock composition because these elements are incompatible in  
53  
54  
55 819 magnetite (Dare et al., 2012) and tend to concentrate in more evolved magma and  
56  
57  
58 820 related fluids. Alternatively, other factor(s) such as fluid chemistry also play an  
59  
60  
61 821 important role. In the fluoride-rich alkaline magmatic systems, Zr and Nb can be

1 822 hydrothermally transported to form related Zr-REE-Nb deposits (Salvi and  
2  
3 823 Williams-Jones, 2006; Yang et al., 2014). Experimental studies also demonstrated that  
4  
5  
6 824 chloride and fluoride-bearing aqueous fluids (e.g., 20 wt% NaCl or 2 wt% NaF), at  
7  
8  
9 825 hydrothermal conditions, could remarkably improve HFSE solubility (Tanis et al.,  
10  
11 826 2015, 2016). Moreover, granitoid-hosted Mo and Sn deposits have an association with  
12  
13  
14 827 F-rich magmas or fluids and Mo and Sn along with Nb and Sc have a strong affinity  
15  
16  
17 828 to F in fluids (Webster and Holloway, 1990; Shchekina and Gramenitskii, 2008).  
18  
19  
20 829 Therefore, the relative enrichment of HFSE and Sn in hydrothermal magnetite from  
21  
22  
23 830 Au-Cu deposits and Sc in hydrothermal magnetite from porphyry Cu-Au deposits  
24  
25  
26 831 appears to be dominated by fluid chemistry (Cl/F). Because Au is commonly assumed  
27  
28  
29 832 to be in the form of chloride complexes in the hypersaline liquid phase (Henley, 1973;  
30  
31 833 Chou and Eugster, 1977), the high concentration of chloride in fluids is more likely  
32  
33  
34 834 the factor inducing the relative enrichment of HFSE in Au-rich porphyry  
35  
36  
37 835 hydrothermal magnetite. This is consistent with the generally high contents of  
38  
39  
40 836 halogens such as Cl and F of ore-bearing rocks in these deposits (Müller and Groves,  
41  
42 837 1993).

43  
44  
45 838 The oxidation state of granitic rocks, reflected by accessory minerals such as  
46  
47  
48 839 magnetite, ilmenite, pyrite, pyrrhotite, and anhydrite, also influences metal contents of  
49  
50  
51 840 related deposits (Ishihara, 1981). For example, porphyry Cu, Cu-Mo, Cu-Au, Au, Mo  
52  
53 841 (Climax-type), and W deposits are commonly associated with oxidized,  
54  
55  
56 842 magnetite-series plutons, whereas porphyry Sn deposits are related to reduced,  
57  
58  
59 843 ilmenite-series plutons (Sinclair, 2007). Granitic rocks hosting Endako-type Mo  
60  
61  
62  
63  
64  
65

1 844 deposits have oxidation state spanning both magnetite and ilmenite series (Sinclair,  
2  
3 845 2007). Because nearly all our studied deposits are associated with magnetite-series  
4  
5  
6 846 plutons, the effect of oxidation state of host rocks on trace element variations in  
7  
8  
9 847 magnetite from different porphyry deposits cannot be discussed. However, the relative  
10  
11  
12 848 oxygen fugacity conditions for different porphyry deposits can be reflected by  
13  
14  
15 849 magnetite chemistry. It is worth noting that hydrothermal magnetite from porphyry  
16  
17 850 Au-Cu deposits is depleted in V relative to those from porphyry Cu-Au, Cu-Mo, and  
18  
19  
20 851 Cu-Mo-Au deposits (Fig. 10C). The fact that gold-rich deposits are usually rich in  
21  
22  
23 852 magnetite suggests that high  $fO_2/fS_2$  ratio, conducive to deposition of larger amounts  
24  
25  
26 853 of magnetite under feldspar-stable conditions, also favor the precipitation of larger  
27  
28  
29 854 amounts of gold (Sillitoe, 1979; Sun et al., 2004). The relative depletion of V in  
30  
31  
32 855 porphyry Au-Cu hydrothermal magnetite is consistent with their formation under  
33  
34  
35 856 higher  $fO_2$  than hydrothermal magnetite from other subtypes of porphyry deposits  
36  
37  
38 857 because V partitions into magnetite at relatively low  $fO_2$  (Toplis and Corgne, 2002;  
39  
40  
41 858 Sievwright et al., 2017; Sossi et al., 2018).

42 859 In addition to host rock composition, fluid chemistry, and  $fO_2$  conditions,  
43  
44  
45 860 temperature may exert control on the chemical composition of magnetite from  
46  
47  
48 861 different types of porphyry deposits. Titanium and Al concentrations in magnetite are  
49  
50  
51 862 positively correlated to temperature in igneous system (Nielsen et al., 1994; Toplis  
52  
53  
54 863 and Carroll, 1995). Both igneous and hydrothermal magnetite from porphyry Cu-Au  
55  
56  
57 864 and Cu-Mo deposits have higher Ti and Al contents than other types of deposits,  
58  
59  
60 865 particularly Au-Cu deposits (Figs. 8C, 9F, and 10D). This indicates that Cu-dominated



1 866 porphyry deposits formed at a higher temperature than Au-dominated porphyry  
2  
3 867 deposits. This conclusion is consistent with the evolution of porphyry systems. In  
4  
5  
6 868 many porphyry Cu deposits, fluid cooling from ~550 to 350°C, assisted by fluid-rock  
7  
8  
9 869 interaction, is largely responsible for Cu precipitation in low sulfidation-state Cu-Fe  
10  
11 870 sulfide assemblages with some Au (Sillitoe, 2010). Upward decompression and  
12  
13  
14 871 expansion of the vapor phase causes a decrease in solubility of the vapor-transported  
15  
16  
17 872 metals (Williams-Jones and Heinrich, 2005), leading to precipitation of the Cu-Fe  
18  
19  
20 873 sulfides together with Au. The precipitation gold by decreasing temperature and  
21  
22  
23 874 pressure thereby potentially accounts for the typically shallow formation (Cox and  
24  
25 875 Singer, 1992; Sillitoe, 2000) of Au-rich porphyry Cu deposits (Williams-Jones and  
26  
27  
28 876 Heinrich, 2005).

29  
30  
31 877

32  
33  
34 878 *Relationship between magmatic affinity and magnetite chemistry*

35  
36 879 Porphyry deposits can be classified based on the geochemical composition of their  
37  
38  
39 880 associated porphyritic intrusions (Barr et al., 1976). Most of the studied porphyry  
40  
41  
42 881 deposits are associated with calc-alkaline and alkaline intrusions, whereas Bingham  
43  
44  
45 882 Canyon and Oyu Tolgoi Cu-Mo-Au deposits, and Bajo de la Alumbrera Cu-Au  
46  
47  
48 883 deposits are hosted by intrusions with high-K calc-alkaline compositions (Table 1). It  
49  
50  
51 884 has been suggested that Au-rich porphyry deposits have an affinity with high-K  
52  
53 885 calc-alkaline rocks (Müller and Groves, 1993, 2000; Sillitoe, 1997, 2000). In this  
54  
55  
56 886 section, we discuss the magmatic affinity with the chemical composition of igneous  
57  
58  
59 887 and hydrothermal magnetite.

1 888 PLS-DA of EPMA data for both igneous and hydrothermal magnetite shows no  
2  
3 889 distinction based on magmatic affinities of host porphyry (Figs. 11 and 12). In spite of  
4  
5  
6 890 overlapping in the  $t_1$ - $t_2$  plots (Figs. 11B and 12B), positive contributions of Zn, V, and  
7  
8  
9 891 Ca discriminate igneous and hydrothermal magnetite associated with calc-alkaline  
10  
11 892 intrusions, whereas positive contributions of Ti and Al discriminate those associated  
12  
13 893 with high-K calc-alkaline intrusions (Figs. 11D-E and 12D-E). PLS-DA of  
14  
15 894 LA-ICP-MS data of hydrothermal magnetite defines fields for porphyries with  
16  
17 895 different magmatic affinity (Figs. 13A-B). Hydrothermal magnetite associated with  
18  
19 896 alkaline intrusions is discriminated by positive contributions of Mg, Mn, Co, Zr, Nb,  
20  
21 897 Mo, Sn, Hf, and Ta, whereas that associated with calc-alkaline intrusions is  
22  
23 898 discriminated by positive contributions of V, Ni, Cu, Ga, Ge, Sb, and W (Figs.  
24  
25 899 13C-D). Hydrothermal magnetite associated with high-K calc-alkaline intrusions can  
26  
27 900 be separated from that associated with alkaline and calc-alkaline intrusions by  
28  
29 901 positive contributions of Al, Sc, Ti, and Ta (Fig. 13E). This indicates that  
30  
31 902 hydrothermal magnetite chemistry is partly controlled by the magmatic affinity of  
32  
33 903 intrusions.  
34  
35

36  
37 904 An alkaline magma is rich in Na and K relative to subalkaline magmas (Le Bas et  
38  
39 905 al., 1986), depleted in Si and/or Al with respect to alkalis, and rich in volatile  
40  
41 906 components (Fitton, 1987). Development of extensive zones of metasomatized  
42  
43 907 country rock (fenite) around alkaline plutons, the abundance of chlorine and fluorine  
44  
45 908 in some alkaline igneous rocks, and the common explosive eruption of alkaline  
46  
47 909 magma all point to high concentrations of volatiles (Fitton, 1987; Harris and Sheppard,  
48  
49  
50  
51  
52  
53  
54  
55  
56  
57  
58  
59  
60  
61  
62  
63  
64  
65

1 910 1987). It is worth noting that hydrothermal magnetite associated with alkaline  
2  
3 911 intrusions has the same signature elements with that from the Au-Cu deposits that are  
4  
5  
6 912 mainly hosted by alkaline intrusions. Therefore, the same factors controlling the  
7  
8  
9 913 chemical composition of hydrothermal magnetite from the Au-Cu deposits, such as  
10  
11  
12 914 the high concentrations of Cl and F in magma/fluids, can be applied to hydrothermal  
13  
14  
15 915 magnetite associated with alkaline intrusions. The typically higher Ca content in  
16  
17  
18 916 igneous and hydrothermal magnetite associated with calc-alkaline intrusions may be  
19  
20  
21 917 related to the high concentration of Ca in this magma series (Wilson, 1996). The  
22  
23  
24 918 relative depletion of HFSE in hydrothermal magnetite associated with calc-alkaline  
25  
26  
27 919 intrusions is also consistent with the depletion of these elements in calc-alkaline  
28  
29  
30 920 magma (Hooper, 1994).

31 921 High-K, I-type granitoid magmas are derived from partial melting of hydrous,  
32  
33  
34 922 calc-alkaline to high-K calc-alkaline, mafic to intermediate metamorphic rocks in the  
35  
36  
37 923 crust (Roberts and Clemens, 1993). The relative enrichment of incompatible elements,  
38  
39  
40 924 Sc and Ta, in igneous and hydrothermal magnetite associated with high-K  
41  
42  
43 925 calc-alkaline intrusions may reflect the composition of this magma type. The coupled  
44  
45  
46 926 behavior of Al and Ti in igneous and hydrothermal magnetite (Figs. 11A, 12A and  
47  
48  
49 927 13A) is similar to the observation in other porphyry deposits (Canil et al., 2016). The  
50  
51  
52 928 partition of both Ti and Al in the magnetite shows a positive temperature dependence  
53  
54  
55 929 (Nielsen et al., 1994; Toplis and Carroll, 1995). The relatively high Al and Ti in  
56  
57  
58 930 igneous and hydrothermal magnetite associated with high-K calc-alkaline intrusions  
59  
60  
61 931 likely reflect higher temperatures for magnetite formation or the relative enrichment

1 932 of these elements in high-K calc-alkaline melts and their exsolved fluids.  
2  
3 933  
4  
5  
6 934 *Comparison of porphyry Cu magnetite composition with IOCG, IOA and skarn*  
7  
8  
9 935 *deposits*  
10  
11 936 Porphyry Cu, IOCG, IOA and skarn deposits belong to the family of  
12  
13 937 magmatic-hydrothermal deposits (Sillitoe, 2003, 2010; Meinert et al., 2005; Williams  
14  
15 938 et al., 2005; Pollard, 2006; Richards and Mumin, 2013; Simon et al., 2018), although  
16  
17 939 some IOCG deposits are also considered to be related to basinal brines (Barton and  
18  
19  
20  
21  
22 940 Johnson, 2000). These deposits have similar ore mineral assemblages of magnetite,  
23  
24  
25 941 hematite, chalcopyrite and pyrite but with different proportions. Some have proposed  
26  
27  
28 942 that IOCG deposits represent a vertical continuum ranging from deep, magnetite  
29  
30  
31 943 dominated Cu–Au mineralization, to hematite-bearing Cu ore at shallow levels, all  
32  
33  
34 944 associated with geochemically primitive diorite intrusions (Sillitoe, 2003; Tornos et  
35  
36  
37 945 al., 2010). Others consider that contrasting tectonic settings and sulfur contents of  
38  
39 946 magmas control the formation of porphyry Cu ± Mo ± Au and intrusion-related IOCG  
40  
41  
42 947 deposits (Richards and Mumin, 2013; Richards et al., 2017). The close relationship  
43  
44  
45 948 between porphyry Cu and skarn systems is well recognized (Einaudi et al., 1981;  
46  
47  
48 949 Einaudi, 1982) and the carbonate wall rocks around the intrusion-centered porphyry  
49  
50  
51 950 system can host proximal Cu-Au skarns and less common distal Zn-Pb and/or Au  
52  
53  
54 951 skarns (Sillitoe, 2010). In carbonates and carbonate alteration close to intrusions in  
55  
56 952 IOCG systems, skarns may develop with Fe-Cu-Au sulfide mineralization (Corriveau  
57  
58  
59 953 et al., 2010, 2016). Dupuis and Beaudoin (2011) proposed plots of Ca+Al+Mn versus

1 954 Ti+V and Ni/(Cr+Mn) versus Ti+V, based on EPMA data, to distinguish magnetite in  
2  
3 955 porphyry deposits from other magmatic-hydrothermal deposits. Nadoll et al. (2014,  
4  
5  
6 956 2015), however, considered that the boundary between porphyry Cu and skarn  
7  
8  
9 957 deposits in Al+Mn versus Ti+V plot is transitional. Canil et al. (2016) showed that the  
10  
11  
12 958 PCA method is efficient to distinguish highest-temperature igneous magnetite,  
13  
14 959 intermediate-temperature hydrothermal porphyry magnetite, and low-temperature  
15  
16  
17 960 skarn magnetite due to different Ti, Al and V contents. Here, we compare the trace  
18  
19  
20 961 element composition of hydrothermal magnetite from porphyry Cu, IOCG, IOA, and  
21  
22  
23 962 skarn deposits using PLS-DA of a large EPMA ( $n = 1675$ ) and LA-ICP-MS ( $n = 1335$ )  
24  
25  
26 963 dataset, to identify the most discriminant elements for each deposit type. This will be  
27  
28  
29 964 useful to identify magnetite with unknown origins.

30  
31 965 PLS-DA of EPMA data (Si, Ca, Al, Mn, Mg, Ti, and V) shows that magnetite from  
32  
33  
34 966 porphyry Cu, IOCG, IOA, and skarn deposits cannot be discriminated from each other  
35  
36  
37 967 (Figs. 18A-B). However, magnetite from different types of deposits shows  
38  
39  
40 968 characteristic elemental composition. Magnetite from porphyry Cu deposits is  
41  
42  
43 969 characterized by positive contributions of Ti, Al, and V (Fig. 18E), whereas that from  
44  
45  
46 970 IOCG deposits is discriminated by positive contributions of Al and Ti (Fig. 18F).  
47  
48  
49 971 Weakly positive contributions of Mg, Ca, and V and negative contribution of Al  
50  
51  
52 972 characterize magnetite from IOA deposits (Fig. 18G), whereas positive contributions  
53  
54  
55 973 of Ca and Mg discriminate magnetite from skarn deposits (Fig. 18H). EPMA data VIP  
56  
57  
58 974 plot shows that Ti is the most important discriminant element for these four types of  
59  
60  
61 975 deposits (Fig. 18M). Calcium is useful discriminating all deposit types except IOA

1 976 deposits, whereas Mg is useful discriminating between porphyry Cu and skarn  
2  
3 977 deposits (Fig. 18M). Silicon is important discriminant element for IOCG deposits,  
4  
5  
6 978 whereas Al is useful in discrimination between IOCG and IOA magnetite (Fig. 18M).  
7  
8  
9 979 PLS-DA of LA-ICP-MS data, using Al, Mn, Mg, Ti, V, Ga, Co, Zn, Ni, and Sn, yields  
10  
11 980 a better discrimination than that of EPMA data. Magnetite from IOCG deposits can be  
12  
13 981 separated from skarn deposits by  $t_1$ , but magnetite from IOA and porphyry deposits  
14  
15  
16  
17 982 overlaps that from IOCG deposits (Figs. 18C-D). Score contributions indicate that  
18  
19  
20 983 magnetite from porphyry deposits has relatively high Ti and Zn (Fig. 18I), whereas  
21  
22 984 that from IOCG deposits has relatively high V and Ni (Fig. 18J). Magnetite from IOA  
23  
24  
25 985 deposits is characterized by higher V, Ti, and Mg (Fig. 18K), whereas magnetite from  
26  
27  
28 986 skarn deposits is characterized by higher Mn, Mg, and Zn (Fig. 18L). LA-ICP-MS  
29  
30  
31 987 data VIP plot shows that Mg, Zn, and V are most important discriminant elements for  
32  
33  
34 988 the four types of deposits, whereas Mn and Ni are important in discriminating  
35  
36  
37 989 between magnetite from IOCG deposits and skarn deposits (Fig. 18N). Tin, Al, and Ti  
38  
39  
40 990 are useful for discriminating between magnetite from IOA and porphyry Cu deposits  
41  
42  
43 991 (Fig. 18N). In summary, Ti, V, Zn, and Al, in the order of decreasing importance, are  
44  
45  
46 992 higher in magnetite from porphyry Cu deposits, V, Ni, Ti, and Al are for IOCG  
47  
48  
49 993 deposits, V, Ti, and Mg are for IOA deposits, and Mg, Mn, Ca, and Zn are for skarn  
50  
51  
52 994 deposits. This conclusion is consistent with the study of Nadoll et al. (2015), in which  
53  
54  
55 995 the key elements accounting for compositional variations are Mg and Mn for  
56  
57  
58 996 hydrothermal magnetite from skarn, and Mg, Ti, V, Mn, Co, and Zn for hydrothermal  
59  
60  
61 997 porphyry magnetite.

1 998 The decreased Ti+V contents in magnetite from porphyry Cu, IOA, IOCG, to skarn  
2  
3 999 deposits is consistent with the studies of Dupuis and Beaudoin (2011) and Canil et al.  
4  
5  
6 1000 (2016), which likely reflect decreasing temperature and increasing oxygen fugacity  
7  
8  
9 1001 (Nadoll et al., 2014). The porphyry Cu system cools from >700°C to <250°C with the  
10  
11 1002 main Cu precipitation at 550-350°C (Sillitoe, 2010). IOA deposits commonly formed  
12  
13 1003 by high-temperature (~800-600°C) magmatic or magmatic–hydrothermal processes as  
14  
15  
16 1004 indicated by Fe-O stable isotope pairs of magnetite and actinolite (Bilenker et al.,  
17  
18  
19 1005 2016; Corriveau et al., 2016), whereas IOCG deposits have temperatures  
20  
21  
22 1006 from >600°C to ~200°C with Cu-Au precipitation between 500°C to 200°C (Williams  
23  
24  
25 1007 et al., 2005; Corriveau et al., 2016). Skarn deposits can evolve from high-temperature  
26  
27  
28 1008 ( $\geq 500^\circ\text{C}$ ) high-salinity fluids of magmatic origin in the prograde alteration stage to  
29  
30  
31 1009 lower temperature ( $\leq 400^\circ\text{C}$ ) fluids during retrograde magnetite-sulfide stage with  
32  
33  
34 1010 influx of cooler, lower salinity fluids of magmatic origin (Meinert et al., 2005). Most  
35  
36 1011 porphyry Cu deposits formed at the  $f\text{O}_2$  of 3 log units above the quartz–  
37  
38  
39 1012 magnetite/fayalite buffer ( $\Delta\text{FMQ} +3$ ) (Richards, 2014), whereas IOCG and skarn  
40  
41  
42 1013 deposits probably formed at  $\Delta\text{FMQ} +5$ , considering the amounts of hematite in the  
43  
44  
45 1014 mineral assemblage (Meinert et al., 2005; Williams et al., 2005). Experimental studies  
46  
47  
48 1015 have shown that IOA deposits can form from immiscible hydrous Fe–Ca–P melt  
49  
50  
51 1016 under more reduced conditions at  $\Delta\text{FMQ}$  between +0.5 and +3.3 (Hou et al., 2018).  
52  
53 1017 The relative depletion of Al in IOA magnetite is due to its low magnetite-silicate melt  
54  
55  
56 1018 partition coefficient ( $D_{\text{Al}} = 0.2$ ; Dare et al., 2012) and relatively immobility of Al in  
57  
58  
59 1019 fluids (Middelburg et al., 1988). With the evolution of melt or fluids, Al will be  
60  
61  
62  
63  
64  
65

1 1020 enriched in later magnetite. Considering that the earlier, higher temperature formation  
2  
3 1021 of IOA deposits than IOCG and skarn deposits in a magmatic-hydrothermal system  
4  
5  
6 1022 (Corriveau et al., 2006), magnetite from IOA deposits is thus relatively depleted in Al.  
7  
8  
9 1023 The higher Ni in IOCG magnetite, compared to porphyry and skarn magnetite, is  
10  
11 1024 probably due to the more mafic magma for IOCG deposits compared to granodioritic  
12  
13 1025 magmas associated with porphyry and skarn deposits (Richards et al., 2017). The  
14  
15 1026 more abundant sulfides in porphyry deposits mineral assemblages, compared to IOCG  
16  
17 1027 deposits, will likely result in low-Ni porphyry system because of Ni partitioning into  
18  
19 1028 sulfides (Dare et al., 2012; Huang et al., 2014). The higher Ca, Mn, Mg, and Zn in  
20  
21 1029 skarn magnetite is consistent with previous studies of magnetite from skarn deposits  
22  
23 1030 (Hu et al., 2014; Nadoll et al., 2015; Huang et al., 2016, 2018b). Experimental studies  
24  
25 1031 suggest that even minor to trace concentrations of base metals, such as Mn and Zn, in  
26  
27 1032 magnetite indicate strong enrichment of Mn and Zn, relative to Fe, in chloride-rich  
28  
29 1033 hydrothermal fluids, particularly in skarn system (Ilton and Eugster, 1989). Therefore,  
30  
31 1034 the elevated Ca, Mn, Mg, and Zn in skarn magnetite likely reflect high concentrations  
32  
33 1035 of these elements in hydrothermal fluids, possibly via fluid-rock (carbonate)  
34  
35 1036 interaction (Einaudi et al., 1981; Meinert et al., 2005).  
36  
37  
38  
39  
40  
41  
42  
43  
44  
45  
46  
47  
48  
49

## 50 **Conclusions**

51  
52  
53 1039 Trace element compositions of igneous and hydrothermal magnetite from porphyry  
54  
55 1040 deposits are used to discuss the main factors controlling the magnetite chemistry.  
56  
57  
58 1041 PLS-DA of magnetite composition is used to discriminate between igneous and  
59  
60  
61  
62  
63  
64  
65



1 1042 hydrothermal magnetite, between porphyry deposit subtypes, and between magmatic  
2  
3 1043 intrusion affinity. Igneous magnetite can be discriminated from hydrothermal  
4  
5  
6 1044 magnetite by higher P, Ti, V, Mn, Zr, Nb, Hf, and Ta but lower Mg, Si, Co, Ni, Ge, Sb,  
7  
8  
9 1045 W, and Pb. Compositional variations between igneous and hydrothermal magnetite in  
10  
11 1046 porphyry system are controlled by temperature, and oxygen fugacity, co-precipitated  
12  
13 1047 sulfides, and element solubility/mobility that affects the partition coefficients.  
14  
15 1048 Hydrothermal magnetite from porphyry W-Mo and Au-Cu deposits can be  
16  
17 1049 discriminated from that from Cu-Mo, Cu-Au, and Cu-Mo-Au deposits due to different  
18  
19 1050 compositional characteristics. Compositional variation in magnetite from different  
20  
21 1051 deposit subtypes results from variations in host rock composition, chlorine in fluids,  
22  
23 1052 temperature, and oxygen fugacity. Magmatic affinity of porphyritic intrusions may  
24  
25 1053 have some control on the chemical composition of igneous and hydrothermal  
26  
27 1054 magnetite mainly by influencing the magma composition and formation temperatures.  
28  
29 1055 However, the reason for the relationship between magmatic affinity and magnetite  
30  
31 1056 composition needs further study. PLS-DA of compiled porphyry Cu, IOCG and skarn  
32  
33 1057 magnetite composition identifies discriminant elements Ti, V, Zn, and Al for porphyry  
34  
35 1058 Cu magnetite, V, Ni, Ti, and Al are for IOCG magnetite, V, Ti, and Mg are for IOA  
36  
37 1059 magnetite, and Mn, Mg, Ca, and Zn for skarn magnetite. These compositional  
38  
39 1060 differences are mainly due to higher temperature and lower oxygen fugacity for IOA  
40  
41 1061 and porphyry deposits, more mafic magma composition and less sulfide competition  
42  
43 1062 for IOCG deposits, and more intensive fluid-rock (carbonate) interaction in skarn  
44  
45 1063 deposits.  
46  
47  
48  
49  
50  
51  
52  
53  
54  
55  
56  
57  
58  
59  
60  
61  
62  
63  
64  
65

1 1064

3 1065

### Acknowledgments

6 1066 This project was funded by China Scholarship Council (CSC, 201604910462), the  
7  
8  
9 1067 Natural Science and Engineering Research Council (NSERC) of Canada through a  
10  
11 1068 Collaborative Research and Development Grant with Vale, Teck, Areva (now Orano)  
12  
13  
14 1069 and the Geological Survey of Canada and the NSERC-Agnico Eagle Industrial  
15  
16  
17 1070 Research Chair in Mineral Exploration. We thank Marc Choquette (Université Laval)  
18  
19  
20 1071 for his assistance with EPMA analyses, André Ferland, Émilie Bédard, and Marjorie  
21  
22  
23 1072 Lapointe (Université Laval) for their assistance with SEM analyses, and Dany Savard  
24  
25  
26 1073 (UQAC) for his assistance with LA-ICP-MS analyses. Special thanks are also  
27  
28 1074 extended to Brian Rusk (Western Washington University), Christoph A. Heinrich  
29  
30  
31 1075 (ETH-Zurich), Jeremy P. Richards (University of Alberta), Meghan Jackson, Paul  
32  
33  
34 1076 Jago, and Janina Micko (University of British Columbia), Aldo Bendezu and Kalin  
35  
36  
37 1077 Kouzmanov (Université de Genève), Doug Kirwin (formerly Ivanhoe Mines), and  
38  
39 1078 Tim Fletcher (Barrick Gold UK Limited), who provided representative samples. We  
40  
41  
42 1079 thank Jaayke L. Knipping for sharing the original table for IOA magnetite data of Los  
43  
44  
45 1080 Colorados. We also acknowledge constructive comments from Patrick Nadoll and an  
46  
47  
48 1081 anonymous reviewer, and editorial handling by Adam Simon and Larry Meinert.

50 1082

## REFERENCES

- 1083
- 1084 Aitchison, J., 1986, The statistical analysis of compositional data: London, UK,  
1085 Chapman and Hall Ltd.
- 1086 Barr, D.A., Fox, P.E., Northcote, K.E., and Preto, V.A., 1976, The alkaline suite  
1087 porphyry deposits: a summary: Canadian Institute of Mining and Metallurgy  
1088 Special Volume 15, p. 359-367.
- 1089 Barton, M.D., and Johnson, D.A., 2000, Alternative brine sources for Fe-oxide  
1090 (-Cu-Au) systems: Implications for hydrothermal alteration and metals, *in* Porter, T.  
1091 M., ed., Hydrothermal iron oxide copper-gold and related deposits: a global  
1092 perspective, 1: Adelaide, Australian Mineral Foundation, p. 43-60.
- 1093 Beane, R.E., 1981, Porphyry copper deposits, Part II. Hydrothermal alteration and  
1094 mineralization: *Economic Geology*, v. 75, p. 235-269.
- 1095 Bernstein, L.R., 1985, Germanium geochemistry and mineralogy: *Geochimica et*  
1096 *Cosmochimica Acta*, v. 49, p. 2409-2422.
- 1097 Bilenker, L.D., Simon, A.C., Reich, M., Lundstrom, C.C., Gajos, N., Bindeman, I.,  
1098 Barra, F., and Munizaga, R., 2016, Fe–O stable isotope pairs elucidate a  
1099 high-temperature origin of Chilean iron oxide-apatite deposits: *Geochimica et*  
1100 *Cosmochimica Acta*, v. 177, p. 94-104.
- 1101 Borcos, M., Vlad, S., Udubasa, G., and Gabudeanu, B., 1998, Qualitative and  
1102 quantitative metallogenetic analysis of the ore genetic units in Romania: *Romanian*  
1103 *Journal of Mineral Deposits*, v. 78, p. 1-83.
- 1104 Boutroy, E., Dare, S.A.S., Beaudoin, G., Barnes, S.-J., and Lightfoot, P.C., 2014,

1 1105 Magnetite composition in Ni-Cu-PGE deposits worldwide and its application to  
2  
3 1106 mineral exploration: *Journal of Geochemical Exploration*, v. 145, p. 64-81.  
4  
5  
6 1107 Brereton, R.G., and Lloyd, G.R., 2014, Partial least squares discriminant analysis:  
7  
8 1108 taking the magic away: *Journal of Chemometrics*, v. 28, p. 213-225.  
9  
10  
11 1109 Buddington, A., and Lindsley, D., 1964, Iron-titanium oxide minerals and synthetic  
12  
13 1110 equivalents: *Journal of Petrology*, v. 5, p. 310-357.  
14  
15  
16  
17 1111 Canil, D., Grondahl, C., Lacourse, T., and Pisiak, L.K., 2016, Trace elements in  
18  
19 1112 magnetite from porphyry Cu–Mo–Au deposits in British Columbia, Canada: *Ore  
20  
21  
22 1113 Geology Reviews*, v. 72, p. 1116-1128.  
23  
24  
25 1114 Carew, M.J., 2004, Controls on Cu-Au mineralisation and Fe oxide metasomatism in  
26  
27 1115 the Eastern Fold Belt, NW Queensland, Australia: Unpub. Ph.D. thesis thesis,  
28  
29 1116 James Cook University, 213-277 p.  
30  
31  
32  
33 1117 Catchpole, H., Kouzmanov, K., Putlitz, B., Seo, J.H., and Fontboté, L., 2015, Zoned  
34  
35 1118 base metal mineralization in a porphyry system: Origin and evolution of  
36  
37 1119 mineralizing fluids in the Morococha district, Peru: *Economic Geology*, v. 110, p.  
38  
39 1120 39-71.  
40  
41  
42  
43  
44 1121 Chen, W.T., Zhou, M.-F., Gao, J.-F., and Hu, R.Z., 2015a, Geochemistry of magnetite  
45  
46 1122 from Proterozoic Fe-Cu deposits in the Kangdian metallogenic province, SW China:  
47  
48 1123 *Mineralium Deposita*, v. 50, p. 795-809.  
49  
50  
51  
52  
53 1124 Chen, W.T., Zhou, M.-F., Li, X., Gao, J.-F., and Hou, K., 2015b, In-situ LA-ICP-MS  
54  
55 1125 trace elemental analyses of magnetite: Cu-(Au, Fe) deposits in the Khetri copper  
56  
57 1126 belt in Rajasthan province, NW India: *Ore Geology Reviews*, v. 65, p. 929-939.  
58  
59  
60  
61  
62  
63  
64  
65

1 1127 Chou, I.-M., and Eugster, H.P., 1977, Solubility of magnetite in supercritical chloride  
2  
3 1128 solutions: American Journal of Science, v. 277, p. 1296-1314.  
4  
5  
6 1129 Ciobanu, C.L., and Cook, N.J., 2004, Skarn textures and a case study: the Ocna de  
7  
8 1130 Fier-Dognecea orefield, Banat, Romania: Ore Geology Reviews, v. 24, p. 315-370.  
9  
10  
11 1131 Cooke, D.R., Hollings, P., and Walshe, J.L., 2005, Giant porphyry deposits:  
12  
13 1132 characteristics, distribution, and tectonic controls: Economic geology, v. 100, p.  
14  
15 1133 801-818.  
16  
17  
18  
19  
20 1134 Corriveau, L., Montreuil, J.-F., and Potter, E., 2016, Alteration facies linkages among  
21  
22 1135 iron oxide copper-gold, iron oxide-apatite, and affiliated deposits in the Great Bear  
23  
24 1136 magmatic zone, Northwest Territories, Canada: Economic Geology, v. 111, p.  
25  
26 1137 2045-2072.  
27  
28  
29  
30  
31 1138 Corriveau, L., Williams, P.J., and Mumin, A.H., 2010, Alteration vectors to IOCG  
32  
33 1139 mineralization – From uncharted terranes to deposits, *in* Corriveau, L., and Mumin,  
34  
35 1140 H., eds., Exploring for iron oxide copper-gold deposits: Canada and global  
36  
37 1141 analogues, Geological Association of Canada, Short Course Notes 20, p. 89-110.  
38  
39  
40  
41  
42 1142 Cox, D.P., and Singer, D.A., 1988, Distribution of gold in porphyry copper deposits,  
43  
44 1143 US Geological Survey Open-File Report 88-46, p. C1-C14.  
45  
46  
47  
48 1144 Crane, D., Kavalieris, I., Hedenquist, J.W., Harris, M., and Camus, F., 2012, Geologic  
49  
50 1145 overview of the Oyu Tolgoi porphyry Cu-Au-Mo deposits, Mongolia: Economic  
51  
52 1146 Geology Special Publication, v. 16, p. 187-213.  
53  
54  
55  
56 1147 Dare, S.A.S., Barnes, S.-J., and Beaudoin, G., 2012, Variation in trace element content  
57  
58 1148 of magnetite crystallized from a fractionating sulfide liquid, Sudbury, Canada:  
59  
60  
61  
62  
63  
64  
65

1 1149 Implications for provenance discrimination: *Geochimica et Cosmochimica Acta*, v.  
2  
3 1150 88, p. 27-50.  
4  
5  
6 1151 Dare, S.A.S., Barnes, S.-J., Beaudoin, G., Méric, J., Boutroy, E., and Potvin-Doucet,  
7  
8  
9 1152 C., 2014, Trace elements in magnetite as petrogenetic indicators: *Mineralium*  
10  
11 1153 *Deposita*, v. 49, p. 785-796.  
12  
13  
14 1154 De Iorio, M., Ebbels, T.M.D., and Stephens, D.A., 2008, Statistical techniques in  
15  
16 1155 metabolic profiling, *Handbook of Statistical Genetics*, John Wiley & Sons, Ltd, p.  
17  
18 1156 347-373.  
19  
20  
21  
22 1157 Deditius, A.P., Reich, M., Simon, A.C., Suvorova, A., Knipping, J., Roberts, M.P.,  
23  
24  
25 1158 Rubanov, S., Dodd, A., and Saunders, M., 2018, Nanogeochemistry of  
26  
27 1159 hydrothermal magnetite: *Contributions to Mineralogy and Petrology*, v. 173, p. 46.  
28  
29  
30  
31 1160 Dilles, J., Martin, M.W., and Stein, H.J., 2003, Re-Os and U-Pb ages for the Butte  
32  
33 1161 copper district, Montana: A short- or long-lived hydrothermal system: GSA 2003  
34  
35 1162 Seattle Annual Meeting, Seattle, 2003.  
36  
37  
38  
39 1163 Dirom, G.E., Dittrick, M.P., McArthur, D.R., Ogryzlo, P.L., Pardoe, A.J., Stothart,  
40  
41  
42 1164 P.G., and Schroeter, T.G., 1995, Bell and Granisle porphyry copper-gold mines,  
43  
44 1165 Babine region, west-central British Columbia, *in* Schroeter, T. G., ed., *Porphyry*  
45  
46 1166 *deposits of the northwestern Cordillera of North America*, Canadian Institute of  
47  
48 1167 *Mining, Metallurgy and Petroleum*, Special Vol. 46, p. 256-289.  
49  
50  
51  
52  
53 1168 Duan, S., Zhang, Z., Jiang, Z., Zhao, J., Zhang, Y., Li, F., and Tian, J., 2014, *Geology,*  
54  
55 1169 *geochemistry, and geochronology of the Dundee iron–zinc ore deposit in western*  
56  
57 1170 *Tianshan, China: Ore Geology Reviews*, v. 57, p. 441-461.  
58  
59  
60  
61  
62  
63  
64  
65

- 1 1171 Dupuis, C., and Beaudoin, G., 2007, Signature géochimique des oxydes de fer et  
2  
3 1172 application à l'exploration minière – 2e volet.: Annual report of project DIVEX  
4  
5  
6 1173 SC-22, p. 1-24.  
7  
8  
9 1174 Dupuis, C., and Beaudoin, G., 2011, Discriminant diagrams for iron oxide trace  
10  
11 1175 element fingerprinting of mineral deposit types: Mineralium Deposita, v. 46, p.  
12  
13 1176 1-17.  
14  
15  
16  
17 1177 Egozcue, J.J., Pawlowsky-Glahn, V., Mateu-Figueras, G., and Barcelo-Vidal, C., 2003,  
18  
19 1178 Isometric logratio transformations for compositional data analysis: Mathematical  
20  
21 1179 Geology, v. 35, p. 279-300.  
22  
23  
24  
25 1180 Einaudi, M.T., 1982, Description of skarns associated with porphyry copper plutons, *in*  
26  
27 1181 Titley, S. R., ed., Advances in geology of the porphyry copper deposits, southwestern  
28  
29 1182 North America: Tucson, University of Arizona Press, p. 139-183.  
30  
31  
32  
33 1183 Einaudi, M.T., Meinert, L.D., and Newberry, R.J., 1981, Skarn deposits: Economic  
34  
35 1184 Geology, v. 75, p. 317-391.  
36  
37  
38  
39 1185 Eliopoulos, D.G., Economou-Eliopoulos, M., and Zelyaskova-Panayiotova, M., 2014,  
40  
41 1186 Critical factors controlling Pd and Pt potential in porphyry Cu–Au deposits:  
42  
43 1187 evidence from the Balkan Peninsula: Geosciences, v. 4, p. 31-49.  
44  
45  
46  
47 1188 Eriksson, L., Byrne, T., Johansson, E., Trygg, J., and Vikström, C., 2013, Multi- and  
48  
49 1189 megavariable data analysis: Basic principles and applications: Sweden, MKS  
50  
51 1190 Umetrics AB, 1-521 p.  
52  
53  
54  
55 1191 Fitton, J.G., 1987, Alkaline igneous rocks, *in* Upton, B. G. J., ed., Geological Society  
56  
57 1192 Special Publications 30: London, Blackwell Scientific Publications.  
58  
59  
60  
61  
62  
63  
64  
65

1 1193 Floyd, P.A., and Winchester, J.A., 1978, Identification and discrimination of altered  
2  
3 1194 and metamorphosed volcanic rocks using immobile elements: *Chemical Geology*, v.  
4  
5  
6 1195 21, p. 291-306.  
7  
8  
9 1196 Fraser, T.M., 1994, Geology, alteration and origin of hydrothermal breccias at the  
10  
11 1197 Mount Polley alkalic porphyry copper-gold deposit, south-central British Columbia:  
12  
13  
14 1198 Unpub. Master thesis thesis, The University of British Columbia, 275 p.  
15  
16  
17 1199 Frei, R., 1995, Evolution of mineralizing fluid in the porphyry copper system of the  
18  
19  
20 1200 Skouries Deposit, Northeast Chalkidiki (Greece); evidence from combined Pb-Sr  
21  
22 1201 and stable isotope data: *Economic Geology*, v. 90, p. 746-762.  
23  
24  
25 1202 Frost, B.R., and Lindsley, D.H., 1992, Equilibria among Fe-Ti oxides, pyroxenes,  
26  
27  
28 1203 olivine, and quartz: Part II. Application: *American Mineralogist*, v. 77, p.  
29  
30 1204 1004-1004.  
31  
32  
33 1205 Ghiorso, M.S., and Sack, O., 1991, Fe-Ti oxide geothermometry: thermodynamic  
34  
35 1206 formulation and the estimation of intensive variables in silicic magmas:  
36  
37  
38 1207 *Contributions to Mineralogy and Petrology*, v. 108, p. 485-510.  
39  
40  
41  
42 1208 Gosselin, P., Beaudoin, G., and Jébrak, M., 2006, Signature géochimique des oxydes  
43  
44 1209 de fer et application à l'exploration minière: Annual report of projet DIVEX SC-16,  
45  
46  
47 1210 p. 1-58.  
48  
49  
50 1211 Harris, A.C., Dunlap, W.J., Reiners, P.W., Allen, C.M., Cooke, D.R., White, N.C.,  
51  
52  
53 1212 Campbell, I.H., and Golding, S.D., 2008, Multimillion year thermal history of a  
54  
55 1213 porphyry copper deposit: application of U-Pb,  $^{40}\text{Ar}/^{39}\text{Ar}$  and (U-Th)/He  
56  
57  
58 1214 chronometers, Bajo de la Alumbrera copper-gold deposit, Argentina: *Mineralium*  
59  
60  
61  
62  
63  
64  
65



1 1215 Deposita, v. 43, p. 295-314.

2

3 1216 Harris, C., and Sheppard, S.M.F., 1987, Magma and fluid evolution in the lavas and

4

5

6 1217 associated granite xenoliths of Ascension Island: Geological Society Special

7

8

9 1218 Publications, v. 30, p. 269-272.

10

11 1219 Heidarian, H., Lentz, D., Alirezaei, S., Peighambari, S., and Hall, D., 2016, Using the

12

13

14 1220 chemical analysis of magnetite to constrain various stages in the formation and

15

16

17 1221 genesis of the Kiruna-type chadormalu magnetite-apatite deposit, Bafq district,

18

19

20 1222 Central Iran: Mineralogy and Petrology, v. 110, p. 927-942.

21

22 1223 Helsel, D.R., 2005, Nondetects and data analysis. Statistics for censored

23

24

25 1224 environmental data: New York, Wiley-Interscience.

26

27

28 1225 Hemley, J.J., and Hunt, J.P., 1992, Hydrothermal ore-forming processes in the light of

29

30

31 1226 studies in rock-buffered systems: II. Some general geologic applications: Economic

32

33

34 1227 Geology, v. 87, p. 23-43.

35

36 1228 Henley, R.W., 1973, Solubility of gold in hydrothermal chloride solutions: Chemical

37

38

39 1229 Geology, v. 11, p. 73-87.

40

41

42 1230 Holbek, P., and Noyes, R., 2013, Copper mountain: an alkalic porphyry copper–gold–

43

44

45 1231 silver deposit in the southern Quesnel terrane, British Columbia: Society of

46

47

48 1232 Economic Geologists Guidebook, v. 44, p. 129-143.

49

50 1233 Hooper, P., 1994, Sources of continental flood basalts: The lithospheric component:

51

52

53 1234 Volcanism, p. 29-53.

54

55 1235 Hou, T., Charlier, B., Holtz, F., Veksler, I., Zhang, Z., Thomas, R., and Namur, O.,

56

57

58 1236 2018, Immiscible hydrous Fe–Ca–P melt and the origin of iron oxide-apatite ore

59

60

61

62

63

64

65

1 1237 deposits: Nature Communications, v. 9, p. 1-8.  
2  
3 1238 Hron, K., Templ, M., and Filzmoser, P., 2010, Imputation of missing values for  
4  
5  
6 1239 compositional data using classical and robust methods: Computational Statistics &  
7  
8  
9 1240 Data Analysis, v. 54, p. 3095-3107.  
10  
11 1241 Hu, H., Lentz, D., Li, J.-W., McCarron, T., Zhao, X.-F., and Hall, D., 2015,  
12  
13  
14 1242 Reequilibration processes in magnetite from iron skarn deposits: Economic  
15  
16  
17 1243 Geology, v. 110, p. 1-8.  
18  
19  
20 1244 Hu, H., Li, J.-W., Lentz, D., Ren, Z., Zhao, X.-F., Deng, X.-D., and Hall, D., 2014,  
21  
22  
23 1245 Dissolution–reprecipitation process of magnetite from the Chengchao iron deposit:  
24  
25  
26 1246 Insights into ore genesis and implication for *in-situ* chemical analysis of magnetite:  
27  
28  
29 1247 Ore Geology Reviews, v. 57, p. 393-405.  
30  
31 1248 Hu, X., Chen, H., Zhao, L., Han, J., and Xia, X., 2017, Magnetite geochemistry of the  
32  
33  
34 1249 Longqiao and Tieshan Fe–(Cu) deposits in the Middle-Lower Yangtze River Belt:  
35  
36  
37 1250 Implications for deposit type and ore genesis: Ore Geology Reviews, v. 89, p.  
38  
39  
40 1251 822-835.  
41  
42 1252 Huang, X.-W., and Beaudoin, G., 2018, Textures and chemical composition of  
43  
44  
45 1253 magnetite from iron oxide-copper-gold (IOCG) and Kiruna-type iron oxide-apatite  
46  
47  
48 1254 (IOA) deposits and their implications for ore genesis and magnetite classification  
49  
50  
51 1255 schemes: Economic Geology (submitted).  
52  
53 1256 Huang, X.-W., Boutroy, É., Makvandi, S., Beaudoin, G., Corriveau, L., and De Toni,  
54  
55  
56 1257 A.F., 2018a, Trace element composition of iron oxides from IOCG and IOA  
57  
58  
59 1258 deposits: relationship to hydrothermal alteration and deposit subtypes: Mineralium  
60  
61  
62  
63  
64  
65

1 1259        *Deposita*. <https://doi.org/10.1007/s00126-018-0825-1>.  
2  
3 1260        Huang, X.-W., Gao, J.-F., Qi, L., Meng, Y.-M., Wang, Y.-C., and Dai, Z.-H., 2016,  
4  
5 1261        In-situ LA-ICP-MS trace elements analysis of magnetite: The Fenghuangshan  
6  
7 1262        Cu-Fe-Au deposit, Tongling, Eastern China: *Ore Geology Reviews*, v. 72, p.  
8  
9 1263        746-759.  
10  
11 1264        Huang, X.-W., Gao, J.-F., Qi, L., and Zhou, M.-F., 2015a, In-situ LA-ICP-MS trace  
12  
13 1265        elemental analyses of magnetite and Re–Os dating of pyrite: The Tianhu  
14  
15 1266        hydrothermally remobilized sedimentary Fe deposit, NW China: *Ore Geology*  
16  
17 1267        *Reviews*, v. 65, p. 900-916.  
18  
19 1268        Huang, X.-W., Qi, L., and Meng, Y.-M., 2014, Trace element geochemistry of  
20  
21 1269        magnetite from the Fe(-Cu) deposits in the Hami region, Eastern Tianshan  
22  
23 1270        Orogenic Belt, NW China: *Acta Geologica Sinica*, v. 88, p. 176-195.  
24  
25 1271        Huang, X.-W., Zhou, M.-F., Beaudoin, G., Gao, J.-F., Qi, L., and Lyu, C., 2018b,  
26  
27 1272        Origin of the volcanic-hosted Yamansu Fe deposit, Eastern Tianshan, NW China:  
28  
29 1273        constraints from pyrite Re-Os isotopes, stable isotopes, and in situ magnetite trace  
30  
31 1274        elements: *Mineralium Deposita*, v. 53, p. 1039-1060.  
32  
33 1275        Huang, X.-W., Zhou, M.-F., Qi, L., Gao, J.-F., and Wang, Y.-W., 2013, Re-Os isotopic  
34  
35 1276        ages of pyrite and chemical composition of magnetite from the Cihai  
36  
37 1277        magmatic-hydrothermal Fe deposit, NW China: *Mineralium Deposita*, v. 48, p.  
38  
39 1278        925-946.  
40  
41 1279        Huang, X.-W., Zhou, M.-F., Qiu, Y.-Z., and Qi, L., 2015b, In-situ LA-ICP-MS trace  
42  
43 1280        elemental analyses of magnetite: The Bayan Obo Fe-REE-Nb deposit, North China:

- 1 1281 Ore Geology Reviews, v. 65, p. 884-899.  
2  
3 1282 Ilton, E.S., and Eugster, H.P., 1989, Base metal exchange between magnetite and a  
4  
5  
6 1283 chloride-rich hydrothermal fluid: *Geochimica et Cosmochimica Acta*, v. 53, p.  
7  
8  
9 1284 291-301.  
10  
11 1285 Ishihara, S., 1977, The magnetite-series and ilmenite-series granitic rocks: *Mining*  
12  
13  
14 1286 *Geology*, v. 27, p. 293-305.  
15  
16  
17 1287 Ishihara, S., 1981, The granitoid series and mineralization: *Economic Geology*, v. 75,  
18  
19  
20 1288 p. 458-484.  
21  
22 1289 Jago, C.P., Tosdal, R.M., Cooke, D.R., and Harris, A.C., 2014, Vertical and lateral  
23  
24  
25 1290 variation of mineralogy and chemistry in the Early Jurassic Mt. Milligan alkalic  
26  
27  
28 1291 porphyry Au-Cu deposit, British Columbia, Canada: *Economic Geology*, v. 109, p.  
29  
30  
31 1292 1005-1033.  
32  
33 1293 Jurek, K., and Hulínský, V., 1980, The use and accuracy of the ZAF correction  
34  
35  
36 1294 procedure for the microanalysis of glasses: *Microchimica Acta*, v. 73, p. 183-198.  
37  
38  
39 1295 Knipping, J.L., Bilenker, L.D., Simon, A.C., Reich, M., Barra, F., Deditius, A.P.,  
40  
41  
42 1296 Wälle, M., Heinrich, C.A., Holtz, F., and Munizaga, R., 2015, Trace elements in  
43  
44  
45 1297 magnetite from massive iron oxide-apatite deposits indicate a combined formation  
46  
47  
48 1298 by igneous and magmatic-hydrothermal processes: *Geochimica et Cosmochimica*  
49  
50  
51 1299 *Acta*, v. 171, p. 15-38.  
52  
53 1300 Kirkham, R.V., and Sinclair, W.D., 1995, Porphyry copper, gold, molybdenum,  
54  
55  
56 1301 tungsten, tin, silver, in Taylor, R. P., and Strong, D. F., eds., *Recent Advances in the*  
57  
58  
59 1302 *Geology of Granite-Related Mineral Deposits*, The Canadian Institute of Mining  
60  
61  
62  
63  
64  
65

1 1303 and Metallurgy, Special Volume 39, p. 50-71.

2

3 1304 Kirwin, D., Forster, C., Kavalieris, I., Crane, D., Orssich, C., Panther, C., Garamjav,

4

5

6 1305 D., Munkhbat, T., and Niislelkhuu, G., 2005, The Oyu Tolgoi copper-gold porphyry

7

8

9 1306 deposits, south Gobi, Mongolia: Geodynamics and metallogeny of Mongolia with a

10

11 1307 special emphasis on copper and gold deposits. SEG-IAGOD field trip, p. 14-16.

12

13

14 1308 Kooiman, G.J.A., McLeod, M.J., and Sinclair, W.D., 1986, Porphyry

15

16

17 1309 tungsten-molybdenum orebodies, polymetallic veins and replacement bodies, and

18

19

20 1310 tin-bearing greisen zones in the Fire Tower Zone, Mount Pleasant, New Brunswick:

21

22 1311 Economic Geology, v. 81, p. 1356-1373.

23

24

25 1312 Kouzmanov, K., von Quadt, A., Peytcheva, I., Harris, C., Heinrich, C.A., Rosu, E.,

26

27

28 1313 and O'Connor, G., 2005, Rosia Poieni porphyry Cu-Au and Rosia Montana

29

30

31 1314 epithermal Au-Ag deposits, Apuseni Mts., Romania: Timing of magmatism and

32

33

34 1315 related mineralisation: Bulgarian Academy of Sciences, Geochemistry, Mineralogy

35

36 1316 and Petrology, v. 43, p. 113-117.

37

38

39 1317 Kroll, T., Müller, D., Seifert, T., Herzig, P.M., and Schneider, A., 2002, Petrology and

40

41

42 1318 geochemistry of the shoshonite-hosted Skouries porphyry Cu–Au deposit,

43

44

45 1319 Chalkidiki, Greece: Mineralium Deposita, v. 37, p. 137-144.

46

47

48 1320 Le Bas, M.J., Le Maitre, R.W., Streckeisen, A., and Zanettin, B., 1986, A chemical

49

50 1321 classification of volcanic rocks based on the total alkali-silica diagram: Journal of

51

52 1322 petrology, v. 27, p. 745-750.

53

54

55 1323 Lee, L., and Helsel, D., 2007, Statistical analysis of water-quality data containing

56

57

58 1324 multiple detection limits II: S-language software for nonparametric distribution

59

60

61

62

63

64

65

- 1 1325 modeling and hypothesis testing: Computers & Geosciences, v. 33, p. 696-704.  
2  
3 1326 LeFort, D., Hanley, J., and Guillong, M., 2011, Subepithermal Au-Pd Mineralization  
4  
5 1327 Associated with an Alkalic Porphyry Cu-Au Deposit, Mount Milligan, Quesnel  
6  
7 1328 Terrane, British Columbia, Canada: Economic Geology, v. 106, p. 781-808.  
8  
9 1329 Li, G., 2012, Iron Ore Deposits in the Eastern Tianshan Orogenic Belt (China): the  
10  
11 1330 Magnetite-Skarn-Magmatism Association: Unpub. PhD thesis thesis, University of  
12  
13 1331 Orleans.  
14  
15 1332 Logan, J.M., and Mihalynuk, M.G., 2014, Tectonic controls on early Mesozoic paired  
16  
17 1333 alkaline porphyry deposit belts (Cu-Au±Ag-Pt-Pd-Mo) within the Canadian  
18  
19 1334 Cordillera: Economic Geology, v. 109, p. 827-858.  
20  
21 1335 Lund, K., Aleinikoff, J.N., Kunk, M.J., Unruh, D.M., Zeihen, G.D., Hodges, W.C., du  
22  
23 1336 Bray, E.A., and O'Neill, J.M., 2002, SHRIMP U-Pb and <sup>40</sup>Ar/<sup>39</sup>Ar age constraints  
24  
25 1337 for relating plutonism and mineralization in the Boulder Batholith region, Montana:  
26  
27 1338 Economic Geology, v. 97, p. 241-267.  
28  
29 1339 Müller, A., Herrington, R., Armstrong, R., Seltmann, R., Kirwin, D.J., Stenina, N.G.,  
30  
31 1340 and Kronz, A., 2010, Trace elements and cathodoluminescence of quartz in  
32  
33 1341 stockwork veins of Mongolian porphyry-style deposits: Mineralium Deposita, v. 45,  
34  
35 1342 p. 707-727.  
36  
37 1343 Müller, D., and Groves, D.I., 1993, Direct and indirect associations between potassic  
38  
39 1344 igneous rocks, shoshonites and gold-copper deposits: Ore Geology Reviews, v. 8, p.  
40  
41 1345 383-406.  
42  
43 1346 Müller, D., and Groves, D.I., 2000, Potassic igneous rocks and associated gold-copper  
44  
45  
46  
47  
48  
49  
50  
51  
52  
53  
54  
55  
56  
57  
58  
59  
60  
61  
62  
63  
64  
65

1 1347 mineralization: Berlin, Springer.  
2  
3 1348 Makvandi, S., Beaudoin, G., McClenaghan, M.B., and Quirt, D., 2017, Geochemistry  
4  
5  
6 1349 of magnetite and hematite from unmineralized bedrock and local till at the  
7  
8  
9 1350 Kiggavik uranium deposit: Implications for sediment provenance: Journal of  
10  
11  
12 1351 Geochemical Exploration, v. 183, p. 1-21.  
13  
14 1352 Makvandi, S., Ghasemzadeh-Barvarz, M., Beaudoin, G., Grunsky, E.C.,  
15  
16  
17 1353 McClenaghan, M.B., and Duchesne, C., 2016a, Principal component analysis of  
18  
19  
20 1354 magnetite composition from volcanogenic massive sulfide deposits: Case studies  
21  
22  
23 1355 from the Izok Lake (Nunavut, Canada) and Halfmile Lake (New Brunswick,  
24  
25  
26 1356 Canada) deposits: Ore Geology Reviews, v. 72, p. 60-85.  
27  
28 1357 Makvandi, S., Ghasemzadeh-Barvarz, M., Beaudoin, G., Grunsky, E.C.,  
29  
30  
31 1358 McClenaghan, M.B., Duchesne, C., and Boutroy, E., 2016b, Partial least  
32  
33  
34 1359 squares-discriminant analysis of trace element compositions of magnetite from  
35  
36  
37 1360 various VMS deposit subtypes: Application to mineral exploration: Ore Geology  
38  
39  
40 1361 Reviews, v. 78, p. 388-408.  
41  
42 1362 McQueen, K.G., and Cross, A.J., 1998, Magnetite as a geochemical sampling medium:  
43  
44  
45 1363 application to skarn deposits, *in* Eggleton, R. A., ed., The State of the Regolith:  
46  
47  
48 1364 Brisbane, Geological Society of Australia, p. 194-199.  
49  
50 1365 Meinert, L.D., Dipple, G.M., and Nicolescu, S., 2005, World skarn deposits, *in*  
51  
52  
53 1366 Hedenquist, J. W., Thompson, J. F. H., Goldfarb, R. J., and Richards, J. P., eds.,  
54  
55  
56 1367 Economic Geology 100th Anniversary Volume: Littleton, Colorado, Society of  
57  
58  
59 1368 Economic Geologists, p. 299-336.  
60  
61  
62  
63  
64  
65

1 1369 Meng, Y.-M., and Hu, R.-Z., 2018, Minireview: Advances in Germanium Isotope  
2  
3 1370 Analysis by Multiple Collector-Inductively Coupled Plasma-Mass Spectrometry:  
4  
5  
6 1371 Analytical Letters, v. 51, p. 627-647.  
7  
8  
9 1372 Meng, Y.M., Hu, R.Z., Huang, X.W., and Gao, J.F., 2017, Germanium in magnetite: A  
10  
11 1373 preliminary review: Acta Geologica Sinica (English Edition), v. 91, p. 711-726.  
12  
13  
14 1374 Middelburg, J.J., van der Weijden, C.H., and Woittiez, J.R.W., 1988, Chemical  
15  
16  
17 1375 processes affecting the mobility of major, minor and trace elements during  
18  
19  
20 1376 weathering of granitic rocks: Chemical Geology, v. 68, p. 253-273.  
21  
22  
23 1377 Milu, V., Milesi, J.-P., and Leroy, J.L., 2004, Rosia Poieni copper deposit, Apuseni  
24  
25 1378 Mountains, Romania: advanced argillic overprint of a porphyry system:  
26  
27  
28 1379 Mineralium Deposita, v. 39, p. 173-188.  
29  
30  
31 1380 Mountjoy, D., 2011, Granitoid-hosted magnetite as an indicator mineral for porphyry  
32  
33  
34 1381 Cu ore deposits: Unpub. B.Sc. thesis thesis, University of Victoria, 41 p.  
35  
36  
37 1382 Mysen, B., 2012, High-pressure and high-temperature titanium solution mechanisms  
38  
39 1383 in silicate-saturated aqueous fluids and hydrous silicate melts: American  
40  
41  
42 1384 Mineralogist, v. 97, p. 1241-1251.  
43  
44  
45 1385 Nadoll, P., 2011, Geochemistry of magnetite from hydrothermal ore deposits and host  
46  
47 1386 rocks-case studies from the Proterozoic Belt Supergroup, Cu-Mo-porphyry+skarn  
48  
49  
50 1387 and Climax-Mo deposits in the western United states: Unpub. PhD dissertation  
51  
52  
53 1388 thesis, The University of Auckland.  
54  
55  
56 1389 Nadoll, P., Angerer, T., Mauk, J.L., French, D., and Walshe, J., 2014, The chemistry of  
57  
58 1390 hydrothermal magnetite: A review: Ore Geology Reviews, v. 61, p. 1-32.  
59  
60  
61  
62  
63  
64  
65



1 1391 Nadoll, P., Mauk, J.L., Hayes, T.S., Koenig, A.E., and Box, S.E., 2012, *Geochemistry*  
2  
3 1392 of magnetite from hydrothermal ore deposits and host rocks of the Mesoproterozoic  
4  
5  
6 1393 Belt Supergroup, United States: *Economic Geology*, v. 107, p. 1275-1292.  
7  
8  
9 1394 Nadoll, P., Mauk, J.L., Leveille, R.A., and Koenig, A.E., 2015, *Geochemistry of*  
10  
11 1395 magnetite from porphyry Cu and skarn deposits in the southwestern United States:  
12  
13  
14 1396 *Mineralium Deposita*, v. 50, p. 493-515.  
15  
16  
17 1397 Nielsen, R.L., Forsythe, L.M., Gallahan, W.E., and Fisk, M.R., 1994, Major- and  
18  
19  
20 1398 trace-element magnetite-melt equilibria: *Chemical geology*, v. 117, p. 167-191.  
21  
22  
23 1399 Pass, H.E., Cooke, D.R., Davidson, G., Maas, R., Dipple, G., Rees, C., Ferreira, L.,  
24  
25  
26 1400 Taylor, C., and Deyell, C.L., 2014, Isotope geochemistry of the Northeast zone,  
27  
28 1401 Mount Polley alkalic Cu-Au-Ag porphyry deposit, British Columbia: A case for  
29  
30  
31 1402 carbonate assimilation: *Economic Geology*, v. 109, p. 859-890.  
32  
33  
34 1403 Pearce, J.A., and Cann, J., 1973, Tectonic setting of basic volcanic rocks determined  
35  
36 1404 using trace element analyses: *Earth and planetary science letters*, v. 19, p. 290-300.  
37  
38  
39 1405 Perelló, J., Raziq, A., and Schloderer, J., 2008, The Chagai porphyry copper belt,  
40  
41  
42 1406 Baluchistan province, Pakistan: *Economic Geology*, v. 103, p. 1583-1612.  
43  
44  
45 1407 Perello, J., Cox, D., Garamjav, D., Sanjdorj, S., Diakov, S., Schissel, D., Munkhbat,  
46  
47  
48 1408 T.-O., and Oyun, G., 2001, Oyu Tolgoi, Mongolia: siluro-devonian porphyry  
49  
50 1409 Cu-Au-(Mo) and high-sulfidation Cu mineralization with a cretaceous chalcocite  
51  
52  
53 1410 blanket: *Economic Geology*, v. 96, p. 1407-1428.  
54  
55  
56 1411 Pisiak, L.K., Canil, D., Lacourse, T., Plouffe, A., and Ferbey, T., 2017, Magnetite as  
57  
58  
59 1412 an indicator mineral in the exploration of porphyry deposits: A case study in till  
60  
61  
62  
63  
64  
65

1 1413 near the Mount Polley Cu-Au deposit, British Columbia, Canada: *Economic*  
2  
3 1414 *Geology*, v. 112, p. 919-940.  
4  
5  
6 1415 Pollard, P.J., 2006, An intrusion-related origin for Cu-Au mineralization in iron  
7  
8 1416 oxide-copper-gold (IOCG) provinces: *Mineralium Deposita*, v. 41, p. 179-187.  
9  
10  
11 1417 Porter, T.M., 2016, The geology, structure and mineralisation of the Oyu Tolgoi  
12  
13 1418 porphyry copper-gold-molybdenum deposits, Mongolia: A review: *Geoscience*  
14  
15 1419 *Frontiers*, v. 7, p. 375-407.  
16  
17  
18 1420 Proffett, J.M., 2003, Geology of the Bajo de la Alumbrera porphyry copper-gold  
19  
20 1421 deposit, Argentina: *Economic Geology*, v. 98, p. 1535-1574.  
21  
22  
23 1422 Raziq, A., Tosdal, R.M., and Creaser, R.A., 2014, Temporal evolution of the  
24  
25 1423 western porphyry Cu-Au systems at Reko Diq, Balochistan, western Pakistan:  
26  
27 1424 *Economic Geology*, v. 109, p. 2003-2021.  
28  
29  
30 1425 Redmond, P.B., and Einaudi, M.T., 2010, The Bingham Canyon porphyry Cu-Mo-Au  
31  
32 1426 deposit. I. Sequence of intrusions, vein formation, and sulfide deposition:  
33  
34 1427 *Economic Geology*, v. 105, p. 43-68.  
35  
36  
37 1428 Reed, M., Rusk, B., and Palandri, J., 2013, The Butte magmatic-hydrothermal system:  
38  
39 1429 One fluid yields all alteration and veins: *Economic Geology*, v. 108, p. 1379-1396.  
40  
41  
42 1430 Richards, J.P., 2014, Discussion of Sun et al. (2013): The link between reduced  
43  
44 1431 porphyry copper deposits and oxidized magmas: *Geochimica et Cosmochimica*  
45  
46 1432 *Acta*, v. 126, p. 643-645.  
47  
48  
49 1433 Richards, J.P., Bray, C.J., Channer, D.M.D., and Spooner, E.T.C., 1997, Fluid  
50  
51 1434 chemistry and processes at the Porgera gold deposit, Papua New Guinea:  
52  
53  
54  
55  
56  
57  
58  
59  
60  
61  
62  
63  
64  
65

1 1435 Mineralium Deposita, v. 32, p. 119-132.

2

3 1436 Richards, J.P., Wilkinson, D., and Ullrich, T., 2006, Geology of the Sari Gunay

4

5

6 1437 epithermal gold deposit, northwest Iran: Economic Geology, v. 101, p. 1455-1496.

7

8

9 1438 Richards, J.P., López, G.P., Zhu, J.-J., Creaser, R.A., Locock, A.J., and Mumin, A.H.,

10

11 1439 2017, Contrasting Tectonic Settings and Sulfur Contents of Magmas Associated

12

13

14 1440 with Cretaceous Porphyry Cu±Mo±Au and Intrusion-Related Iron Oxide Cu-Au

15

16

17 1441 Deposits in Northern Chile: Economic Geology, v. 112, p. 295-318.

18

19

20 1442 Richards, J.P., and Mumin, A.H., 2013, Magmatic-hydrothermal processes within an

21

22 1443 evolving Earth: Iron oxide-copper-gold and porphyry Cu±Mo±Au deposits:

23

24

25 1444 Geology, v. 41, p. 767-770.

26

27

28 1445 Roberts, M.P., and Clemens, J.D., 1993, Origin of high-potassium, calc-alkaline,

29

30

31 1446 I-type granitoids: Geology, v. 21, p. 825-828.

32

33

34 1447 Romero, B., Kojima, S., Wong, C., Barra, F., Véliz, W., and Ruiz, J., 2011,

35

36 1448 Molybdenite Mineralization and Re - Os Geochronology of the Escondida and

37

38

39 1449 Escondida Norte Porphyry Deposits, Northern Chile: Resource geology, v. 61, p.

40

41

42 1450 91-100.

43

44

45 1451 Ronacher, E., Richards, J., Reed, M., Bray, C., Spooner, E., and Adams, P., 2004,

46

47 1452 Characteristics and evolution of the hydrothermal fluid in the North zone

48

49

50 1453 high-grade area, Porgera gold deposit, Papua New Guinea: Economic Geology, v.

51

52

53 1454 99, p. 843-867.

54

55

56 1455 Rudnick, R.L., and Gao, S., 2003, Composition of the continental crust, *in* Holland, H.

57

58 1456 D., and Turekian, K. K., eds., Treatise on geochemistry, 3. The crust: Oxford,

59

60

61

62

63

64

65

1 1457 Elsevier-Pergaman, p. 1-64.  
2  
3 1458 Rusk, B.G., Oliver, N.H.S., Zhang, D., Brown, A., Lilly, R., and Jungmann, D., 2009,  
4  
5  
6 1459 Compositions of magnetite and sulfides from barren and mineralized IOCG  
7  
8  
9 1460 deposits in the eastern succession of the Mt Isa Inlier, Australia Proceedings of  
10  
11 1461 GSA Annual Meeting, 18-21 October 2009, Portland, 2009, p. 84.  
12  
13  
14 1462 Rusk, B.G., Reed, M.H., and Dilles, J.H., 2008, Fluid inclusion evidence for  
15  
16  
17 1463 magmatic-hydrothermal fluid evolution in the porphyry copper-molybdenum  
18  
19  
20 1464 deposit at Butte, Montana: *Economic Geology*, v. 103, p. 307-334.  
21  
22  
23 1465 Salvi, S., and Williams-Jones, A.E., 2006, Alteration, HFSE mineralisation and  
24  
25  
26 1466 hydrocarbon formation in peralkaline igneous systems: Insights from the Strange  
27  
28  
29 1467 Lake Pluton, Canada: *Lithos*, v. 91, p. 19-34.  
30  
31 1468 Samson, I.M., 1990, Fluid evolution and mineralization in a subvolcanic granite stock;  
32  
33  
34 1469 the Mount Pleasant W-Mo-Sn deposits, New Brunswick, Canada: *Economic*  
35  
36  
37 1470 *Geology*, v. 85, p. 145-163.  
38  
39 1471 Savard, D., Barnes, S.J., Dare, S., and Beaudoin, G., 2012, Improved calibration  
40  
41  
42 1472 technique for magnetite analysis by LA-ICP-MS: *Mineralogical Magazine*, v. 76, p.  
43  
44  
45 1473 2329.  
46  
47 1474 Selby, D., and Creaser, R.A., 2001, Re-Os geochronology and systematics in  
48  
49  
50 1475 molybdenite from the Endako porphyry molybdenum deposit, British Columbia,  
51  
52  
53 1476 Canada: *Economic Geology*, v. 96, p. 197-204.  
54  
55  
56 1477 Selby, D., Nesbitt, B.E., Muehlenbachs, K., and Prochaska, W., 2000, Hydrothermal  
57  
58  
59 1478 alteration and fluid chemistry of the Endako porphyry molybdenum deposit, British  
60  
61  
62  
63  
64  
65

1 1479 Columbia: Economic Geology, v. 95, p. 183-202.  
2  
3 1480 Schwartz, M., and Melcher, F., 2004, The Falémé iron district, Senegal: Economic  
4  
5  
6 1481 Geology, v. 99, p. 917-939.  
7  
8  
9 1482 Seedorf, E., 2005, Porphyry deposits: Characteristics and origin of hypogene features:  
10  
11 1483 Economic Geology, v. 100, p. 251-298.  
12  
13  
14 1484 Shchekina, T.I., and Gramenitskii, E.N., 2008, Geochemistry of Sc in the magmatic  
15  
16 1485 process: experimental evidence: Geochemistry International, v. 46, p. 351-366.  
17  
18  
19  
20 1486 Shimazaki, H., 1998, On the occurrence of silician magnetites: Resource Geology, v.  
21  
22 1487 48, p. 23-29.  
23  
24  
25 1488 Sievwright, R.H., Wilkinson, J.J., O'Neill, H.S.C., and Berry, A.J., 2017,  
26  
27 1489 Thermodynamic controls on element partitioning between titanomagnetite and  
28  
29 1490 andesitic–dacitic silicate melts: Contributions to Mineralogy and Petrology, v. 172,  
30  
31 1491 p. 1-33.  
32  
33  
34  
35  
36 1492 Sillitoe, R.H., 1979, Some thoughts on gold-rich porphyry copper deposits:  
37  
38 1493 Mineralium Deposita, v. 14, p. 161-174.  
39  
40  
41  
42 1494 Sillitoe, R.H., 1997, Characteristics and controls of the largest porphyry copper-gold  
43  
44 1495 and epithermal gold deposits in the circum-Pacific region: Australian Journal of  
45  
46 1496 Earth Sciences, v. 44, p. 373-388.  
47  
48  
49  
50 1497 Sillitoe, R.H., 2000, Gold-rich porphyry deposits: descriptive and genetic models and  
51  
52 1498 their role in exploration and discovery: Reviews in Economic Geology, v. 13, p.  
53  
54 1499 315-345.  
55  
56  
57  
58 1500 Sillitoe, R.H., 2003, Iron oxide-copper-gold deposits: an Andean view: Mineralium  
59  
60  
61  
62  
63  
64  
65

1 1501 Deposita, v. 38, p. 787-812.

2

3 1502 Sillitoe, R.H., 2010, Porphyry copper systems: Economic Geology, v. 105, p. 3-41.

4

5

6 1503 Simon, A.C., Knipping, J., Reich, M., Barra, F., Deditius, A.P., Bilenker, L., and

7

8

9 1504 Childress, T., 2018, Kiruna-Type Iron Oxide-Apatite (IOA) and Iron Oxide

10

11 1505 Copper-Gold (IOCG) Deposits Form by a Combination of Igneous and

12

13 1506 Magmatic-Hydrothermal Processes: Evidence from the Chilean Iron Belt:

14

15 1507 Economic Geology Special Publications, v. 21, p. 89-114.

16

17

18 1508 Simon, A.C., Pettke, T., Candela, P.A., Piccoli, P.M., and Heinrich, C.A., 2004,

19

20 1509 Magnetite solubility and iron transport in magmatic-hydrothermal environments:

21

22 1510 Geochimica et Cosmochimica Acta, v. 68, p. 4905-4914.

23

24

25 1511 Sinclair, W.D., 1995, Porphyry W, *in* Lefebure, D. V., and Ray, G. E., eds., Selected

26

27 1512 British Columbia Mineral Deposit Profiles, Volume 1 - Metallics and Coal: British

28

29 1513 Columbia Ministry of Energy, Mines and Petroleum Resources, Open File 1995-20,

30

31 1514 p. 101-104.

32

33

34 1515 Sinclair, W.D., 2007, Porphyry deposits, *in* Goodfellow, W. D., ed., Mineral deposits

35

36 1516 of Canada: A synthesis of major deposit-types, district metallogeny, the evolution

37

38 1517 of geological provinces, and exploration methods, Geological Association of

39

40 1518 Canada, Mineral Deposits Division, Special Publication No. 5, p. 223-243.

41

42

43 1519 Singer, D.A., 1995, World class base and precious metal deposits; a quantitative

44

45 1520 analysis: Economic Geology, v. 90, p. 88-104.

46

47

48 1521 Singoyi, B., Danyushevsky, L., Davidson, G.J., Large, R., and Zaw, K., 2006,

49

50 1522 Determination of trace elements in magnetites from hydrothermal deposits using

51

52

53

54

55

56

57

58

59

60

61

62

63

64

65

1 1523 the LA ICP-MS technique: SEG Keystone Conference, Denver, USA, CD-ROM,  
2  
3 1524 2006.  
4  
5  
6 1525 Sossi, P.A., Prytulak, J., and O'Neill, H.S.C., 2018, Experimental calibration of  
7  
8  
9 1526 vanadium partitioning and stable isotope fractionation between hydrous granitic  
10  
11 1527 melt and magnetite at 800°C and 0.5 GPa: Contributions to Mineralogy and  
12  
13 1528 Petrology, v. 173, p. 27.  
14  
15  
16  
17 1529 Sun, W., Arculus, R.J., Kamenetsky, V.S., and Binns, R.A., 2004, Release of  
18  
19  
20 1530 gold-bearing fluids in convergent margin magmas prompted by magnetite  
21  
22 1531 crystallization: Nature, v. 431, p. 975-978.  
23  
24  
25 1532 Tanis, E.A., Simon, A., Tschauner, O., Chow, P., Xiao, Y., Burnley, P., Cline, C.J.,  
26  
27  
28 1533 Hanchar, J.M., Pettke, T., and Shen, G., 2015, The mobility of Nb in  
29  
30 1534 rutile-saturated NaCl-and NaF-bearing aqueous fluids from 1–6.5 GPa and 300–  
31  
32 1535 800°C: American Mineralogist, v. 100, p. 1600-1609.  
33  
34  
35  
36 1536 Tanis, E.A., Simon, A., Zhang, Y., Chow, P., Xiao, Y., Hanchar, J.M., Tschauner, O.,  
37  
38  
39 1537 and Shen, G., 2016, Rutile solubility in NaF–NaCl–KCl-bearing aqueous fluids at  
40  
41 1538 0.5–2.79 GPa and 250–650°C: Geochimica et Cosmochimica Acta, v. 177, p.  
42  
43 1539 170-181.  
44  
45  
46  
47 1540 Titley, S.R., 1990, Evolution and style of fracture permeability in intrusion-centered  
48  
49 1541 hydrothermal systems, in Titley, S. R., ed., The role of fluids in crustal processes:  
50  
51 1542 Washington DC, National Academic Press, p. 50-63.  
52  
53  
54  
55 1543 Toplis, M., and Carroll, M., 1995, An experimental study of the influence of oxygen  
56  
57 1544 fugacity on Fe-Ti oxide stability, phase relations, and mineral—melt equilibria in  
58  
59  
60  
61  
62  
63  
64  
65

1 1545 ferro-basaltic systems: *Journal of Petrology*, v. 36, p. 1137-1170.

2

3 1546 Toplis, M.J., and Corgne, A., 2002, An experimental study of element partitioning

4

5

6 1547 between magnetite, clinopyroxene and iron-bearing silicate liquids with particular

7

8

9 1548 emphasis on vanadium: *Contributions to Mineralogy and Petrology*, v. 144, p.

10

11 1549 22-37.

12

13

14 1550 Tornos, F., Velasco, F., Barra, F., and Morata, D., 2010, The Tropezón Cu–Mo–(Au)

15

16

17 1551 deposit, Northern Chile: the missing link between IOCG and porphyry copper

18

19

20 1552 systems?: *Mineralium Deposita*, v. 45, p. 313-321.

21

22

23 1553 Ulrich, T., and Heinrich, C.A., 2001, Geology and alteration geochemistry of the

24

25 1554 porphyry Cu-Au deposit at Bajo de la Alumbrera, Argentina: *Economic Geology*, v.

26

27

28 1555 96, p. 1719-1742.

29

30

31 1556 Vigar, A., 2014, Valuation Report on the Kharmagtai Project, Mongolia.

32

33

34 1557 Vila, T., and Sillitoe, R.H., 1991, Gold-rich porphyry systems in the Maricunga belt,

35

36 1558 northern Chile: *Economic Geology*, v. 86, p. 1238-1260.

37

38

39 1559 Watenphul, A., Schmidt, C., and Scholten, L., 2012, First insights into Cr<sup>3+</sup> solubility

40

41

42 1560 in aqueous fluids at elevated P and T by m-XRF, 1st European Mineralogical

43

44 1561 Conference-EMC: Frankfurt, Germany #544 (abstr.).

45

46

47 1562 Watenphul, A., Scholten, L., Kavner, A., Alraun, P., Falkenberg, G., Newville, M.,

48

49

50 1563 Lanzirotti, A., and Schmidt, C., 2013, Cu and Ni solubility in high-temperature

51

52 1564 aqueous fluids, American geophysical Union-AGU, Fall meeting: San Francisco,

53

54 1565 CA, USA #MR33A-2311 (abstr.).

55

56

57

58 1566 Webster, J.D., and Holloway, J.R., 1990, Partitioning of F and Cl between

59

60

61

62

63

64

65



1 1567 magmatic—hydrothermal fluids and highly evolved granitic magmas, *in* Stein, H. J.,  
2  
3 1568 and Hanah, J. L., eds., *Ore-bearing granite systems: petrogenesis and mineralizing*  
4  
5  
6 1569 processes, Geological Society of America Special Paper 246, p. 21-34.  
7  
8  
9 1570 Wen, G., Li, J.-W., Hofstra, A.H., Koenig, A.E., Lowers, H.A., and Adams, D., 2017,  
10  
11 1571 Hydrothermal reequilibration of igneous magnetite in altered granitic plutons and  
12  
13  
14 1572 its implications for magnetite classification schemes: Insights from the  
15  
16  
17 1573 Handan-Xingtai iron district, North China Craton: *Geochimica et Cosmochimica*  
18  
19  
20 1574 *Acta*, v. 213, p. 255-270.  
21  
22  
23 1575 Westendorp, R.W., Watkinson, D.H., and Jonasson, I.R., 1991, Silicon-bearing zoned  
24  
25 1576 magnetite crystals and the evolution of hydrothermal fluids at the Ansil Cu-Zn mine,  
26  
27  
28 1577 Rouyn-Noranda, Quebec: *Economic Geology*, v. 86, p. 1110-1114.  
29  
30  
31 1578 Whitten, E.H.T., 1995, Open and closed compositional data in petrology:  
32  
33  
34 1579 *Mathematical geology*, v. 27, p. 789-806.  
35  
36  
37 1580 Williams, P.J., Barton, M.D., Johnson, D.A., Fontbote, L., De Haller, A., Mark, G.,  
38  
39 1581 Oliver, N.H.S., and Marschik, R., 2005, Iron oxide copper-gold deposits: geology,  
40  
41  
42 1582 space-time distribution and possible modes of origin, *in* Hedenquist, J. W.,  
43  
44  
45 1583 Thompson, J. F. H., Goldfarb, R. J., and Richards, J. P., eds., *Economic Geology*  
46  
47  
48 1584 100th Anniversary Volume: Littelton, Colorado, USA, Society of Economic  
49  
50  
51 1585 Geologists, p. 371-405.  
52  
53  
54 1586 Williams-Jones, A.E., and Heinrich, C.A., 2005, 100th Anniversary special paper:  
55  
56 1587 vapor transport of metals and the formation of magmatic-hydrothermal ore deposits:  
57  
58  
59 1588 *Economic Geology*, v. 100, p. 1287-1312.  
60  
61  
62  
63  
64  
65

1 1589 Wilson, A.J., Cooke, D.R., Stein, H.J., Fanning, C.M., Holliday, J.R., and Tedder, I.J.,  
2  
3 1590 2007, U-Pb and Re-Os geochronologic evidence for two alkalic porphyry  
4  
5  
6 1591 ore-forming events in the Cadia district, New South Wales, Australia: *Economic*  
7  
8  
9 1592 *Geology*, v. 102, p. 3-26.

10  
11 1593 Wilson, J.W.J., Kesler, S.E., Cloke, P.L., and Kelly, W.C., 1980, Fluid inclusion  
12  
13 1594 geochemistry of the Granisle and Bell porphyry copper deposits, British Columbia:  
14  
15  
16 1595 *Economic Geology*, v. 75, p. 45-61.

17  
18  
19 1596 Wilson, M., 1996, *Igneous petrogenesis*: London, UK, Chapman & Hall.

20  
21  
22 1597 Wold, S., Sjöström, M., and Eriksson, L., 2001, PLS-regression: a basic tool of  
23  
24  
25 1598 chemometrics: *Chemometrics and Intelligent Laboratory Systems*, v. 58, p.  
26  
27  
28 1599 109-130.

29  
30  
31 1600 Xie, Q., Zhang, Z., Hou, T., Jin, Z., and Santosh, M., 2017, *Geochemistry and oxygen*  
32  
33 1601 *isotope composition of magnetite from the Zhangmatun deposit, North China*  
34  
35  
36 1602 *Craton: Implications for the magmatic-hydrothermal evolution of Cornwall-type*  
37  
38  
39 1603 *iron mineralization: Ore Geology Reviews*, v. 88, p. 57-70.

40  
41  
42 1604 Yang, W.-B., Niu, H.-C., Shan, Q., Sun, W.-D., Zhang, H., Li, N.-B., Jiang, Y.-H., and  
43  
44 1605 Yu, X.-Y., 2014, *Geochemistry of magmatic and hydrothermal zircon from the*  
45  
46  
47 1606 *highly evolved Baerzhe alkaline granite: implications for Zr-REE-Nb*  
48  
49  
50 1607 *mineralization: Mineralium Deposita*, v. 49, p. 451-470.

51  
52  
53 1608 Yang, X.-M., Lentz, D.R., and McCutcheon, S.R., 2003, *Petrochemical evolution of*  
54  
55  
56 1609 *subvolcanic granitoid intrusions within the Late Devonian Mount Pleasant Caldera,*  
57  
58  
59 1610 *southwestern New Brunswick, Canada: comparison of Au versus*

1 1611 Sn-W-Mo-polymetallic mineralization systems: *Atlantic Geology*, v. 39, p. 97-121.  
2  
3 1612 Yi, L., Gu, X., Lu, A., Liu, J., Lei, H., Wang, Z., Cui, Y., Zuo, H., and Shen, C., 2015,  
4  
5 1613 Major and Trace Elements of Magnetite from the Qimantag Metallogenic Belt:  
6  
7 1614 Insights into Evolution of Ore-forming Fluids: *Acta Geologica Sinica (English*  
8  
9 1615 *Edition)*, v. 89, p. 1226-1243.  
10  
11 1616 Zhao, L., Chen, H., Zhang, L., Li, D., Zhang, W., Wang, C., Yang, J., and Yan, X.,  
12  
13 1617 2018, Magnetite geochemistry of the Heijianshan Fe-Cu (-Au) deposit in Eastern  
14  
15 1618 Tianshan: Metallogenic implications for submarine volcanic-hosted Fe-Cu deposits  
16  
17 1619 in NW China: *Ore Geology Reviews*, v. 100, p. 422-440.  
18  
19 1620 Zhao, W.W., and Zhou, M.-F., 2015, In-situ LA-ICP-MS trace elemental analyses of  
20  
21 1621 magnetite: The Mesozoic Tengtie skarn Fe deposit in the Nanling Range, South  
22  
23 1622 China: *Ore Geology Reviews*, v. 65, p. 872-883.  
24  
25  
26  
27  
28  
29  
30  
31  
32  
33  
34  
35  
36  
37  
38  
39  
40  
41  
42  
43  
44  
45  
46  
47  
48  
49  
50  
51  
52  
53  
54  
55  
56  
57  
58  
59  
60  
61  
62  
63  
64  
65

1       1623       **Figure captions**

2  
3       1624

4  
5  
6       1625       Fig. 1. Photomicrographs showing the occurrences of igneous magnetite from the  
7  
8  
9       1626       porphyry deposits. A and B are images under transmitted light, whereas C and D are  
10  
11       1627       images under reflected light. E and F are BSE images. A. Subhedral to anhedral  
12  
13       1628       igneous magnetite disseminated in andesite porphyry from the Mount Milligan Cu-Au  
14  
15       1629       deposit (sample 90-616-191). The andesite is composed of phenocrysts of sericitized  
16  
17       1630       feldspar in a quartzo-feldspathic matrix. B. Anhedral igneous magnetite disseminated  
18  
19       1631       in dacite porphyry from the Reko Diq Cu-Au deposit (sample Spegar1). The dacite is  
20  
21       1632       composed of phenocrysts of plagioclase, K-feldspar, and amphibole in a  
22  
23       1633       quartzo-feldspathic matrix. C. Magnetite occurring as exsolution bands in ilmenite in  
24  
25       1634       andesite porphyry from the Rosia Poieni Cu-Au deposit (sample RP-4-CH-34). D.  
26  
27       1635       Magnetite with ilmenite exsolution lamellae replaced by hematite from the Reko Diq  
28  
29       1636       Cu-Au deposit (sample RK 8). E. Igneous magnetite from the Reko Diq Cu-Au  
30  
31       1637       deposit showing exsolution lamellae of ilmenite (sample RK 22). Some lamellae have  
32  
33       1638       transformed to titanite. F. Magnetite from the Mount Milligan Cu-Au deposit replaced  
34  
35       1639       by chalcopyrite and titanite (sample 90-616-191). Abbreviations: Fsp = feldspar, Kfs  
36  
37       1640       = K-feldspar, Pl = plagioclase, Am = amphibole, Mag = magnetite, Hem = hematite,  
38  
39       1641       Ilm = ilmenite, Ttn = titanite, Ccp = chalcopyrite.

40  
41  
42       1642

43  
44  
45       1643       Fig. 2 Photomicrographs showing the occurrences of hydrothermal magnetite from  
46  
47       1644       the porphyry deposits. All images are under reflected light except image A under

1 1645 transmitted light. A. Hydrothermal magnetite within chlorite-magnetite-chalcopyrite  
2  
3 1646 veinlets from the Oyu Tolgoi Cu-Au-Mo deposit (sample Oyu Tolgoi). Magnetite is  
4  
5  
6 1647 anhedral to subhedral and forms disseminated grains and aggregates in a strongly  
7  
8  
9 1648 sericitized feldspath-rich rock. B. Hydrothermal magnetite in quartz vein from the  
10  
11 1649 Bajo de la Alumbreira Cu-Au deposit (sample 51-61). Magnetite is anhedral and partly  
12  
13  
14 1650 replaced by hematite. C. Hydrothermal magnetite in quartz vein from Butte deposit  
15  
16  
17 1651 (sample 7233D). Magnetite occurs as aggregates of anhedral grains associated with  
18  
19  
20 1652 chalcopyrite and shows evidence of martitization. Small inclusions of chalcopyrite are  
21  
22  
23 1653 common. D. Hydrothermal magnetite in thick magnetite veins from the Reko Diq  
24  
25 1654 Cu-Au deposit (sample RK 5). Subhedral magnetite forms massive aggregates and  
26  
27  
28 1655 displays martitization along spinel planes. E. Hydrothermal magnetite in  
29  
30  
31 1656 magnetite-chalcopyrite-quartz-pyrite vein from Butte deposit (sample 11166-3199).  
32  
33  
34 1657 Magnetite is anhedral, forms massive aggregates, is enclosed by chalcopyrite and  
35  
36  
37 1658 pyrite, hosts small inclusions of chalcopyrite, and is slightly replaced by hematite  
38  
39  
40 1659 along rims. F. Hydrothermal magnetite in magnetite-cemented breccia from  
41  
42 1660 Escondida Norte deposit (sample EN3). Magnetite occurs as small anhedral grains,  
43  
44  
45 1661 partially or totally replaced by hematite (martitization). G. Anhedral to subhedral  
46  
47  
48 1662 hydrothermal magnetite from the Kharmagtai Cu-Au deposit replaced by hematite and  
49  
50  
51 1663 chalcopyrite along the rims and fractures (sample Kharmagtai). H. Anhedral  
52  
53 1664 hydrothermal magnetite from the Skouries Cu-Au deposit showing oscillatory zoning  
54  
55  
56 1665 and nearly totally replaced by hematite (sample 1836). Some magnetite grains were  
57  
58  
59 1666 completely replaced by chalcopyrite resulting in the formation of small magnetite  
60  
61  
62  
63  
64  
65

1 1667 inclusions in chalcopyrite. Abbreviations: Chl = chlorite, Ccp = chalcopyrite, Hem =  
2  
3 1668 hematite, Mag = magnetite, Qz = quartz, Ser = sericite.

4  
5  
6 1669

7  
8  
9 1670 Fig. 3. Back-scattered electron images of zoned magnetite from porphyry deposits.

10  
11 1671 A-B. Hydrothermal magnetite from the Kharmagtai Cu-Au deposit showing zoned

12  
13  
14 1672 textures composed of dark gray and light gray domains (sample Kharmagtai). The

15  
16  
17 1673 dark gray domains are composed of small silicate inclusions. C-D. Hydrothermal

18  
19  
20 1674 magnetite in magnetite-quartz vein from the Bajo de la Alumbrera Cu-Au deposit.

21  
22  
23 1675 Amounts of quartz inclusions and minor ilmenite exsolution lamellae are observed in

24  
25  
26 1676 magnetite. E. Hydrothermal magnetite from the Endako porphyry Mo deposit

27  
28  
29 1677 showing oscillatory zoning that was replaced by hematite (sample 2071). There also

30  
31 1678 minor chalcopyrite inclusions in magnetite. F. Hydrothermal magnetite from the

32  
33  
34 1679 Mount Pleasant porphyry W-Mo deposit composed of Si-rich (dark gray) and Si-poor

35  
36  
37 1680 (light gray) domains (sample SC1). Abbreviations: Mag = magnetite, Hem = hematite,

38  
39 1681 Ilm = ilmenite, Qz = quartz, Ccp = chalcopyrite.

40  
41  
42 1682

43  
44  
45 1683 Fig. 4. Multi-element diagrams of average trace element composition of magnetite

46  
47  
48 1684 from individual deposits, normalized to bulk continental crust (Rudnick and Gao,

49  
50  
51 1685 2003). The light gray lines represent individual analyses, whereas the color lines with

52  
53  
54 1686 symbols represent deposit average. A-B. EPMA data of igneous and hydrothermal

55  
56 1687 magnetite. C-D. LA-ICP-MS data of igneous and hydrothermal magnetite.

57  
58  
59 1688

1 1689 Fig. 5. Box and whisker plots of trace elements in igneous and hydrothermal  
2  
3 1690 magnetite analyzed by EPMA (A) and by LA-ICP-MS (B). The upper and lower  
4  
5  
6 1691 margins of the box represent the upper 75% and lower 25% of the data. The whiskers  
7  
8  
9 1692 represent the upper and lower threshold values (95% data). Median values are shown  
10  
11  
12 1693 as solid black lines and mean values as solid black circles. Outliers are shown as open  
13  
14 1694 circles along the whisker. Data below detection limit are removed from this plot.  
15  
16

17 1695

18  
19  
20 1696 Fig. 6. Box and whisker plots of trace elements in igneous and hydrothermal  
21  
22 1697 magnetite from different types of porphyry deposits. A and C are EPMA data, whereas  
23  
24  
25 1698 B and D are LA-ICP-MS data. The meaning of symbols in box and whisker plot is the  
26  
27  
28 1699 same as that of Fig. 5. Data below detection limit are removed from this plot.  
29  
30

31 1700

32  
33 1701 Fig. 7. PLS-DA of EPMA (A, B) and LA-ICP-MS (C, D) data of igneous and  
34  
35  
36 1702 hydrothermal magnetite from the studied deposits. A. The  $qw^*_1$ - $qw^*_2$  (first and  
37  
38  
39 1703 second loadings) plot based on EPMA data showing correlations among element  
40  
41  
42 1704 variables and magnetite type. B. The  $t_1$ - $t_2$  (first and second scores) plot showing the  
43  
44  
45 1705 distribution of individual analyses of samples in the latent variable space defined by  
46  
47  
48 1706  $qw^*_1$ - $qw^*_2$  in A. C. The  $qw^*_1$ - $qw^*_2$  (first and second loadings) plot based on  
49  
50 1707 LA-ICP-MS data showing correlations among element variables and magnetite type.  
51  
52  
53 1708 D. The  $t_1$ - $t_2$  (first and second scores) plot showing the distribution of individual  
54  
55  
56 1709 analyses of samples in the latent variable space defined by  $qw^*_1$ - $qw^*_2$  in C. Dotted  
57  
58  
59 1710 red line in D roughly separates igneous from hydrothermal magnetite. E-G. Score  
60  
61  
62  
63  
64  
65

1 1711 contribution plots of elements for igneous and hydrothermal magnetite.  
2  
3 1712  
4  
5  
6 1713 Fig. 8. PLS-DA of EPMA data of igneous magnetite from porphyry Cu-Au, Cu-Mo,  
7  
8  
9 1714 and Cu-Mo-Au deposits. A. The  $qw^*_1$ - $qw^*_2$  (first and second loadings) plot showing  
10  
11 1715 correlations among element variables and deposit subtypes. B. The  $t_1$ - $t_2$  (first and  
12  
13 1716 second scores) plot showing the distribution of individual analyses of samples in the  
14  
15 1717 latent variable space defined by  $qw^*_1$ - $qw^*_2$  in A. C-E. Score contribution plots of  
16  
17 1718 elements for hydrothermal magnetite from different types of mineralization. F. The  
18  
19 1719 VIP showing the importance of compositional variables in classification of samples in  
20  
21 1720 B. Gray lines in F represent the VIP value of 1. Elements with VIP value higher than  
22  
23 1721 1 are the most important in the classification.  
24  
25  
26  
27  
28  
29  
30

31 1722  
32  
33 1723 Fig. 9. PLS-DA of EPMA data of hydrothermal magnetite from different types of  
34  
35 1724 porphyry deposits. A. The  $qw^*_1$ - $qw^*_2$  (first and second loadings) plot showing  
36  
37 1725 correlations among element variables and deposit subtypes. B. The  $t_1$ - $t_2$  (first and  
38  
39 1726 second scores) plot showing the distribution of individual analyses of samples in the  
40  
41 1727 latent variable space defined by  $qw^*_1$ - $qw^*_2$  in A. C. The  $qw^*_1$ - $qw^*_3$  (first and third  
42  
43 1728 loadings) plot showing correlations among element variables and deposit subtypes. D.  
44  
45 1729 The  $t_1$ - $t_3$  (first and third scores) plot showing the distribution of individual analyses of  
46  
47 1730 samples in the latent variable space defined by  $qw^*_1$ - $qw^*_3$  in C. E-J. Score  
48  
49 1731 contribution plots of elements for hydrothermal magnetite from different types of  
50  
51 1732 mineralization. K. The VIP showing the importance of compositional variables in  
52  
53  
54  
55  
56  
57  
58  
59  
60  
61  
62  
63  
64  
65



1 1733 classification of samples in B and D. Gray lines in K represent the VIP value of 1.

2  
3 1734 Elements with VIP value higher than 1 are the most important in the classification.

4  
5  
6 1735

7  
8  
9 1736 Fig. 10. PLS-DA of LA-ICP-MS data of hydrothermal magnetite from different types

10  
11 1737 of porphyry deposits. A. The  $q_w^*_1$ - $q_w^*_2$  (first and second loadings) plot showing

12  
13  
14 1738 correlations among element variables and deposit subtypes. B. The  $t_1$ - $t_2$  (first and

15  
16  
17 1739 second scores) plot showing the distribution of individual analyses of samples in the

18  
19  
20 1740 latent variable space defined by  $q_w^*_1$ - $q_w^*_2$  in A. C-F. Score contribution plots of

21  
22  
23 1741 elements for hydrothermal magnetite from different types of mineralization. G. The

24  
25 1742 VIP showing the importance of compositional variables in classification of samples in

26  
27  
28 1743 B. Gray lines in G represent the VIP value of 1. Elements with VIP value higher than

29  
30  
31 1744 1 are the most important in the classification.

32  
33  
34 1745

35  
36 1746 Fig. 11. PLS-DA of EPMA data of igneous magnetite grouped by magmatic affinity of

37  
38  
39 1747 porphyry intrusions. A. The  $q_w^*_1$ - $q_w^*_2$  (first and second loadings) plot showing

40  
41  
42 1748 correlations among element variables and magmatic affinity. B. The  $t_1$ - $t_2$  (first and

43  
44  
45 1749 second scores) plot showing the distribution of individual analyses of samples in the

46  
47  
48 1750 latent variable space defined by  $q_w^*_1$ - $q_w^*_2$  in A. C-E. Score contribution plots of

49  
50  
51 1751 elements for igneous magnetite associated with different magmatic affinities. F. The

52  
53 1752 VIP showing the importance of compositional variables in classification of samples in

54  
55  
56 1753 B. Gray lines in F represent the VIP value of 1. Elements with VIP value higher than 1

57  
58  
59 1754 are the most important in the classification.

1 1755

2  
3 1756 Fig. 12. PLS-DA of EPMA data of hydrothermal magnetite grouped by magmatic  
4  
5  
6 1757 affinity of porphyry intrusions. A. The  $qw^*_1$ - $qw^*_2$  (first and second loadings) plot  
7  
8  
9 1758 showing correlations among element variables and magmatic affinity. B. The  $t_1$ - $t_2$   
10  
11 1759 (first and second scores) plot showing the distribution of individual analyses of  
12  
13 1760 samples in the latent variable space defined by  $qw^*_1$ - $qw^*_2$  in A. C-E. Score  
14  
15 1761 contribution plots of elements for hydrothermal magnetite associated with different  
16  
17 1762 magmatic affinities. F. The VIP showing the importance of compositional variables in  
18  
19 1763 classification of samples in B. Gray lines in F represent the VIP value of 1. Elements  
20  
21 1764 with VIP value higher than 1 are the most important in the classification.  
22  
23  
24  
25  
26  
27

28 1765

29  
30  
31 1766 Fig. 13. PLS-DA of LA-ICP-MS data of hydrothermal magnetite grouped by  
32  
33 1767 magmatic affinity of porphyry intrusions. A. The  $qw^*_1$ - $qw^*_2$  (first and second  
34  
35 1768 loadings) plot showing correlations among element variables and magmatic affinity. B.  
36  
37  
38  
39 1769 The  $t_1$ - $t_2$  (first and second scores) plot showing the distribution of individual analyses  
40  
41 1770 of samples in the latent variable space defined by  $qw^*_1$ - $qw^*_2$  in A. C-E. Score  
42  
43 1771 contribution plots of elements for hydrothermal magnetite associated with different  
44  
45 1772 magmatic affinities. F. The VIP showing the importance of compositional variables in  
46  
47  
48 1773 classification of samples in B. Gray lines in F represent the VIP value of 1. Elements  
49  
50 1774 with VIP value higher than 1 are the most important in the classification.  
51  
52  
53  
54  
55

56 1775

57  
58 1776 Fig. 14. PLS-DA of EPMA data of igneous magnetite hosted by intermediate and  
59  
60  
61  
62  
63  
64  
65

1 1777 felsic porphyry. A. The  $qw^*_1$ - $qw^*_2$  (first and second loadings) plot showing  
2  
3 1778 correlations among element variables and porphyry composition. B. The  $t_1$ - $t_2$  (first  
4  
5  
6 1779 and second scores) plot showing the distribution of individual analyses of samples in  
7  
8  
9 1780 the latent variable space defined by  $qw^*_1$ - $qw^*_2$  in A. C-D. Score contribution plots of  
10  
11  
12 1781 elements for igneous magnetite hosted by intermediate and felsic porphyry.

13  
14  
15 1782

16  
17 1783 Fig. 15. PLS-DA of EPMA data of hydrothermal magnetite grouped by host porphyry  
18  
19  
20 1784 composition. A. The  $qw^*_1$ - $qw^*_2$  (first and second loadings) plot showing correlations  
21  
22 1785 among element variables and porphyry composition. B. The  $t_1$ - $t_2$  (first and second  
23  
24  
25 1786 scores) plot showing the distribution of individual analyses of samples in the latent  
26  
27  
28 1787 variable space defined by  $qw^*_1$ - $qw^*_2$  in A. C-E. Score contribution plots of elements  
29  
30  
31 1788 for hydrothermal magnetite associated with different types of porphyries. F. The VIP  
32  
33  
34 1789 showing the importance of compositional variables in classification of samples in B.  
35  
36 1790 Gray lines in F represent the VIP value of 1.

37  
38  
39 1791

40  
41  
42 1792 Fig. 16. PLS-DA of LA-ICP-MS data of hydrothermal magnetite grouped by host  
43  
44  
45 1793 porphyry composition. A. The  $qw^*_1$ - $qw^*_2$  (first and second loadings) plot showing  
46  
47  
48 1794 correlations among element variables and porphyry composition. B. The  $t_1$ - $t_2$  (first  
49  
50  
51 1795 and second scores) plot showing the distribution of individual analyses of samples in  
52  
53 1796 the latent variable space defined by  $qw^*_1$ - $qw^*_2$  in A. C-E. Score contribution plots of  
54  
55  
56 1797 elements for hydrothermal magnetite associated with different types of porphyries. F.  
57  
58  
59 1798 The VIP showing the importance of compositional variables in classification of  
60

1 1799 samples in B. Gray lines in F represent the VIP value of 1.  
2  
3 1800  
4  
5  
6 1801 Fig. 17. Plots of Ni/Cr versus Ti (A, B) and V versus Ti (C, D) showing the  
7  
8  
9 1802 composition differences between igneous and hydrothermal magnetite from porphyry  
10  
11 1803 deposits. The boundary line (dotted line) between igneous and hydrothermal  
12  
13 1804 magnetite in A is defined by Dare et al. (2014), whereas the fields in B for igneous  
14  
15 1805 and hydrothermal magnetite are defined by the data of Nadoll et al. (2015).  
16  
17 1806  
18  
19  
20 1807 Fig. 18. PLS-DA of EPMA (A, B, E-H, M) and LA-ICP-MS (C, D, I-L, N) data of  
21  
22 1808 hydrothermal magnetite from porphyry Cu, IOCG, IOA, and skarn deposits. EPMA  
23  
24 1809 data sources: porphyry Cu (this study; Dupuis and Beaudoin, 2011), IOCG (Dupuis  
25  
26 1810 and Beaudoin, 2011; Huang et al., 2018a), IOA (Knipping et al., 2015; Huang et al.,  
27  
28 1811 2018a), and skarn deposits (Schwartz and Melcher, 2004; Dupuis and Beaudoin, 2011;  
29  
30 1812 Nadoll, 2011; Li, 2012; Dare et al., 2014; Duan et al., 2014; Hu et al., 2014; Hu et al.,  
31  
32 1813 2017; Xie et al., 2017). LA-ICP-MS data sources: porphyry Cu (this study), IOCG  
33  
34 1814 (Carew, 2004; Gosselin et al., 2006; Dupuis and Beaudoin, 2007; Chen et al., 2015a, b;  
35  
36 1815 Zhao et al., 2016; Huang et al., 2018a), IOA (Knipping et al., 2015; Huang et al.,  
37  
38 1816 2018a), and skarn (Huang et al., 2013, 2016, 2018b; Yi et al., 2015; Zhao and Zhou,  
39  
40 1817 2015; Canil et al., 2016; Hu et al., 2017; Xie et al., 2017) deposits. A and C. The  
41  
42 1818  $qw^*_1$ - $qw^*_2$  (first and second loadings) plot showing correlations among element  
43  
44 1819 variables and deposit types. B and D. The  $t_1$ - $t_2$  (first and second scores) plots showing  
45  
46 1820 the distribution of individual analyses of samples in the latent variable space defined  
47  
48  
49  
50  
51  
52  
53  
54  
55  
56  
57  
58  
59  
60  
61  
62  
63  
64  
65

1 1821 by  $qw^*_1$ - $qw^*_2$  in A and C, respectively. E-H. Score contribution plots of elements  
2  
3 1822 based on EPMA data for hydrothermal magnetite from different types of deposits. I-L.  
4  
5  
6 1823 Score contribution plots of elements based on LA-ICP-MS data for hydrothermal  
7  
8  
9 1824 magnetite from different types of deposits. M and N. The VIPs showing the  
10  
11 1825 importance of compositional variables in classification of samples in B and D,  
12  
13  
14 1826 respectively.  
15  
16

17 1827

18  
19  
20 1828 **Tables**

21  
22 1829 Table 1. Main Characteristics of Studied Porphyry Deposits  
23

24  
25 1830

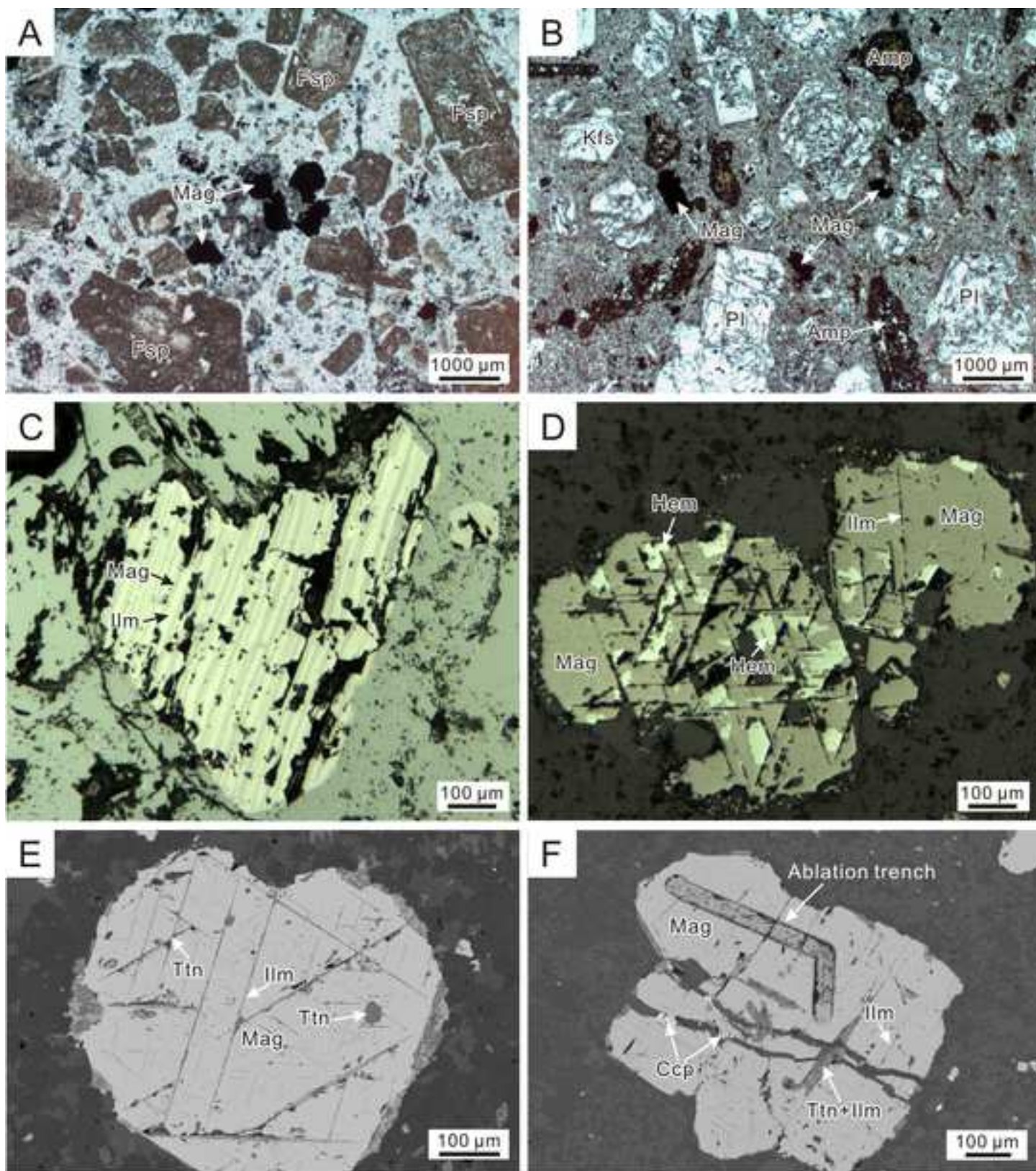
26  
27 1831 Table 2. Summary of Samples Analyzed, Magnetite Types, and Number of Analyses  
28  
29 1832 per Sample  
30

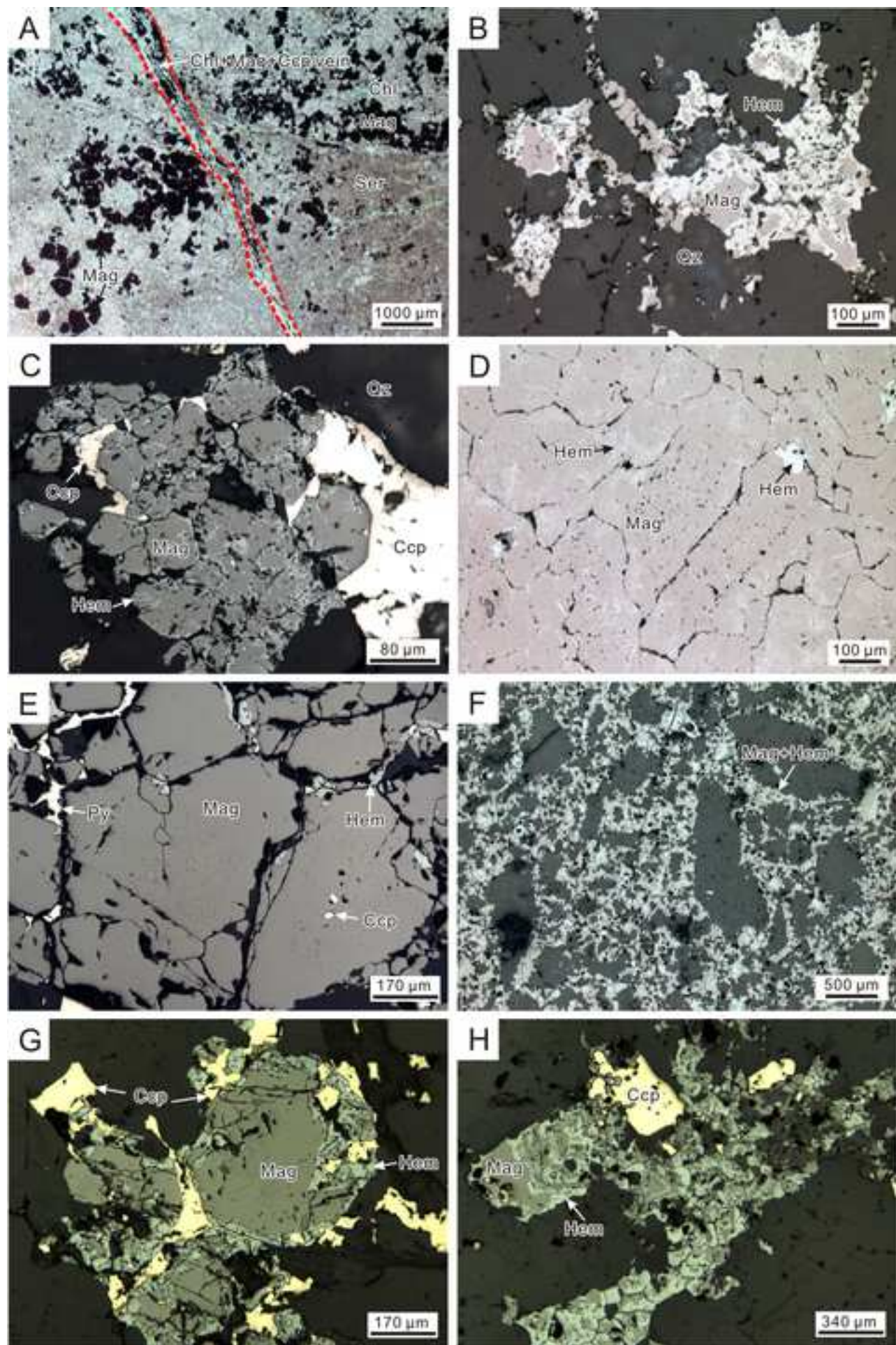
31 1833

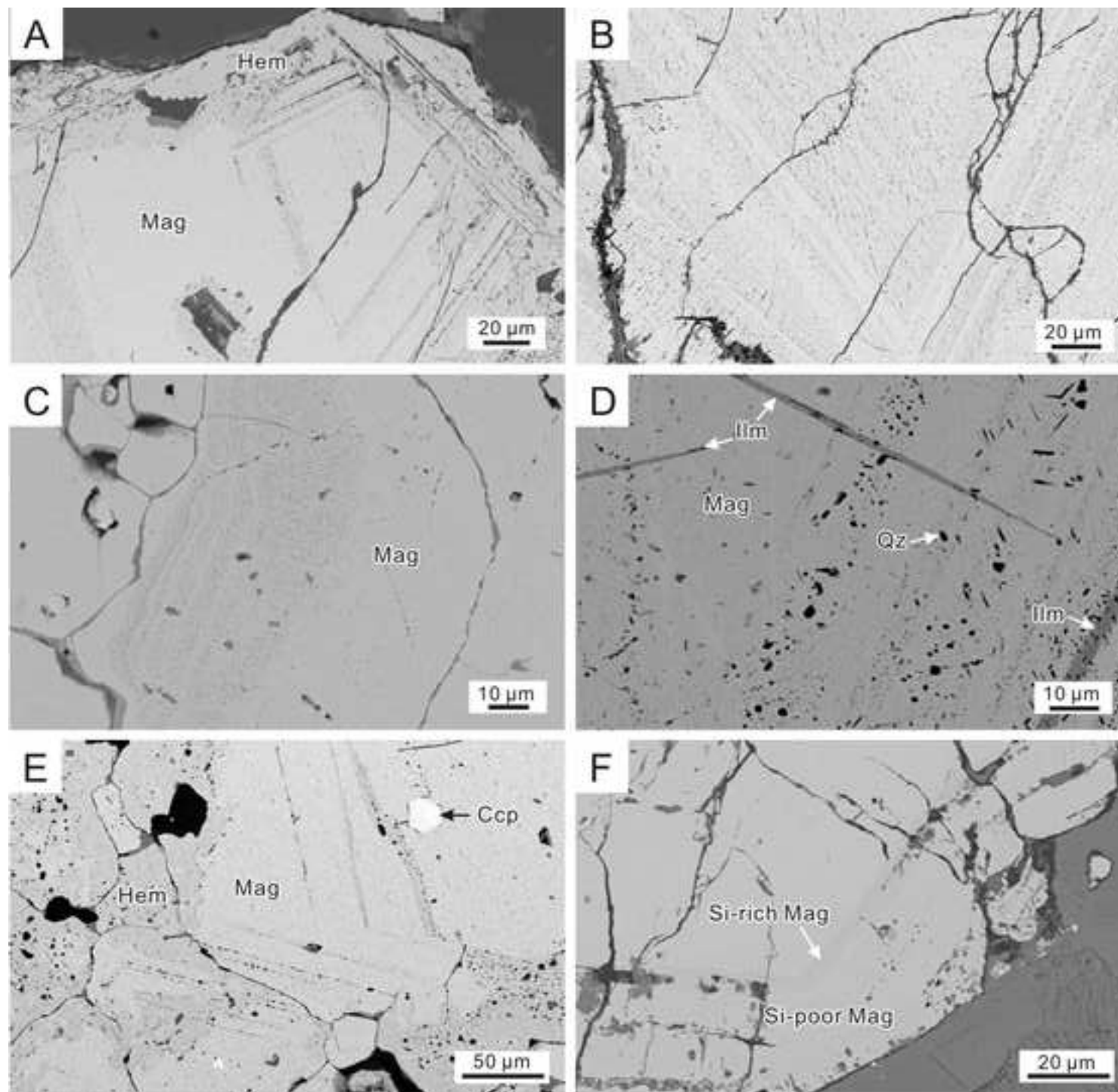
32  
33  
34 1834 **Appendices**

35  
36  
37 1835 Appendix Figures A1-A5  
38

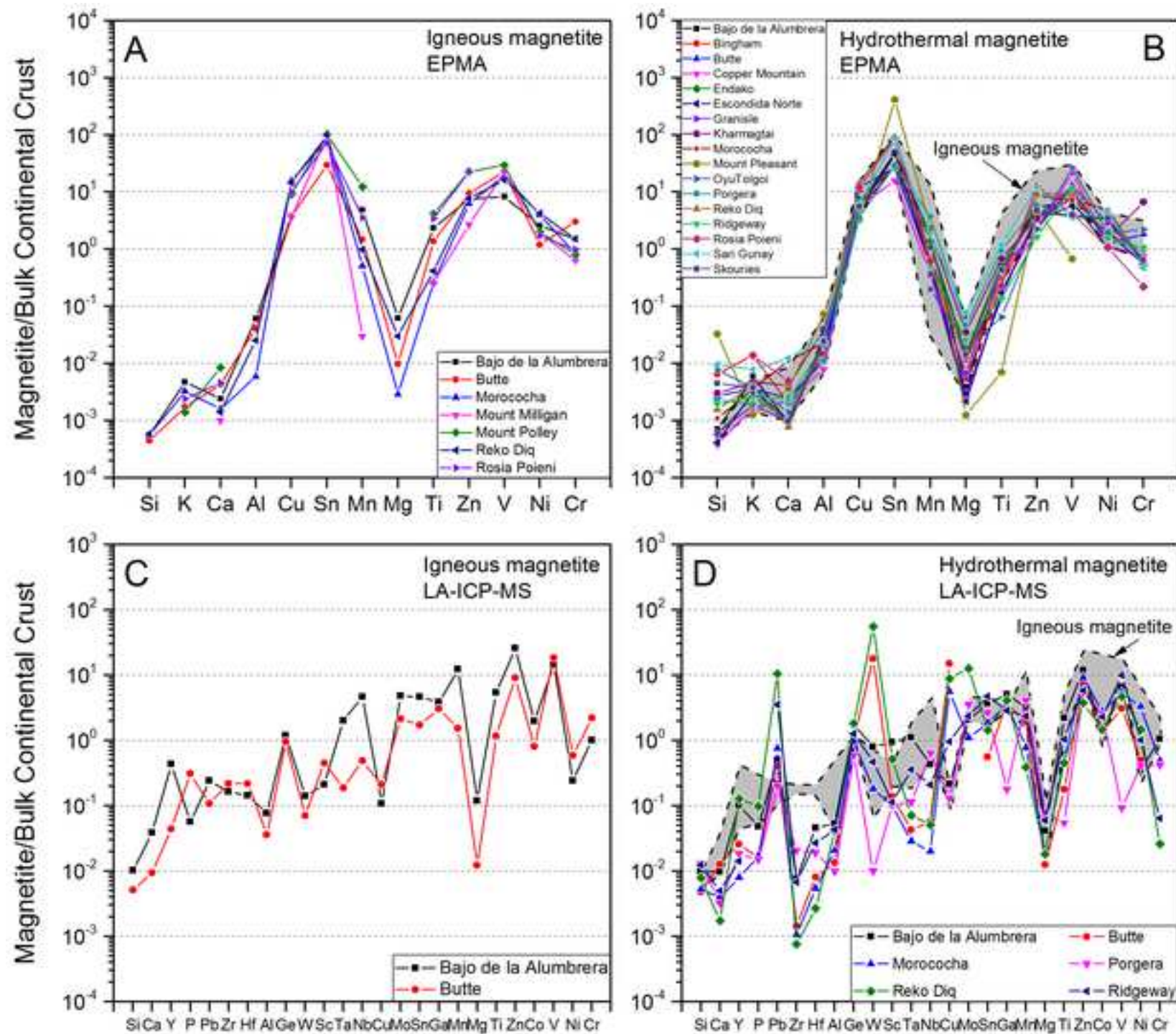
39  
40 1836 Table A1. Full Results of EPMA and LA-ICP-MS Analyses  
41  
42  
43  
44  
45  
46  
47  
48  
49  
50  
51  
52  
53  
54  
55  
56  
57  
58  
59  
60  
61  
62  
63  
64  
65

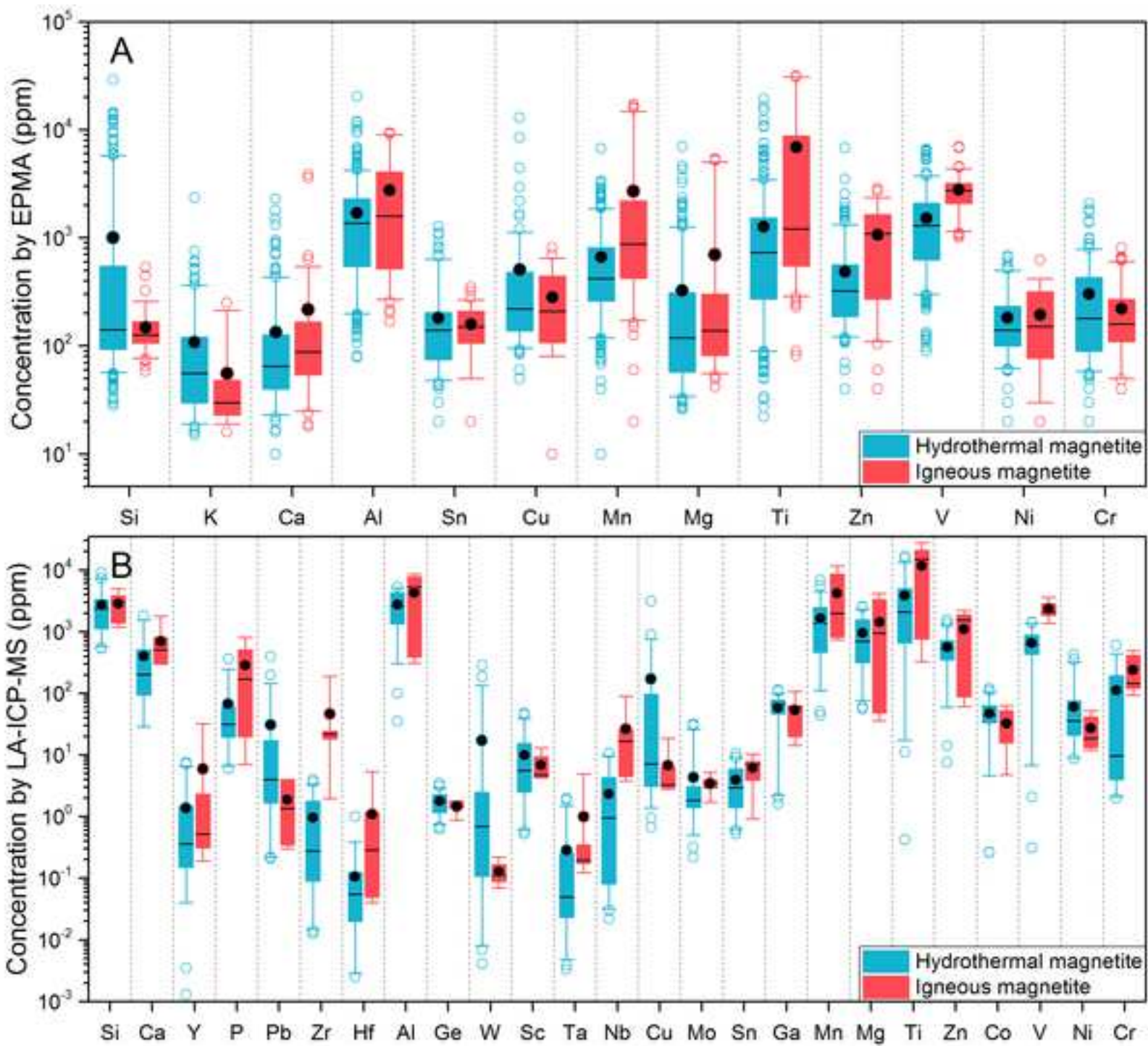


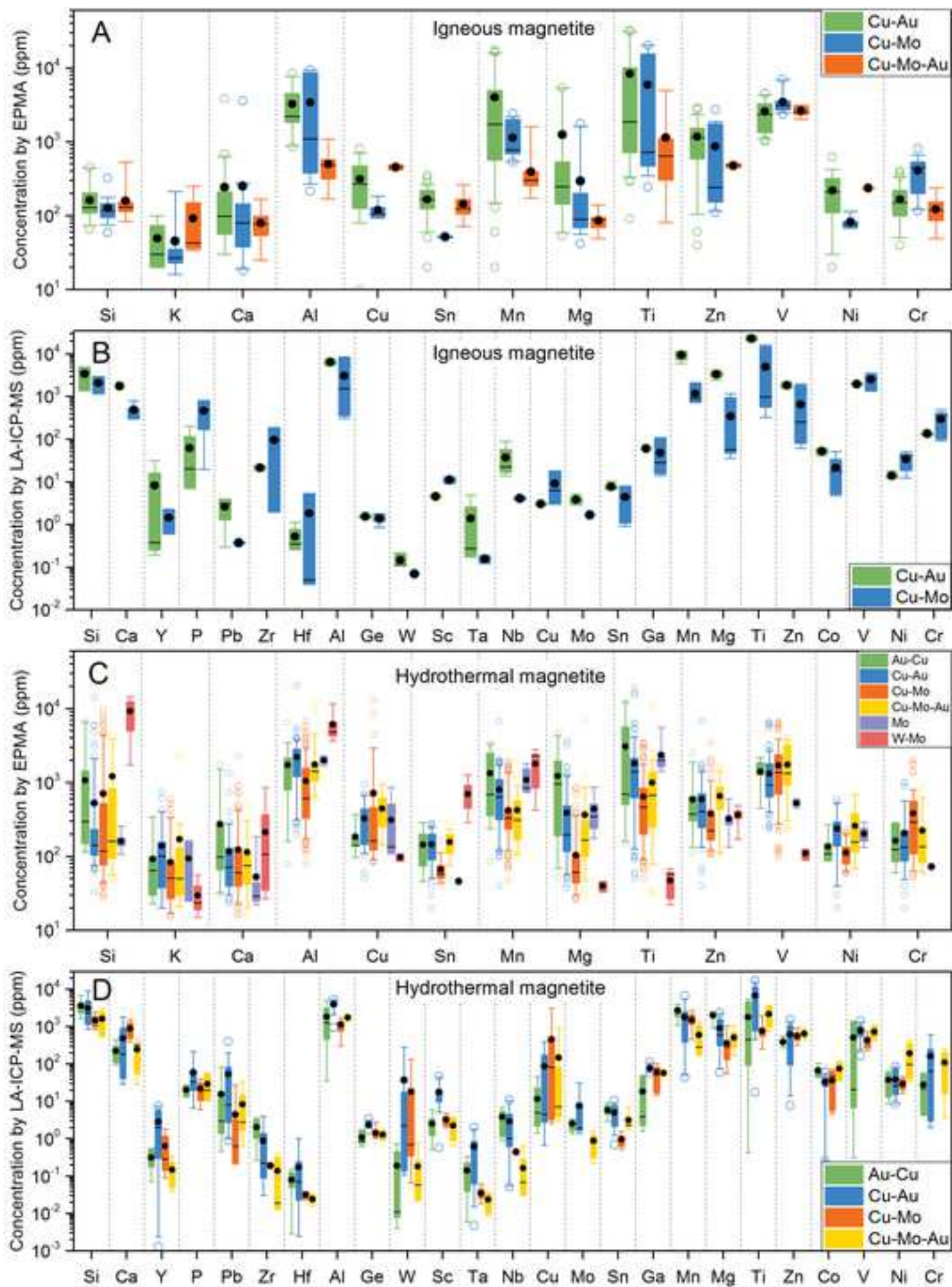


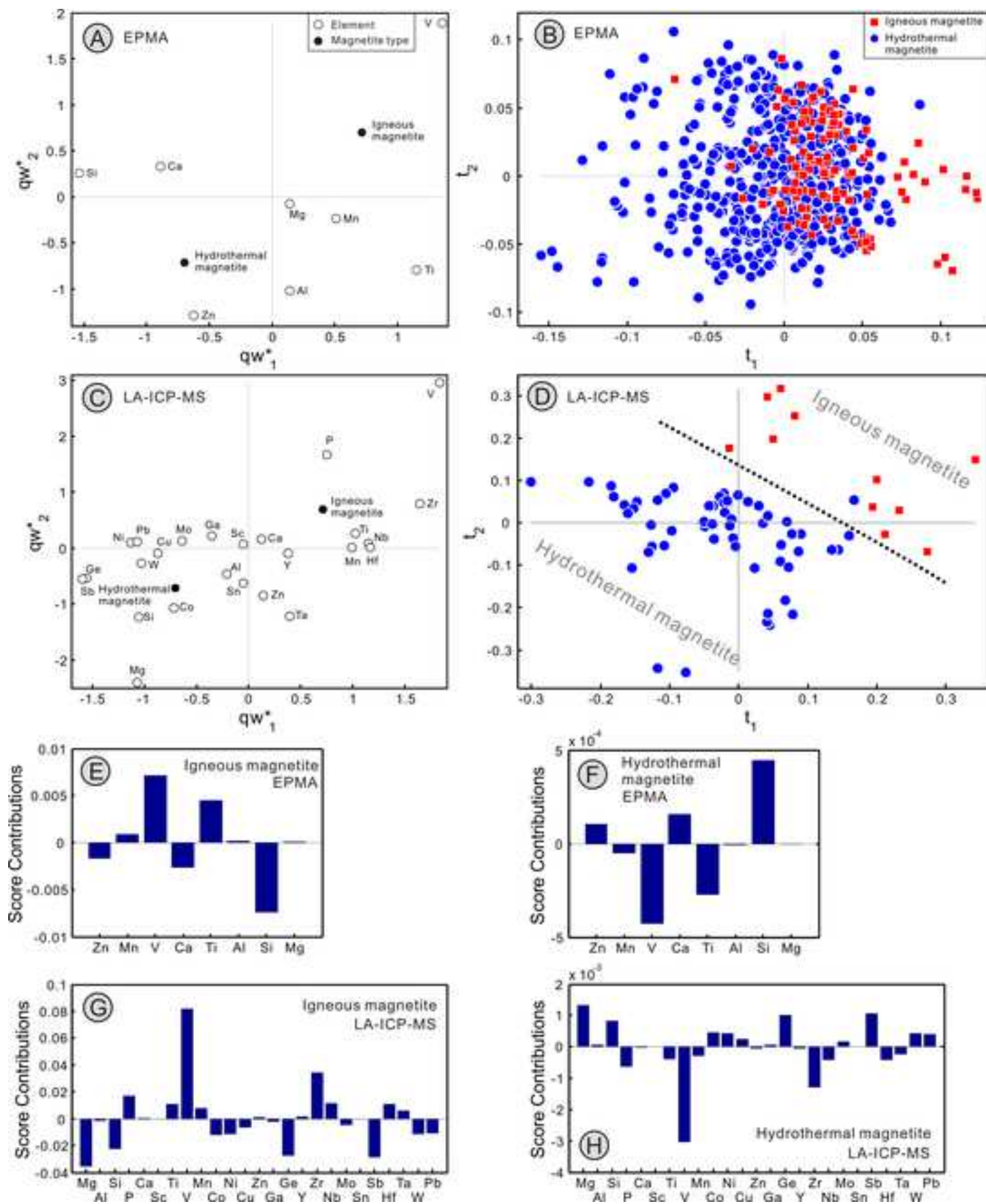


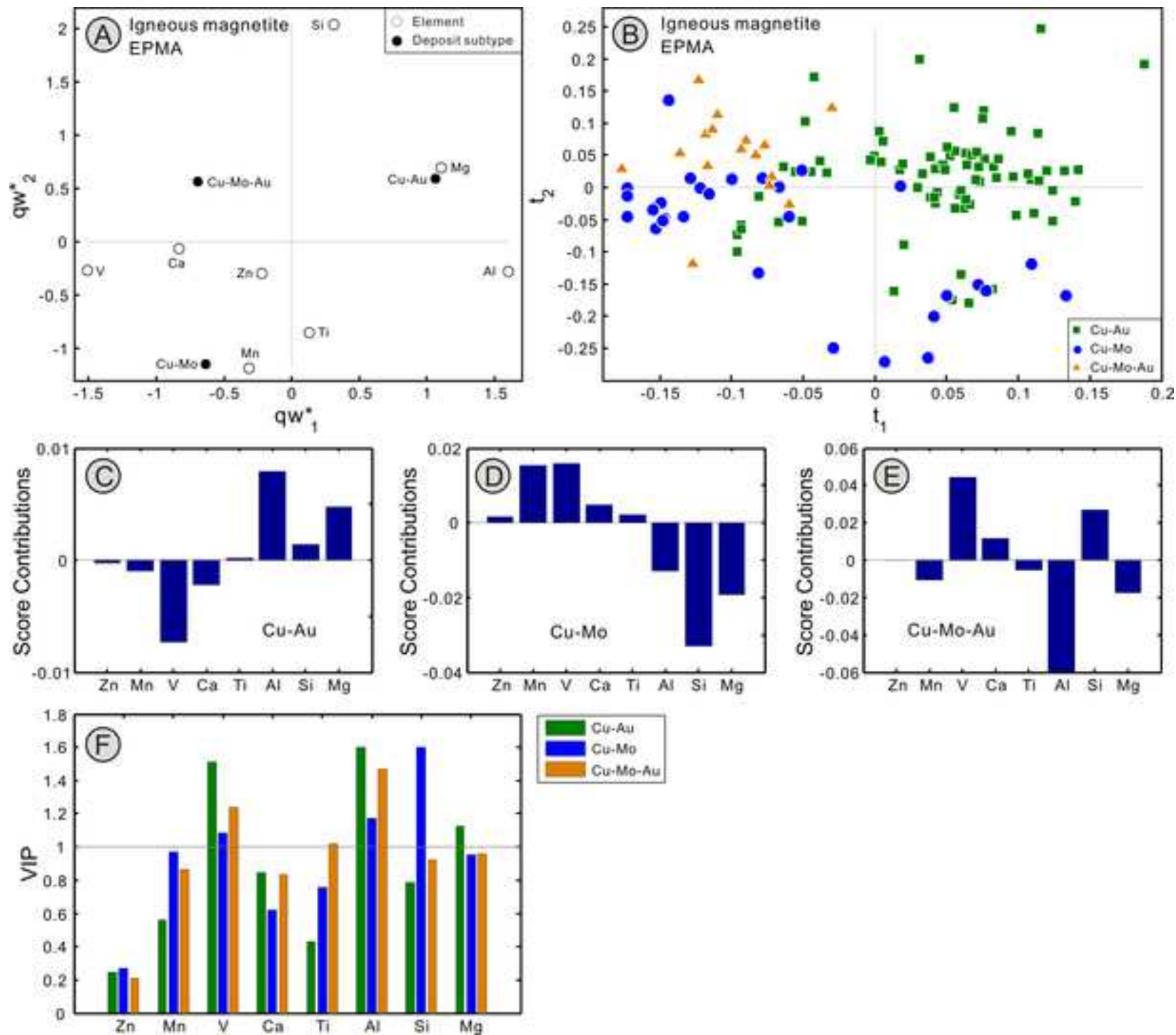


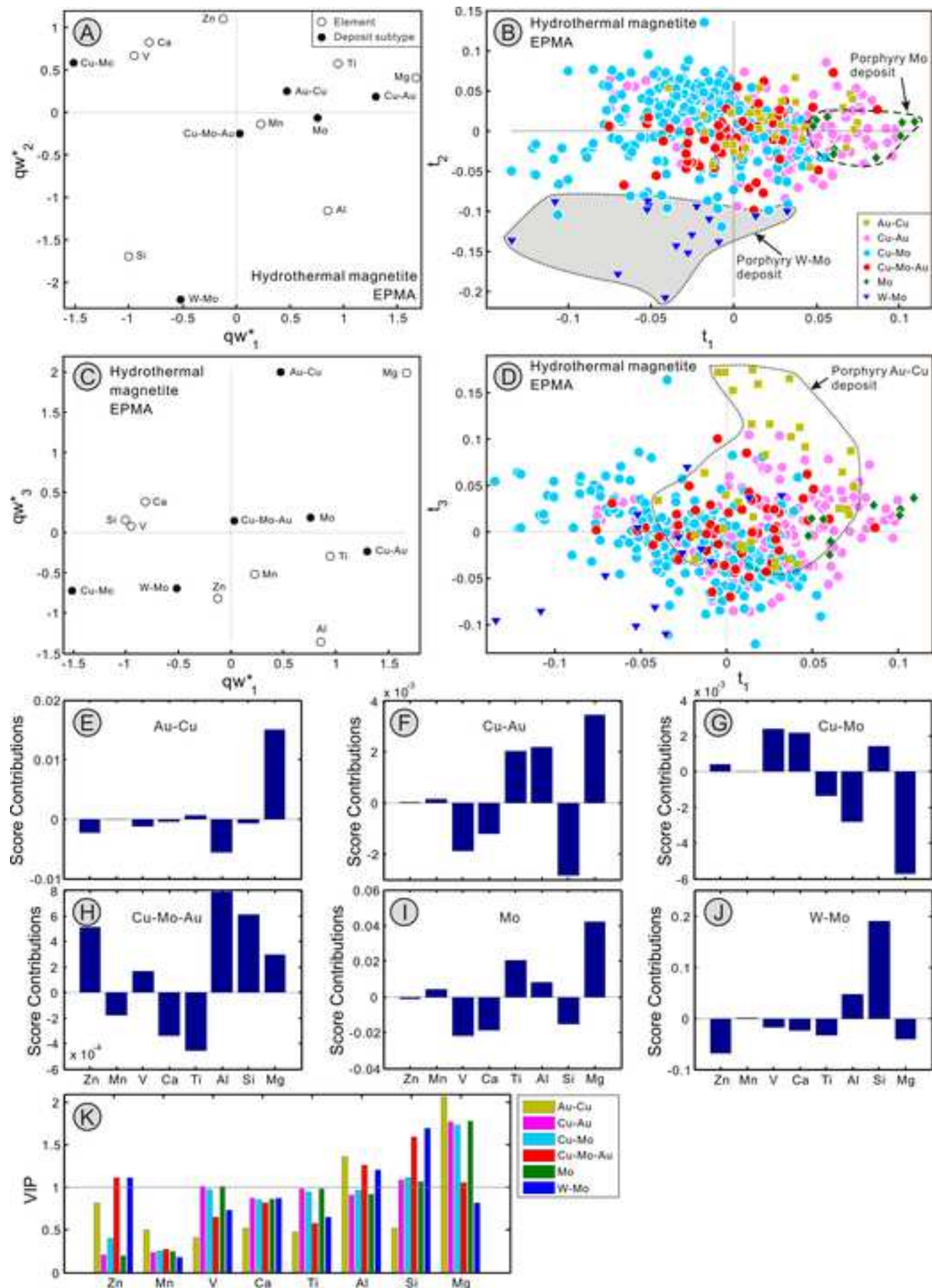


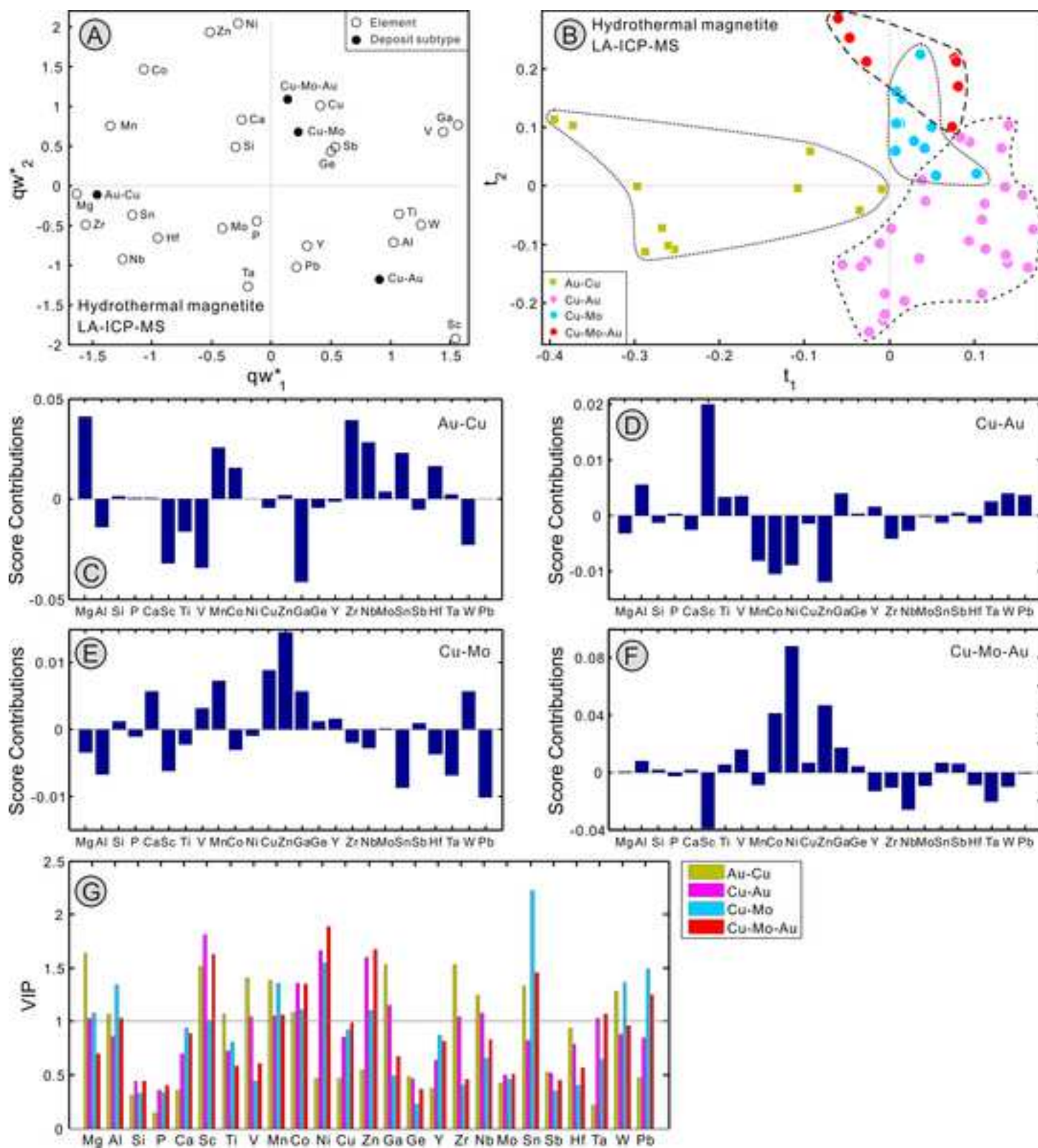


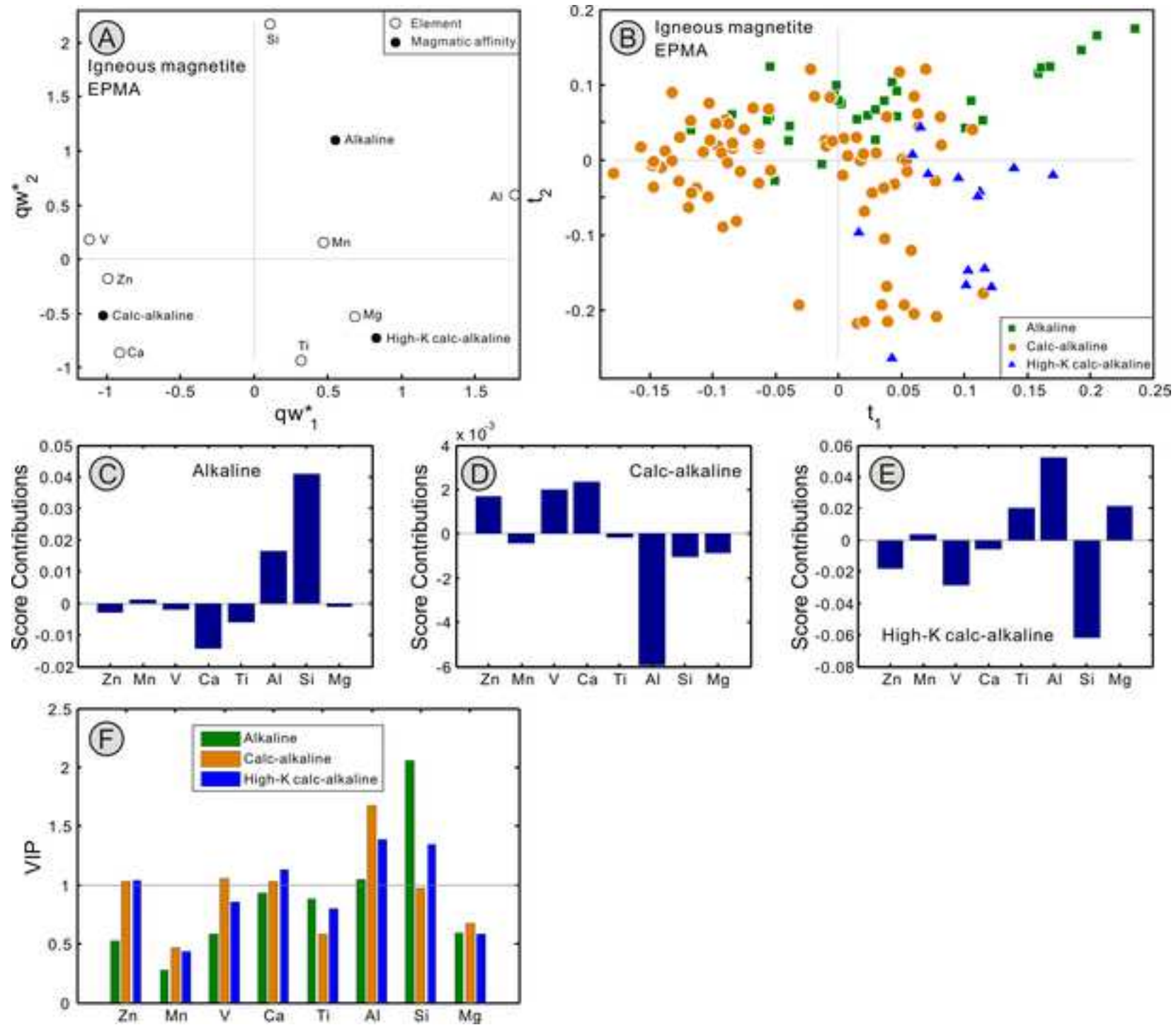




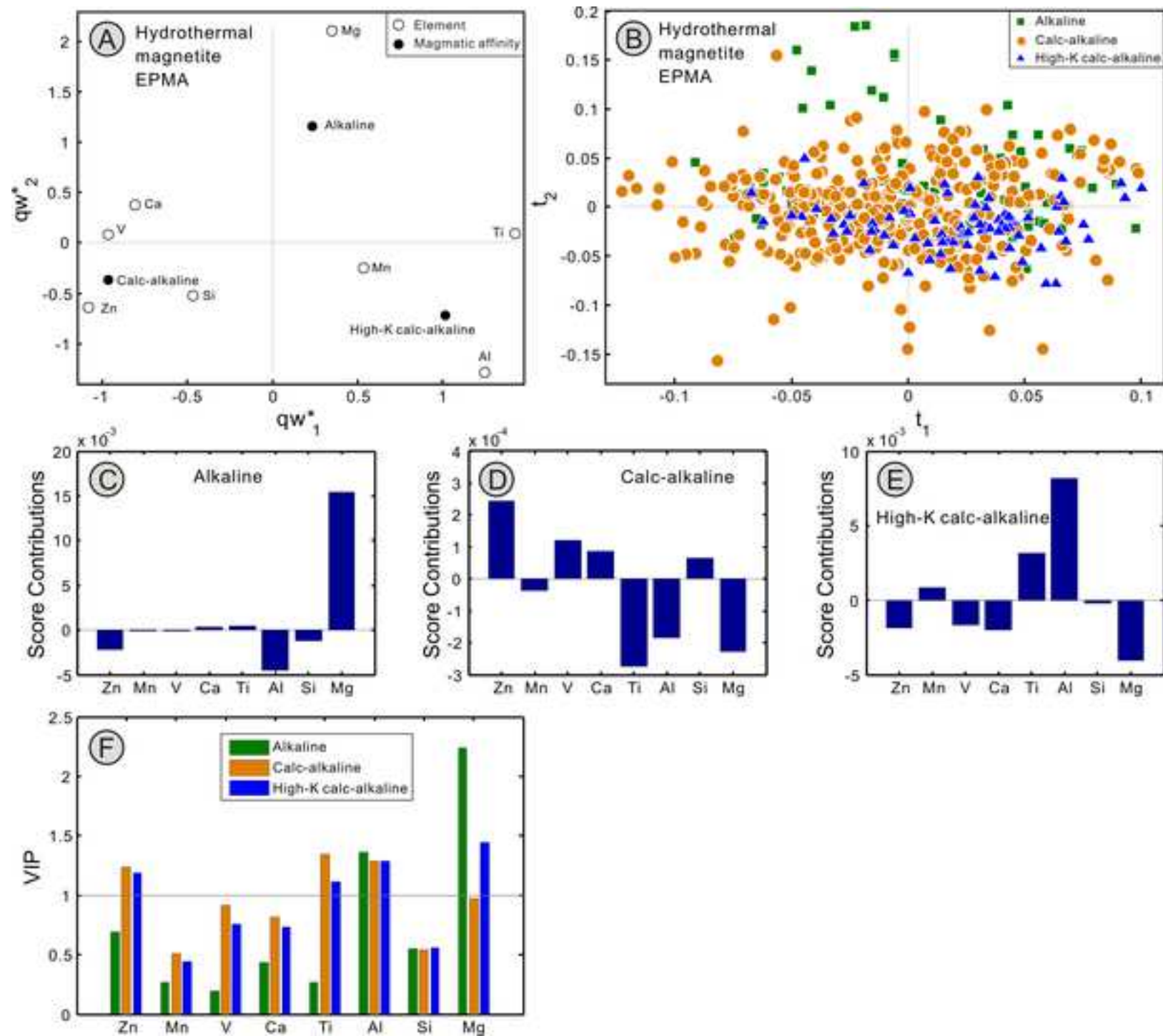


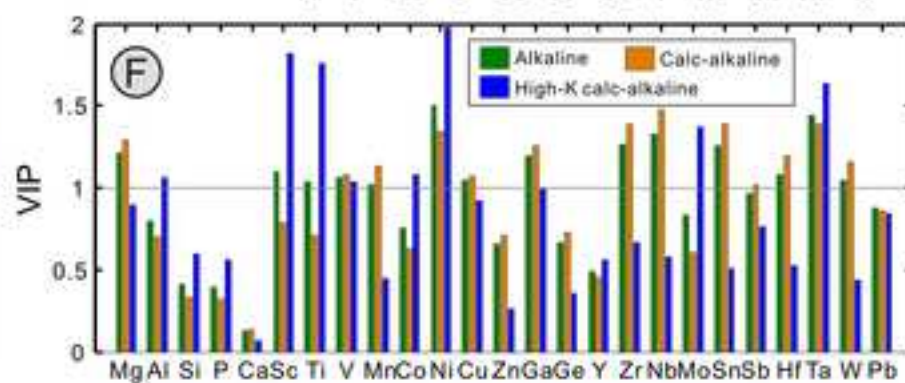
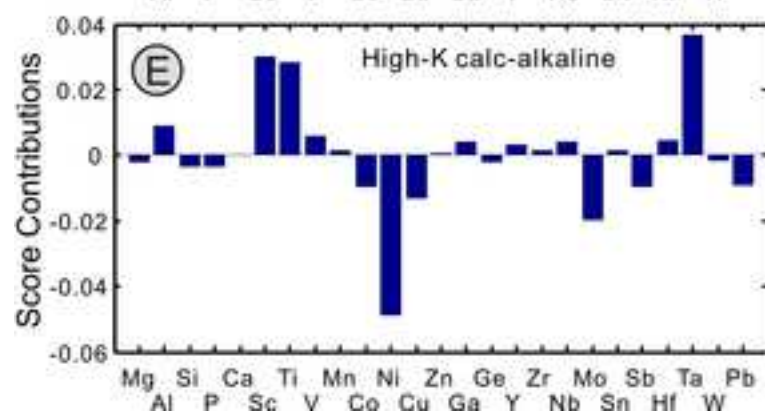
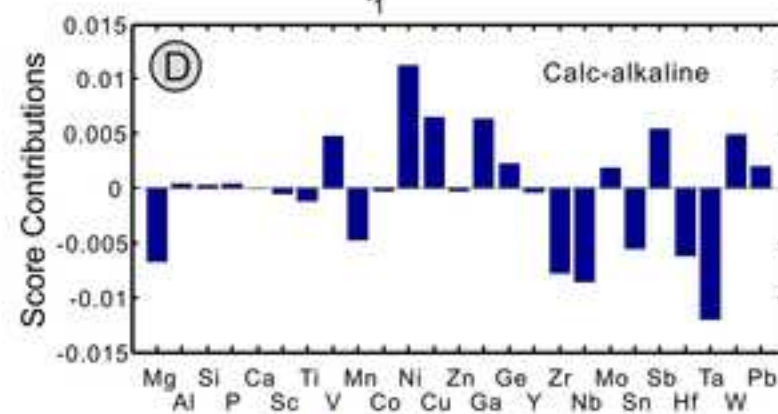
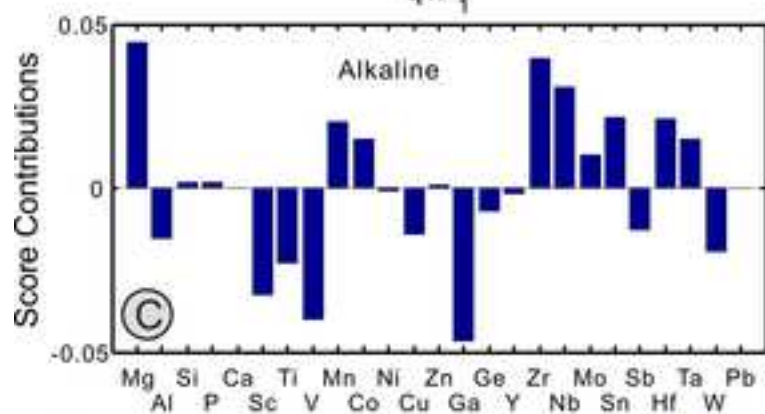
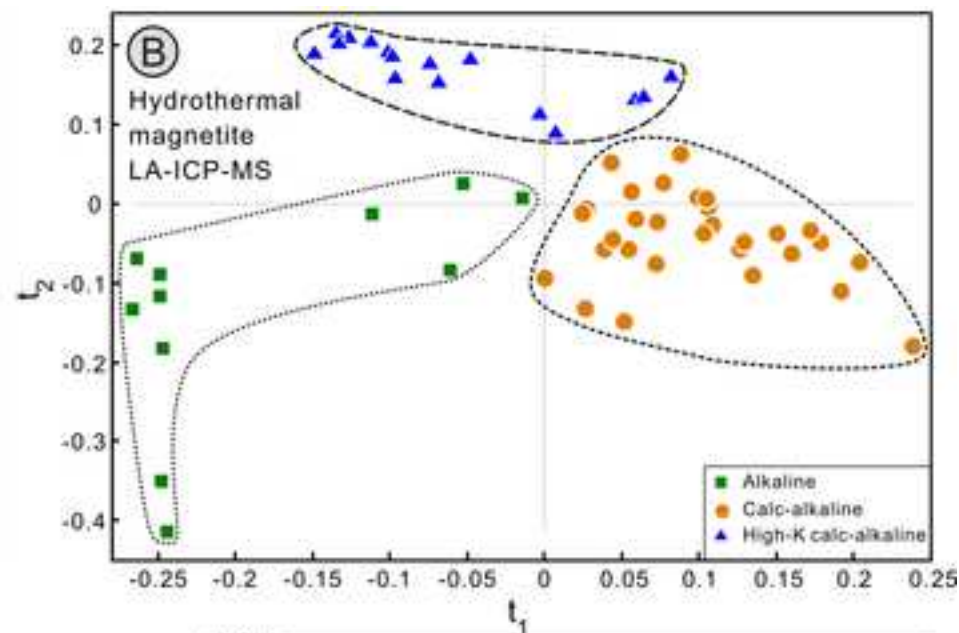
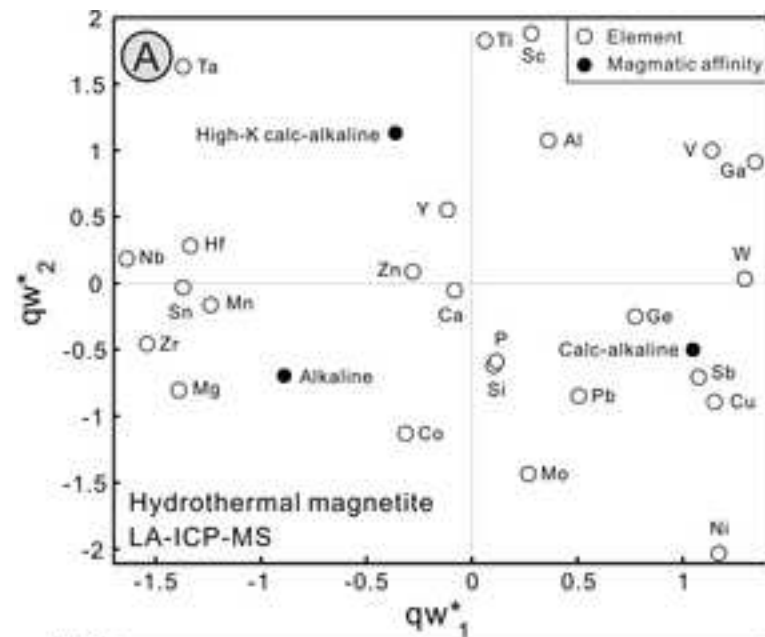


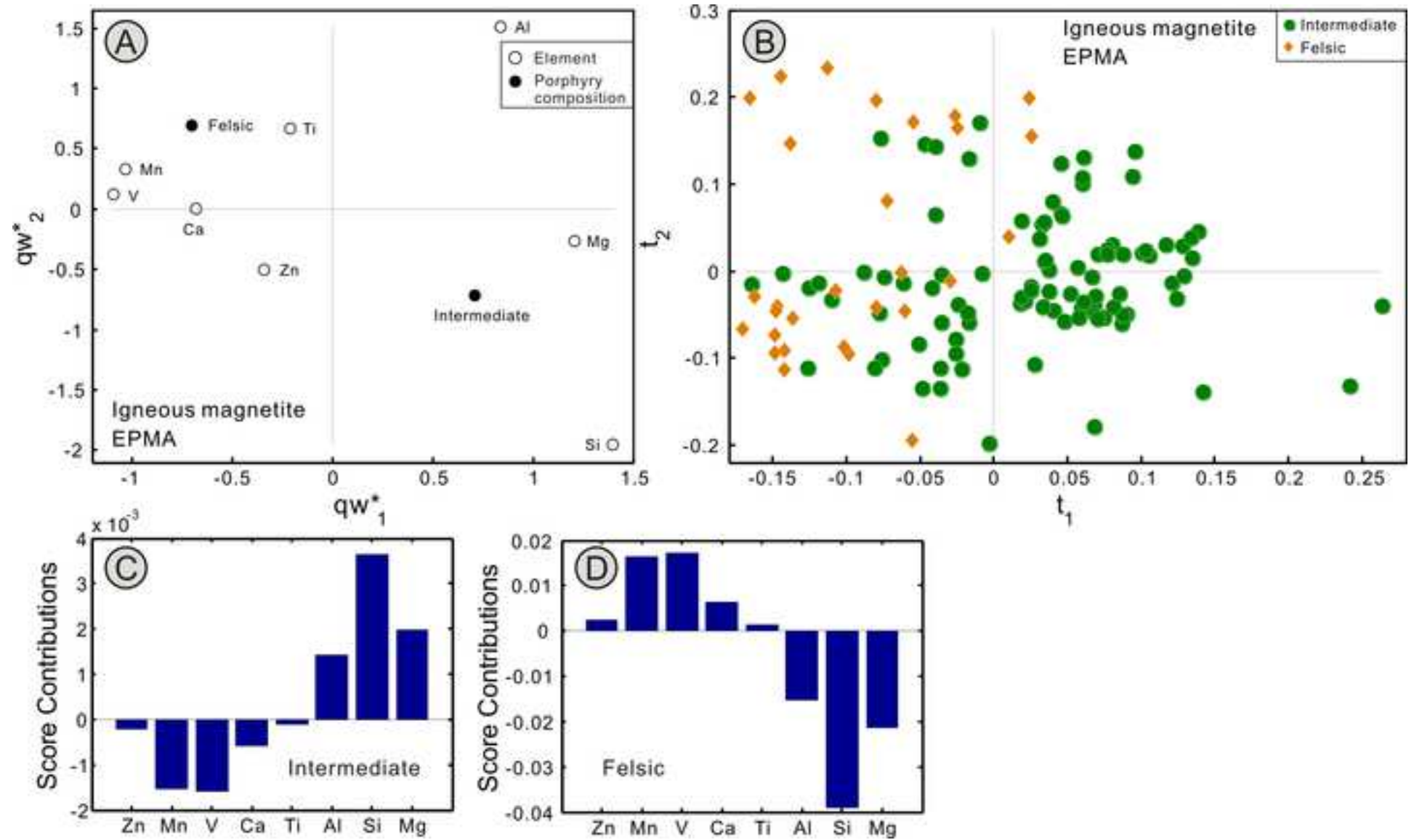


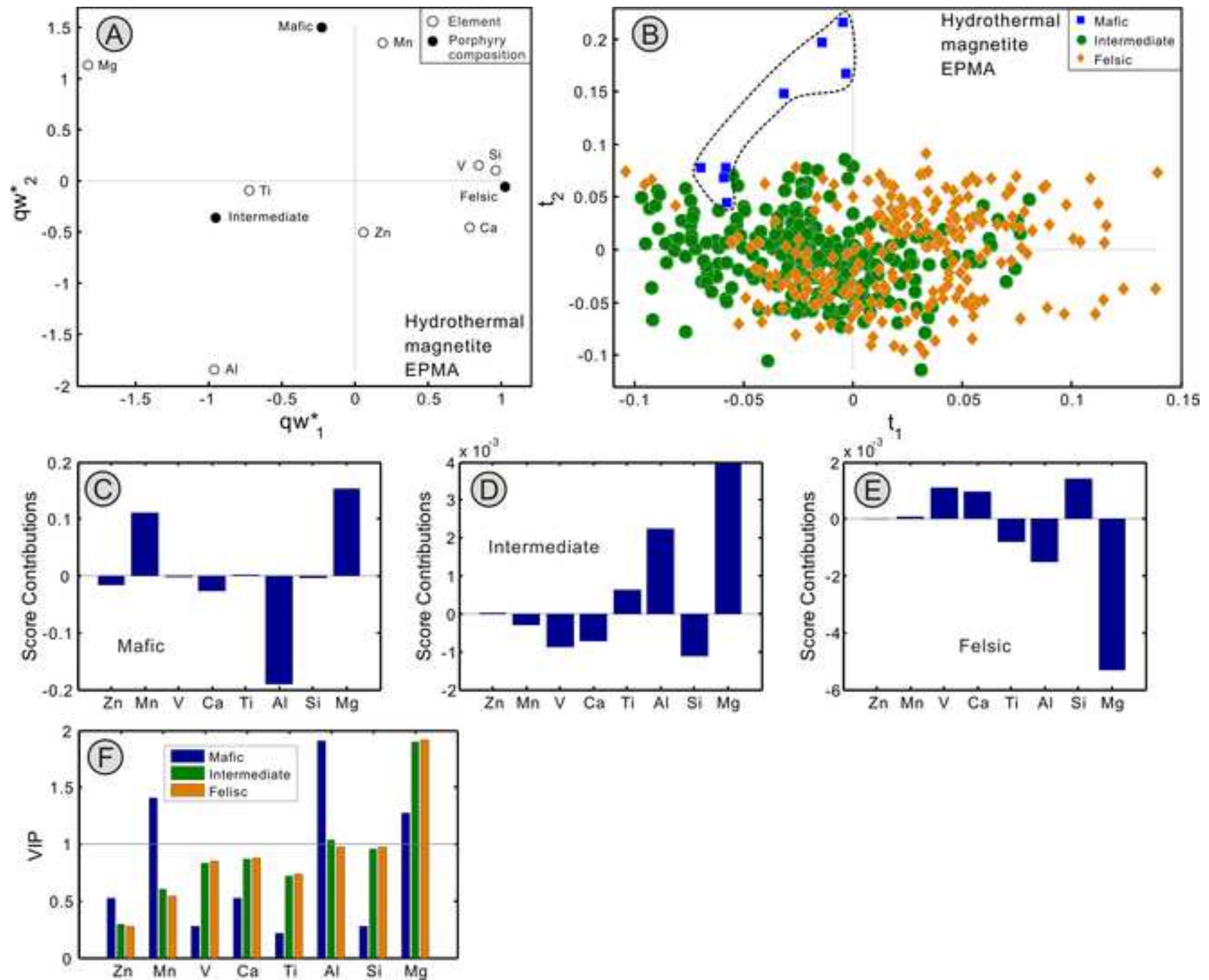


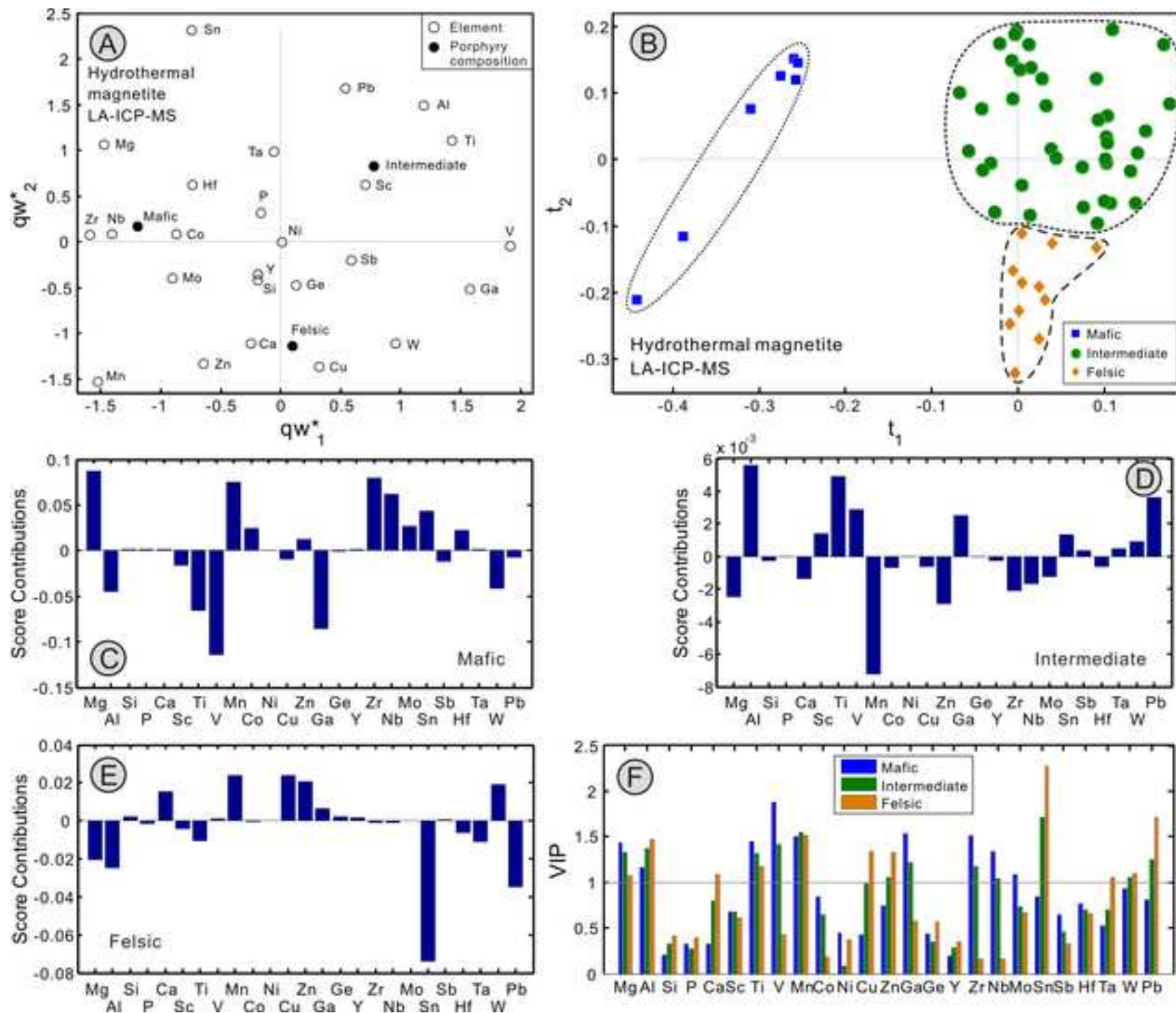


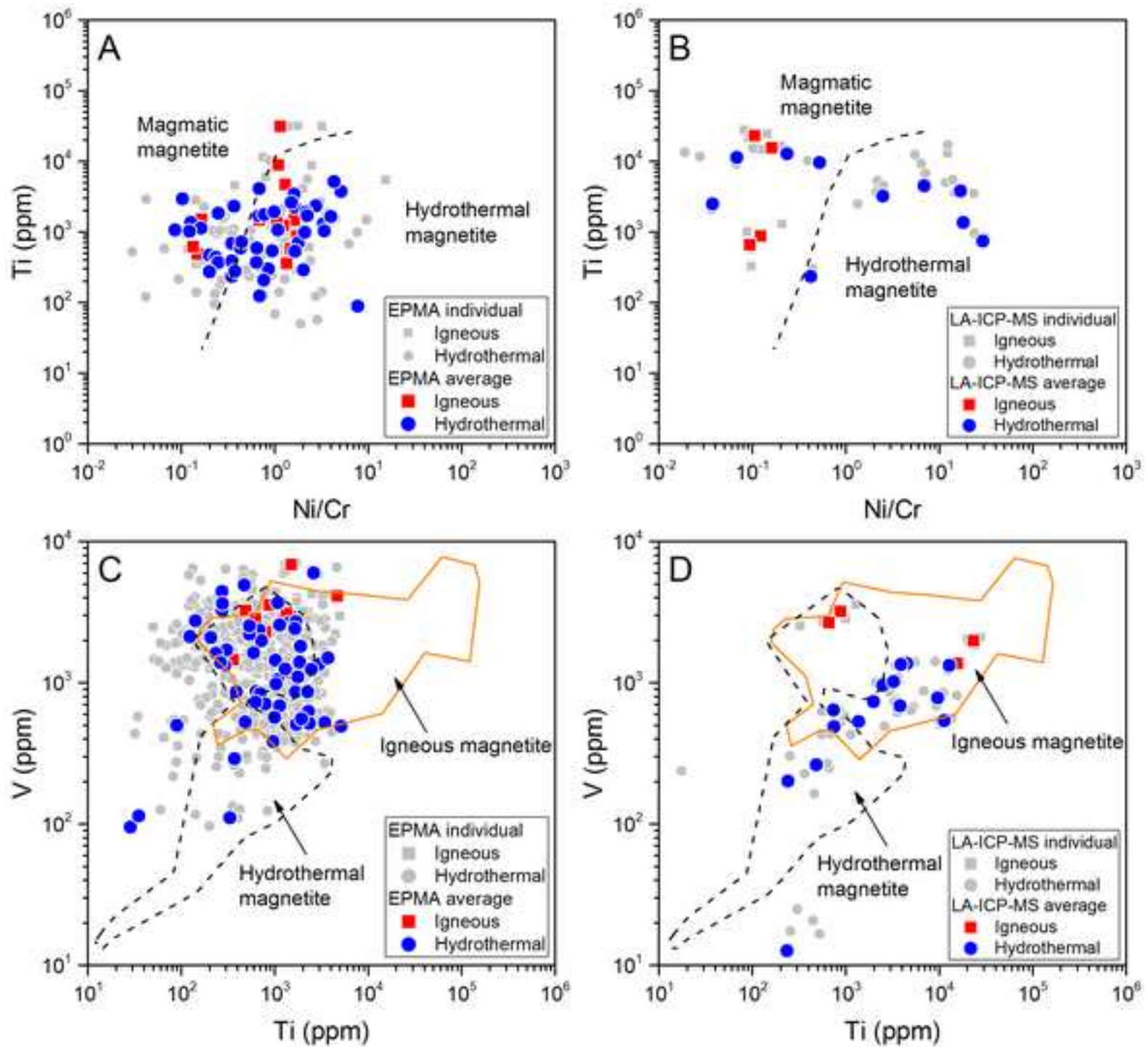












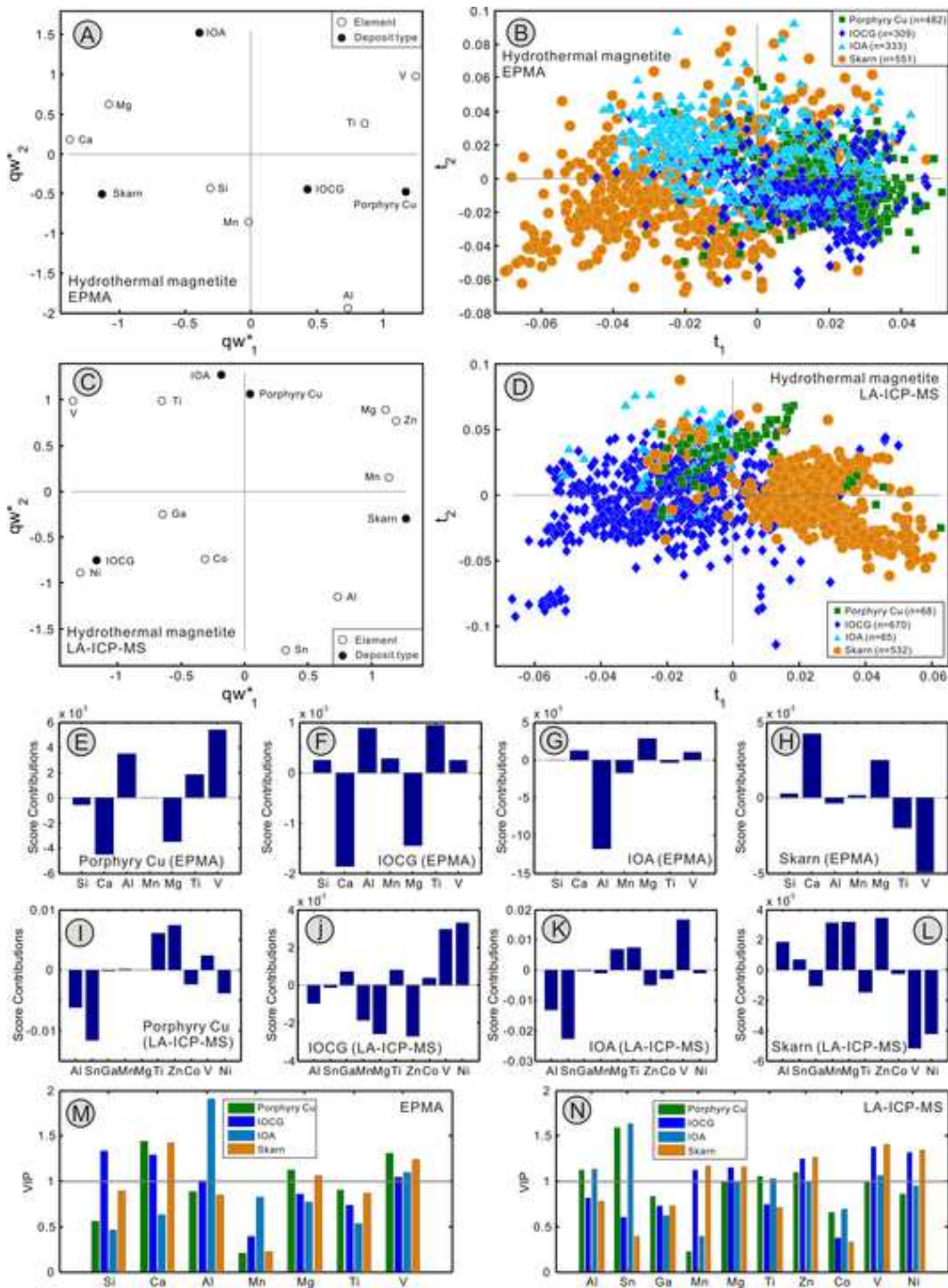


Table 1. Main Characteristics of Studied Porphyry Deposits

Deposit	Location	Mineralization	Production, resource, or reserve	Age	Magmatic affinity	Host porphyry composition	Host porphyry classification	Country rock	Reference
<b>Western North America</b>									
Bingham Canyon	United States	Cu-Mo-Au	Production: 2666 Mt at 0.74% Cu, 0.04% Mo, 0.49 g/t Au, and 3.29 g/t Ag	Eocene (~39-37 Ma)	High-K calc-alkaline	Quartz monzonite	Intermediate	Siliciclastic and carbonate rocks of the Oquirrh Group	Cooke et al. (2005), Redmond and Einaudi (2010)
Granisle	Canada	Cu-Au	Production: 53 Mt at 0.47% Cu	Eocene (~51 Ma)	Calc-alkaline	Quartz diorite porphyry and biotite feldspar porphyry	Intermediate	Andesite and sedimentary rocks (shale, siltstone, conglomerate) of the Hazelton Group	Wilson et al. (1980), Dirom et al. (1995)
Butte	United States	Cu-Mo	Production and reserves: 2083 Mt at 0.85% Cu	Paleocene (~66-64 Ma)	Calc-alkaline	Quartz porphyry and granite porphyry	Felsic	Butte granite and cogenetic aplites and pegmatites	Lund et al. (2002), Dilles et al. (2003), Cooke et al. (2005), Rusk et al. (2008), Reed et al. (2013)
Mount Milligan	Canada	Cu-Au	Total proven and probable reserves: 542 Mt at 0.20% Cu and 0.36 g/t Au	Early Jurassic (~183 Ma)	Alkaline	Quartz monzonite to monzodiorite	Intermediate	Trachyandesites and volcaniclastic rocks of the Witch Lake Group	Lefort et al. (2011), Jago et al. (2014), Logan and Mihalynuk (2014), Thompson Creek Metals Company (2016, internal report)
Copper Mountain	Canada	Cu-Au	Total proven and probable reserves: 205 Mt at 0.29% Cu, 0.10 g/t Au, and 1.21 g/t Ag	Late Triassic-Early Jurassic (~204-200 Ma)	Alkaline	Diorite, monzonite, and syenite	Intermediate	Andesite to basalt of the Nicola Group	Holbek and Noyes (2013), Logan and Mihalynuk (2014)
Mount Polley	Canada	Cu-Au	Total measured and indicated resources: 411 Mt at 0.28% Cu, 0.29 g/t Au, and 0.81 g/t Ag (cut-off grade of 0.25% Cu)	Late Triassic (~205-202 Ma)	Alkaline	Diorite, monzonite, plagioclase porphyry, and syenite	Intermediate	Basalt and carbonaceous sedimentary rocks of the Nicola Group	Fraser (1994), Logan and Mihalynuk (2014), Pass et al. (2014), Imperial Metals Corporation (2016, internal



			equivalent)						report)
Endako	Canada	Mo	Production and reserves: 341 Mt at 0.07% Mo	Late Jurassic (~148-145 Ma)	Calc-alkaline	Granitic rocks	Felsic	Granite to granodiorite of the François Lake plutonic suite	Selby et al. (2000), Selby and Creaser (2001), Sinclair (2007)
<b>Western South America</b>									
Bajo de la Alumbreira	Argentina	Cu-Au	Production and remaining resources: 605 Mt at 0.54% Cu and 0.64 g/t Au	Miocene (~7 Ma)	High-K calc-alkaline	Dacite porphyry	Intermediate	Andesite of the Farallón Negro Volcanic Complex	Ulrich and Heinrich (2001), Proffett (2003), Harris et al. (2008)
Morococha (district)	Peru	Cu-Mo-Au	Total measured and indicated resources of the Toromocho porphyry Cu-Mo deposit: 520 Mt at 0.37% Cu, 0.01% Mo, and 6.10 g/t Ag	Miocene (~9-7 Ma)	Calc-alkaline	Dioritic, granodioritic, and quartz monzonitic porphyry	Intermediate	Carbonate rocks of the Pucará Group and Anticona diorite	Catchpole et al. (2015), Chinalco Mining Corporation (2016, internal report)
Escondida Norte	Chile	Cu-Mo	Production and reserves: sulfide (supergene): 1280 Mt at 1.24% Cu; oxide: 330 Mt at 0.77% Cu	Eocene (~38-36 Ma)	Calc-alkaline	Granodiorite to tonalite	Felsic	Andesite to rhyolite of La Tabla Formation and coeval intrusive phase	Cooke et al. (2005), Romero et al. (2011)
<b>Eastern North America</b>									
Mount Pleasant	Canada	W-Mo	Production and reserves: 22.5 Mt at 0.21% W, 0.10% Mo, and 0.08% Bi	Carboniferous (~340-330 Ma)	Calc-alkaline	Granitic rocks	Felsic	Rhyolite to dacite, minor andesite, trachyandesite and basalt, and argillite breccia of the Piskahagan Group	Kooiman et al. (1986), Samson (1990), Yang et al. (2003)
<b>Eastern Europe</b>									
Rosia Poieni	Romania	Cu-Au	Total measured, indicated, and inferred resources: 350 Mt at 0.36% Cu and 0.29 g/t Au	Miocene (~9 Ma)	Calc-alkaline	Diorite porphyry	Intermediate	Rotunda andesite, volcanoclastic rocks, and sedimentary rocks	Borcós et al. (1998), Milu et al. (2004), Kouzmanov et al. (2005)

Skouries	Greece	Cu-Au	Total proven and probable reserves: 138 Mt at 0.53% Cu and 0.81 g/t Au	Miocene (~19 Ma)	Alkaline	Monzonite porphyry	Intermediate	Biotite-gneiss and schist of the Vertiskos Formation	Frei (1995), Kroll et al. (2002), Eliopoulos et al. (2014)
<b>Central Asia</b>									
Sari Gunay	Iran	Au-Cu	Resources: 52 Mt at 1.77 g/t Au (cut-off grade of 1.00 g/t Au)	Miocene (~12-10 Ma)	Alkaline	Latitic to trachytic volcanic complex	Intermediate	Schist, limestone, and intermediate to felsic volcanic rocks	Richards et al. (2006)
Reko Diq (H9, H13, H14-H15, H79, Spegar centers)	Pakistan	Cu-Au	Total measured, indicated, and inferred resources: 5900 Mt at 0.41% Cu and 0.22 g/t Au	Miocene (~14-10 Ma)	Calc-alkaline	Quartz diorite to granodiorite	Intermediate	Andesite of the Reko Diq Formation and clastic sedimentary rocks of the Dalbandin Formation	Perelló et al. (2008), Raziq et al. (2014), Tethyan Copper Company (2016, internal report)
Kharmagtai (district)	Mongolia	Cu-Au	Total measured, indicated, and inferred resources: 133 Mt at 0.36% Cu and 0.37 g/t Au (cut-off grade of 0.30% Cu equivalent)	Late Carboniferous (~297 Ma)	Calc-alkaline	Monzodiorite and diorite porphyry	Intermediate	Volcano-sedimentary sequence	Kirwin et al. (2005), Müller et al. (2010), Vigar (2014)
Oyu Tolgoi (district)	Mongolia	Cu-Mo-Au	Total proven and probable reserves: 1494 Mt at 0.85% Cu, 0.31 g/t Au, and 1.23 g/t Ag	Late Devonian (~372-370 Ma)	High-K calc-alkaline	Quartz monzodiorite	Intermediate	Basalt and minor volcanoclastic and sedimentary rocks of the Oyu Tolgoi and Heruga sequences	Perelló et al. (2001), Crane et al. (2012), Porter (2016)
<b>Southwestern Pacific</b>									
Porgera (deep veins)	Papua New Guinea	Au-Cu	Total proven and probable reserves: 14 Mt at 4.24 g/t Au	Miocene (~6 Ma)	Alkaline	Hypabyssal intrusions of alkali basaltic, hawaiitic, and mugearitic compositions	Mafic	Carbonaceous mudstones and calcareous siltstones of the Chim Formation	Richards et al. (1997), Ronacher et al. (2004), Barrick Gold Corporation (2015, internal report)
Ridgeway	Australia	Au-Cu	Total measured, indicated, and inferred resources: 150 Mt at 0.51 g/t Au, 0.33% Cu, and 0.65 g/t Ag	Late Ordovician (~457-456 Ma)	Alkaline	Monzodiorite to quartz monzonite	Intermediate	Andesitic- and basaltic-clast volcanic conglomerate and siltstone of the Weemalla Formation	Wilson et al. (2007), Newcrest Mining (2016, internal report)

Table 2. Summary of Samples Analyzed, Magnetite Types, and Number of Analyses per Sample

Deposit	Sample no.	Magnetite types	Number of analyses		Deposit	Sample no.	Magnetite types	Number of analyses	
			EPMA <sup>1</sup>	LA-ICP-MS <sup>2</sup>				EPMA <sup>1</sup>	LA-ICP-MS <sup>2</sup>
<b>Western North America</b>					<b>Western South America</b>				
Bingham Canyon	BC-1	Hydrothermal	15(6)		Bajo de la Alumbreira	3129	Hydrothermal	9	5
Granisle	2045	Hydrothermal	9			3130	Hydrothermal	9	4
Butte	10772-32A	Hydrothermal	4			3131	Hydrothermal	9	3
	10778-6	Hydrothermal	4			3132	Igenous	9	
	10835-10	Hydrothermal	9			3133	Igenous	5	4
	10880-B	Igneous	9	2		49-60	Hydrothermal	8(8)	
	10943-1	Hydrothermal	4			51-522	Hydrothermal	7(7)	4
	10961-766	Hydrothermal	9	4		51-61	Hydrothermal	8(8)	
	11135-2485	Hydrothermal	1		Morococha (district)	T1	Hydrothermal	10(10)	3
	11135-3618	Hydrothermal	6			T2	Hydrothermal	8(8)	4
	11148-4620	Hydrothermal	9			KMO-6-205	Igenous	8(8)	
	11153-3713	Hydrothermal	17			KMO-7-512	Hydrothermal	8(8)	
	11166-3199	Hydrothermal	9	6		MO-6-KK-39a	Igenous	8(8)	
	11171-3367	Hydrothermal	3		Escondida Norte-Zaldívar	EN2	Hydrothermal	9	
	11172-2901	Hydrothermal	9			EN3	Hydrothermal	9	
	11185-1797a	Hydrothermal	5		<b>Eastern North America</b>				
	11185-1797b	Igneous	2		Mount Pleasant	SC1	Hydrothermal	6	
11185-2198.5B	Hydrothermal	6			SC2	Hydrothermal	9		
11185-2391	Hydrothermal	9		<b>Eastern Europe</b>					
11185-3273	Hydrothermal	6		Rosia Poieni	RP-3-RR-04	Hydrothermal	8(8)		
11185-3448	Hydrothermal	3			RP-3-RR-10	Igenous	8(8)		

	11185-4658	Hydrothermal	2			RP-4-CH-34	Igenous	4(4)	
	11185-4854	Hydrothermal	6		Skouries	1836	Hydrothermal	8(5)	
	7233D	Hydrothermal	9			1837	Hydrothermal	15(6)	
	9124-220-A	Hydrothermal	9	1	<b>Central Asia</b>				
	9714.5	Hydrothermal	6		Sari Gunay	DK74	Hydrothermal	9(6)	
	9868-2	Hydrothermal	6		Reko Diq	Loc 18a	Hydrothermal	6(6)	5
	BU-96-MR-13	Hydrothermal	9			Loc 18b	Igenous	4(4)	
	Bub2k-1A	Hydrothermal	6			Loc 25	Hydrothermal	5(5)	2
	Bub2k-1B	Hydrothermal	9			Loc 42	Hydrothermal	8(8)	
	Bub2k-3	Hydrothermal	6			RK 5	Hydrothermal	8(8)	4
	BUR-98-13	Hydrothermal	15			RK 8	Igenous	8(8)	
	BUR-98-5	Igneous	9	3		RK 14	Hydrothermal	8(8)	
	BUR-98-8	Igneous	9	2		RK 18	Hydrothermal	10(10)	1
Mount Milligan	90-616-191	Igneous	8(8)			RK 22	Igenous	8(8)	
	90-667-67.5	Igneous	6(6)			RK 24	Hydrothermal	4(4)	
Copper Mountain	2089	Hydrothermal	6(6)			TAF	Hydrothermal	6(6)	
	2082	Hydrothermal	16(8)			Spegar1	Igenous	3(3)	
Mount Polley	WB-04-106-305.1	Igneous	8(8)		Kharmagtai	Kharmagtai	Hydrothermal	12	
	WB-04-149-29	Igneous	8(8)		Oyu Tolgoi	Oyu Tolgoi	Hydrothermal	15(6)	
Endako	2071	Hydrothermal	9		<b>Southwestern Pacific</b>				
					Porgera	P99-003	Hydrothermal	9	7
					Ridgeway	Ridgeway	Hydrothermal	15(6)	4

<sup>1</sup>Spot analyses. Number in parenthesis means analyses by Dupuis and Beaudoin (2011)

<sup>2</sup>Line analyses